The Atacama Cosmology Telescope: Cross-correlation of kSZ and continuity equation velocity reconstruction with photometric DESI LRGs

Fiona McCarthy^{1,2,3*}, Boryana Hadzhiyska^{4,2,5,6}, J. Richard Bond⁷, William R. Coulton^{1,2}, Jo Dunkley^{8,9}, Carmen Embil Villagra^{1,2}, Matthew C. Johnson^{10,11}, Kavilan Moodley^{12,13}, Toshiya Namikawa^{1,14,2}, Bernardita Ried Guachalla^{15,16,17}, Blake D. Sherwin^{1,2}, Cristóbal Sifón¹⁸,

Alexander van Engelen¹⁹, Eve M. Vavagiakis^{20,21}, Edward J. Wollack²²

Accepted XXX. Received YYY; in original form ZZZ

ABSTRACT

Over the last year, kinematic Sunyaev–Zel'dovich (kSZ) velocity reconstruction—the measurement of the large-scale velocity field using the anisotropic statistics of the small-scale kSZ-galaxy overdensity correlation— has emerged as a statistically significant probe of the large-scale Universe. In this work, we perform a 2-dimensional tomographic reconstruction using ACT DR6 CMB data and DESI legacy luminous red galaxies (LRGs). We measure the cross-correlation of the kSZ-reconstructed velocity v^{kSZ} with the velocity inferred from the continuity equation applied to the DESI LRGs v^{cont} at the $\sim 10\sigma$ level, detecting the signal with an amplitude with respect to our theory of $b_v = 0.339 \pm 0.034$. We fit a scale-dependent galaxy bias model to our measurement in order to constrain local primordial non-Gaussianity $f_{\rm NL}^{loc}$, finding $f_{\rm NL}^{loc} = -180^{+61}_{-86}$ at 67% confidence, with $f_{\rm NL}^{loc}$ consistent with zero at 95% confidence. We also measure an auto spectrum at 2.1σ significance which provides a constraint on b_v of $b_v = 0.26^{+0.11}_{-0.05}$, which is consistent with the measurement from the cross spectrum. Our combined measurement is $b_v = 0.33 \pm 0.03$, an 11σ measurement. We find a good fit of our model to the data in all cases. Finally, we use different ACT frequency combinations to explore foreground contamination, finding no evidence for foreground contamination in our velocity cross correlated with the large-scale galaxy field, and find signs of foreground contamination which is contained in the equal-redshift spectra.

Key words: keyword1 – keyword2 – keyword3

1 INTRODUCTION

The kinematic Sunyaev-Zel'dovich (kSZ) effect (Zeldovich & Sunyaev 1969; Sunyaev & Zeldovich 1970, 1980) is a foreground signal

¹DAMTP, Centre for Mathematical Sciences, Wilberforce Road, Cambridge, CB3 0WA, UK

²Kavli Institute for Cosmology Cambridge, Madingley Road, Cambridge, CB3 0HA, UK

³Center for Computational Astrophysics, Flatiron Institute, 162 5th Avenue, New York, NY 10010 USA

⁴Institute of Astronomy, Madingley Road, Cambridge, CB3 0HA, United Kingdom

⁵Physics Division, Lawrence Berkeley National Laboratory, Berkeley, CA 94720, USA

⁶Berkeley Center for Cosmological Physics, Department of Physics, University of California, Berkeley, CA 94720, USA

 $^{^7}$ Canadian Institute for Theoretical Astrophysics, 60 St. George Street, University of Toronto, Toronto, ON, M5S 3H8, Canada

⁸ Joseph Henry Laboratories of Physics, Jadwin Hall, Princeton University, Princeton, NJ, USA 08544

⁹Department of Astrophysical Sciences, Peyton Hall, Princeton University, Princeton, NJ USA 08544

¹⁰Perimeter Institute for Theoretical Physics, 31 Caroline St N, Waterloo, ON N2L 2Y5, Canada

¹¹Department of Physics and Astronomy, York University, Toronto, ON M3J 1P3, Canada

¹²A. Astrophysics Research Centre, University of KwaZulu-Natal, Westville Campus, Durban 4041, South Africa

¹³B. School of Mathematics, Statistics & Computer Science, University of KwaZulu-Natal, Westville Campus, Durban 4041, South Africa

¹⁴Center for Data-Driven Discovery, Kavli IPMU (WPI), UTIAS, The University of Tokyo, Kashiwa, 277-8583, Japan

¹⁵Department of Physics, Stanford University, Stanford, CA, USA 94305-4085

¹⁶Kavli Institute for Particle Astrophysics and Cosmology, 382 Via Pueblo Mall Stanford, CA 94305-4060, USA

¹⁷SLAC National Accelerator Laboratory 2575 Sand Hill Road Menlo Park, California 94025, USA

¹⁸Instituto de Física, Pontificia Universidad Católica de Valparaíso, Casilla 4059, Valparaíso, Chile

¹⁹School of Earth and Space Exploration, Arizona State University, Tempe, AZ 85287, USA

²⁰Department of Physics, Duke University, Durham, NC, 27704, USA

²¹Department of Physics, Cornell University, Ithaca, NY, 14853, USA

²²NASA Goddard Space Flight Center, 8800 Greenbelt Road, Greenbelt, MD 20771, USA

to the cosmic microwave background (CMB) sourced when a CMB photon Thomson scatters off ionized electron gas in the late Universe moving with respect to the CMB rest frame. The signal contains information about the bulk velocity as well as the density of electrons along the line of sight.

On small scales (angular multipoles $\ell > \sim 4000$), the kSZ signal is expected to dominate over the primary CMB anisotropies, and it is emerging as a new probe of cosmic structure and astrophysics as we make higher sensitivity and resolution CMB measurements. We have moved beyond the era of relatively low and medium significance detections with Planck and early ACT and SPT datasets to a phase in which kSZ is a statistically significant probe of cosmology and astrophysics with the Atacama Cosmology Telescope (ACT) (e.g Hand et al. 2012; Planck Collaboration 2013; Schaan et al. 2016; Soergel et al. 2016; Hill et al. 2016; Schaan et al. 2021; Kusiak et al. 2021; Tanimura et al. 2021; Calafut et al. 2021; Hadzhiyska et al. 2025b; McCarthy et al. 2025; Laguë et al. 2024; Guachalla et al. 2025; Lai et al. 2025; Hotinli et al. 2025; Roper et al. 2025). The Simons Observatory (Ade et al. 2019; Abitbol et al. 2025) Large Aperture Telescope (LAT) survey has recently begun, and the kSZ will soon become a precision cosmology probe as well as a highly significant probe of astrophysics.

kSZ velocity reconstruction (Zhang 2010; Terrana et al. 2017; Deutsch et al. 2018; Smith et al. 2018) uses the kSZ effect to measure the large-scale velocity field of the Universe using the mode-coupling in the temperature-galaxy correlation $\langle Tg \rangle$ induced by the kSZ effect. The first implementations of kSZ velocity reconstruction were performed using *Planck* (Planck Collaboration et al. 2020a) data (Bloch & Johnson 2024) and ACT data (McCarthy et al. 2025; Laguë et al. 2025; Hotinli et al. 2025; Lai et al. 2025), with the highest signal-to-noise detections (Hotinli et al. 2025; Lai et al. 2025) coming from a combination with small- and large-scale DESI luminous red galaxies (LRGs) (Zhou et al. 2023a).

In kSZ velocity reconstruction, an estimate of the large-scale velocity \hat{v} is created from small-scale anisotropic power in $\langle Tg \rangle$. There is a distinct scale separation, with large scales here corresponding to cosmological scales (multipole $L \sim O(1-100)$, or comoving wavenumber $k \sim O(0.01) \, \mathrm{Mpc^{-1}}$) and small scales corresponding to intra-halo scales ($\ell \sim O(1000)$ or $k \sim O(1) \, \mathrm{Mpc^{-1}}$). Going forward, a superscript "L" on a field will be used to refer to a large-scale mode of it, and a superscript "S" to a small-scale mode.

In this work, we report a measurement of the kSZ velocity signal at $\sim 10\sigma$ in cross correlation with a separate measurement of the large-scale velocity field, and 11σ when the kSZ velocity auto is included. Similarly to McCarthy et al. (2025) and Lai et al. (2025), we work in the 2-dimensional formalism of Deutsch et al. (2018). We use a $\langle T_{\rm ACT-DR6}^S g_{\rm DESI-LRG}^S g_{\rm DESI-LRG}^L \rangle$ data combination similar to both Lai et al. (2025) and Hotinli et al. (2025), which recently both found 11.7 σ detections of the signal (although Hotinli et al. (2025) used ACT DR5 data as opposed to DR6).

In this paper, we follow our recent work (McCarthy et al. 2025), which used a $\langle T_{\text{ACT-DR6}}^S g_{\text{DESI-LRG}}^S g_{\text{SDSS}}^L \rangle$ combination where the large-scale Sloan Digital Sky Survey (SDSS) galaxies were filtered to produce a velocity estimate and measure the angular velocity cross-power spectrum $C_{\nu}^{\nu\nu}$. Now, we measure $C_{\nu}^{\nu\nu}$ using a redshift-binned 2-dimensional velocity template which is constructed from the continuity equation applied to the DR10 photometric DESI

LRGs (Hadzhiyska et al. 2025b, 2024; Ried Guachalla et al. 2024). We include a demonstration of our pipeline on *N*-body simulations.

This large-scale velocity field can then be correlated with itself or with other fields. The velocity-g cross-correlation is sensitive to the scale-dependence of the large-scale galaxy bias (Münchmeyer et al. 2019) and is thus a probe of local primordial non-Gaussianity (Dalal et al. 2008), parametrized by $f_{\rm NL}^{\rm loc}$ (hereafter $f_{\rm NL}$). $f_{\rm NL}$ constraints have recently been obtained from the signal (Krywonos et al. 2024; Laguë et al. 2025; Hotinli et al. 2025), with Hotinli et al. (2025) finding $f_{\rm NL} = -30^{+40}_{-33}$. In this work, we also derive $f_{\rm NL}$ constraints, finding $-264 < f_{\rm NL} < -109$ at 67% confidence, with $f_{\rm NL}$ consistent with zero at 95% confidence. Our results are not as tight as previous analyses with a similar dataset and signal-to-noise; we take steps to compare the analyses and attribute this to our use of a lower maximum scale $k_{\rm max}$.

We include a measurement of the kSZ velocity auto power spectrum, finding a 2σ measurement of the amplitude without using the cross-spectrum information. We use this to constrain b_{ν} independently of the cross-spectrum to $b_{\nu} = 0.26^{+0.11}_{-0.05}$, which is consistent with the measurement from the cross; we combine them to find $b_{\nu} = 0.33 \pm 0.03$, an 11σ measurement.

Finally, we compare our C_L^{vv} measurement to a C_L^{vg} measurement, which we make by cross-correlating the kSZ-estimated velocity field with the galaxy overdensity directly, and perform several tests for foreground bias, finding hints of foreground bias in some parts of the C_L^{vg} signal.

This paper is organized as follows. In Section 2 we describe the datasets that we use. In Section 3 we describe our pipeline. We present our theory modelling in Section 4. We show a demonstration on simulations in Section 5. In Section 6 we present our results. We find a good fit for our scale-independent model in $C_L^{\nu\nu}$, and we use this measurement to measure the scale-dependent bias induced by $f_{\rm NL}$. We show tests for foreground contamination in Sec. 7. We conclude in Section 8.

2 DATA

We use three datasets: the small-scale ACT DR6+*Planck* component-separated temperature maps (Naess et al. 2025; Coulton et al. 2024a), the small-scale DESI DR9 extended photometric luminous red galaxy (LRG) sample (Zhou et al. 2023a; Dey et al. 2019), and the large-scale DESI DR10 extended LRGs with and without velocity reconstruction performed (Zhou et al. 2023a,b). We describe these datasets in this Section.

2.1 Small-scale temperature

We use the public ACT DR6+*Planck* temperature map. This is a needlet internal linear combination (NILC) (Bennett et al. 1992; Delabrouille et al. 2009) estimation of the blackbody component of the multi-frequency ACT DR6 data (Naess et al. 2025) and *Planck* NPIPE data (Planck Collaboration 2020c), described in Coulton et al. (2024a). The blackbody components in the sky are the primary CMB anisotropies as well as the kSZ anisotropies, so we refer to this as a CMB+kSZ map. As the kSZ is a small-scale signal, the high-resolution ACT data is instrumental to this measurement.

NILC provides a minimum-variance estimate of the signal of interest, but the map contains residual foregrounds, notably the thermal Sunyaev–Zel'dovich (tSZ) effect and the cosmic infrared background (CIB). The tSZ effect can be isolated in frequency space by its well-known *y* distortion (Sunyaev & Zeldovich 1970); the CIB is harder

¹ In the ensemble average, $\langle Tg \rangle$ is zero; we refer here to the average over the one realization that we see in our sky, *i.e.* the average at fixed large-scale modes.

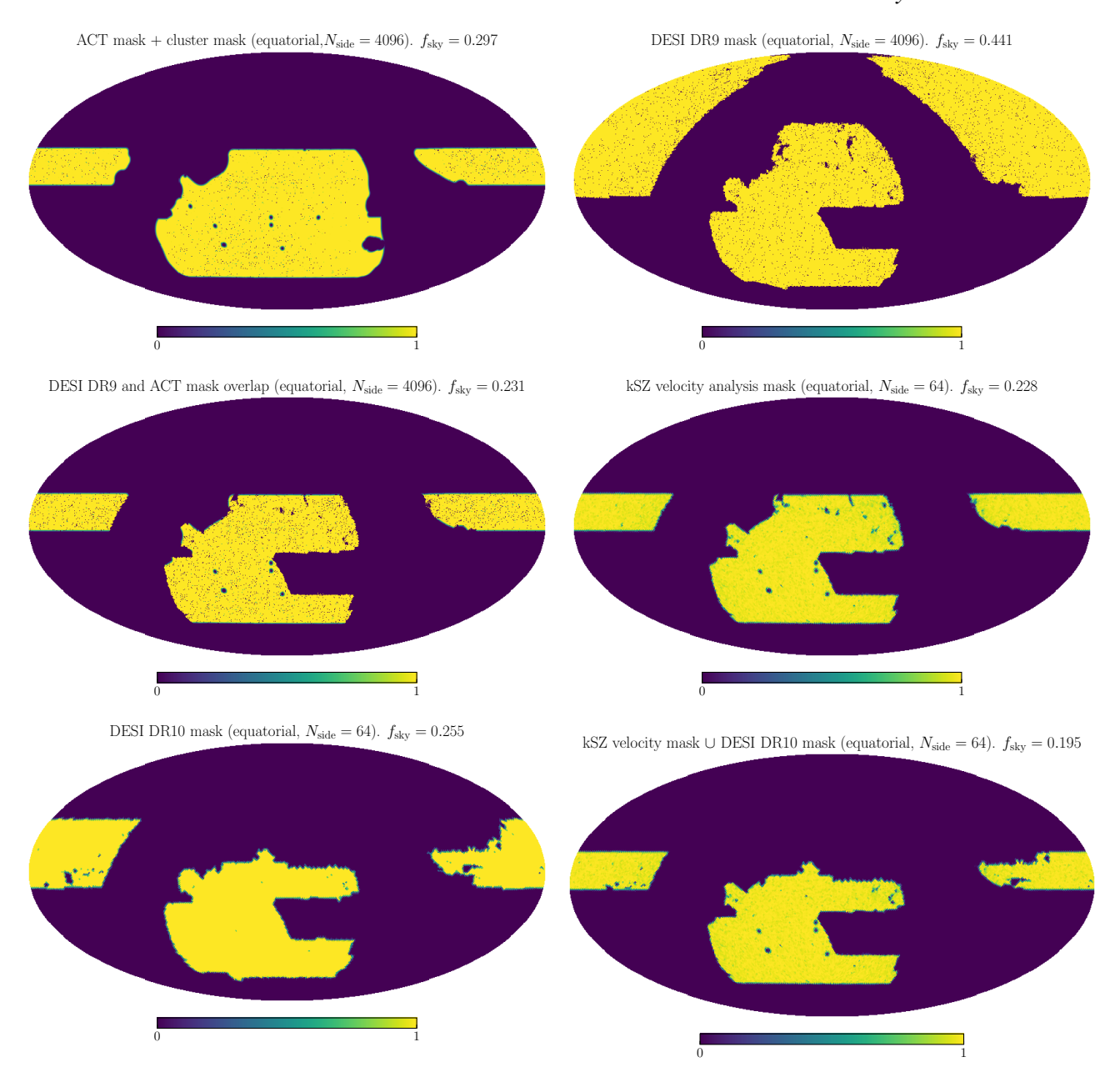


Figure 1. Masks used in this analysis. The analysis mask used for the CMB dataset is shown on the top left; this is the ACT mask combined with the cluster mask created from the ACT DR5 cluster catalogue. The DESI DR9 mask that we use for the small-scale galaxies is shown on the top right. The product of this with the ACT mask + cluster mask, which we use to perform kSZ velocity reconstruction at $N_{\text{side}} = 4096$, is shown on middle left. We downgrade this to an $N_{\text{side}} = 64$ mask and apodize with a 2 degree apodization scale to perform analysis on the reconstructed kSZ velocity; this is shown on the middle right. The mask used for the large-scale DR10 DESI galaxies is shown on the bottom left. The overlap of the two large-scale maps is shown on the bottom right to indicate the overlap in sky area between both large-scale measurements, although note that we never use this mask in practice.

to remove due to its less exact frequency dependence. In order to test our signal for foreground contamination, we will use other public ACT+Planck products described in Coulton et al. (2024a), in particular the blackbody-deprojected Compton-y map and the y-deprojected blackbody map. Both of these maps were created using constrained NILC (Chen & Wright 2009; Remazeilles et al. 2011), which can exactly remove a foreground with known frequency dependence from an ILC map. The blackbody-deprojected y-distortion map will be used as a generic "foreground" map on which we expect a null signal; the y-deprojected blackbody map will be used as an alternative input to the kSZ estimator. This has different foregrounds

than the unconstrained NILC map, though larger variance, leading to a lower signal-to-noise velocity reconstruction.

All of the ACT+*Planck* maps have a beam which we approximate as Gaussian with full width at half maximum (FWHM) of 1.6′, and cover 30% of the sky. In all cases, we project from the native Plate-Carrée (CAR) coordinate system to a HEALPix (Górski et al. 2005) coordinate system with $N_{\rm side} = 4096$, by first projecting to spherical harmonics with $\ell_{\rm max} = 3 \times 4096$ and then to HEALPix.

4 F. McCarthy et al.

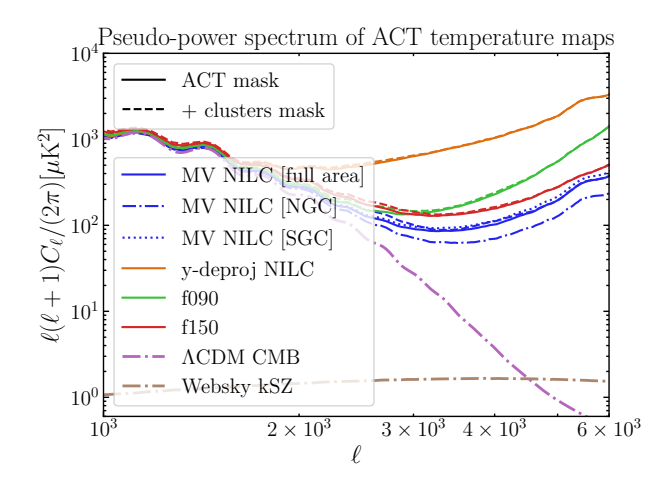


Figure 2. An estimation of the power spectra of the ACT temperature maps we use, on the full ACT region ("ACT mask") as well as the ACT region with clusters masked ("ACT + clusters masked"). We show this both for minimum-variance NILC map ("MV NILC") as well as for the tSZ-deprojected NILC map ("y-deproj NILC"), and the single-frequency maps. These are pseudo- C_ℓ estimates, estimated by measuring the raw power spectra of the masked map and dividing by the sky area available. The impact of deprojecting the tSZ is large; the impact of masking the tSZ clusters is much smaller. The variance on the NGC area is noticably lower than on the SGC area. In all cases we have divided by an estimate of the beam. Unless otherwise indicated, all measurements are on the full (NGC+SGC) area. We include an estimate of the kSZ signal from the Websky simulations Stein et al. (2020).

Sky area

The ACT survey mask that we use is shown in Fig. 1. It leaves 30.1% of the sky uncovered. In addition to this mask, we mask tSZ clusters by constructing a mask of circles of radius 5' centered on each of the 4195 objects in the ACT DR5 tSZ cluster catalogue (Hilton et al. 2021).² We apodize this mask with a 5 arcminute apodization scale using the "C1" apodization routine of pymaster. The total area of sky lost is 0.46% (of the whole sky); this is 1.4% of the total ACT footprint, such that the final sky area available is 29.7%. We will explore the impact of masking the clusters on the analysis in Section 6.1.

Power spectra

We show the power spectra of the temperature maps we use in Figure 2. These are estimated simply by measuring the pseudo- C_{ℓ} s on the available sky area and dividing by the sky area available.³

2.2 Small-scale galaxies

For the small-scale galaxy leg of our $\langle T^S g^S g^L \rangle$ bispectrum, we use the DESI LRGs with photometric redshifts described in Zhou et al. (2023a). We use the extended sample, as we are interested in maximizing number density. These objects were selected from the

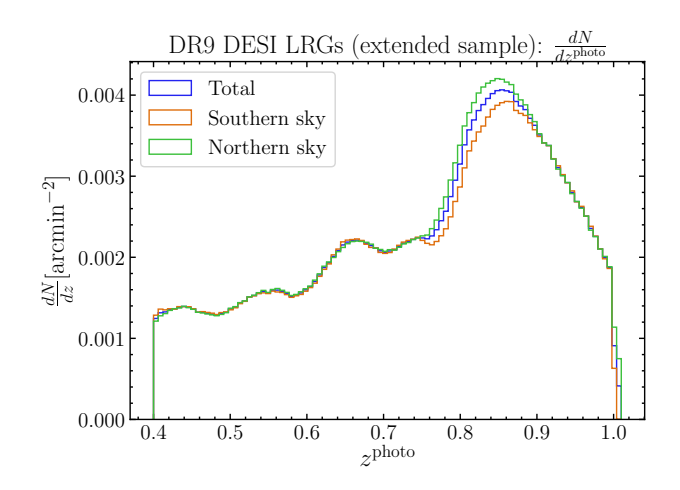


Figure 3. The distribution of the photometric redshifts z^{photo} of the DR9 DESI LRGs that we use for the small-scale galaxy sample for kSZ velocity reconstruction. There are 27,253,833 objects in total, over 44.1% of the sky.

imaging data from the DESI Legacy Survey DR9 (Dey et al. 2019; Zhou et al. 2023b). We use galaxies with photometric redshift $z^{\rm photo}$ in the full range $0.4 < z^{\rm photo} < 1.01$. There are 33,735,219 objects in total, covering 44.1% of the sky. They have photo-z uncertainty $\frac{\sigma_z}{(1+z)} \sim 0.026$. We use only the 27,253,833 objects that are assigned to one of the four tomographic redshift bins that were spectroscopically calibrated in Zhou et al. (2023a); these include all of the objects with $0.4 < z^{\rm photo} < 1$. We separate the galaxies into a North Galactic Cap (NGC) and South Galactic Cap (SGC) region. The overall number density is $0.22638~{\rm arcmin}^{-2}$, with $0.22149~{\rm arcmin}^{-2}$ in the SGC and $0.23038~{\rm arcmin}^{-2}$ in the NGC. The distributions of the photometric redshifts of these galaxies are shown in Fig. 3, in arcmin $^{-2}$.

In all cases, the sky mask we use for the small-scale galaxies is the product of the four masks provided with the extended galaxies (one for each redshift bin). This mask is shown in Figure 1, on the first row (right column).

We split the galaxies into redshift bins before performing kSZ velocity reconstruction. When we do so, we start with the predefined tomographic bins, which are defined by redshift boundaries [0.4, 0.545, 0.713, 0.885, 1.01]. There are 3,825,983, 6,404,291, 8,409,482, and 8,614,077 objects in each of the 4 bins (in order of increasing redshift). There are spectroscopically calibrated true redshift distributions $\frac{dN}{dz^{\text{true}}}$ available for these bins as part of the release.⁴

The kSZ effect is sensitive only to the radial velocity mode, which can cancel out along the line-of-sight if large redshift bins are used. To avoid this, redshift bins smaller than the velocity correlation length ($\sim 200 {\rm Mpc}$) should be used. Thus, to maximize our sensitivity, we further bin the galaxies by further dividing each of the four previously defined redshift bins into two and four bins, resulting overall N=8 bin and N=16 bin cases. When we do this, we choose boundaries in $z^{\rm photo}$ such that each bin is split into bins with an equal number of galaxies. The boundaries are shown in Table 1. We estimate the true $\frac{dN}{dz}$ by convolving the $\frac{dN}{dz^{\rm photo}}$ (estimated by histogramming the data)

² We note that since the beginning of this work, the ACT DR6 cluster catalogue, which contains 9977 objects, has been completed and released (ACT-DESHSC Collaboration et al. 2025). Switching to a mask defined with this catalogue did not affect any of our results.

³ We have checked that using filters computed from binned mask-decoupled spectra estimated with pymaster does not change our results.

⁴ These binned dataproducts and spectroscopically-calibrated $\frac{dN}{dz}$ are available at https://data.desi.lbl.gov/public/papers/c3/lrg_xcorr_2023/.

number of bins N	Boundaries (in photo-z)
4	0.4, 0.545, 0.714, 0.854, 1
8	0.4, 0.472, 0.545, 0.639, 0.713, 0.803, 0.854, 0.917, 1.01
16	0.4, 0.436, 0.472, 0.509, 0.545, 0.593, 0.639, 0.676, 0.713, 0.763, 0.803, 0.832, 0.854, 0.885, 0.917, 0.953, 1.010, 0.953, 0.954, 0.954, 0.954, 0.954, 0.955, 0.954, 0.955, 0.

Table 1. The boundaries used in redshift space to construct the tomographic galaxy overdensity samples

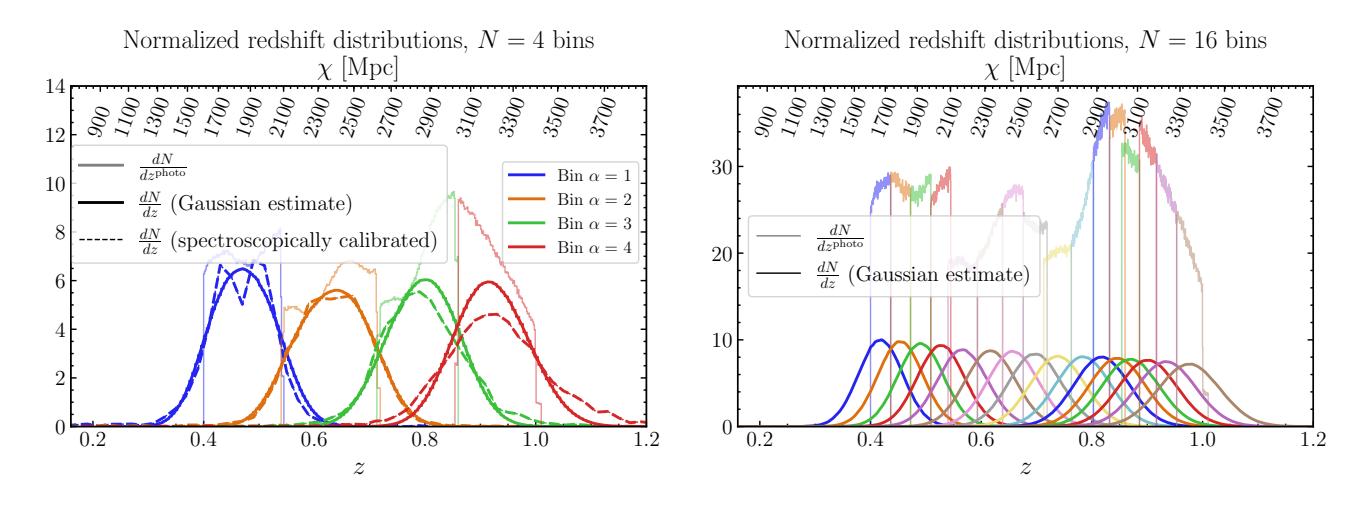


Figure 4. The redshift distributions. The $\frac{dN}{dz^{\text{photo}}}$, which we estimate just by histogramming the z^{photo} provided for each object, is in a faded line; the Gaussian-estimated $\frac{dN}{dz^{\text{true}}}$ is shown in the solid line. The spectroscopically calibrated $\frac{dN}{dz^{\text{true}}}$, provided by Zhou et al. (2023a), is also shown in the dashed lines. We use the spectroscopic estimates in our N=4 analysis, and the Gaussian estimates elsewhere. The coherence length for the velocity is ~200 Mpc; we indicate the moving distance on the upper x axis in order to compare to this number. In our 16-bin case, we approach this, but with broad redshift bins.

with Gaussians of width $0.027 \times (1 + z)$ and show these quantities in Fig. 4.

2.2.1 Projection to 2+1 dimensions

We convert each photo-z bin into number density and then overdensity by projecting the galaxy number counts into $N_{\rm side} = 4096$ HEALPix maps $g_{\alpha}(\hat{n})$ where the value of each pixel is simply the number of objects in that pixel. We convert from number counts $g_{\alpha}(\hat{n})$ to overdensity according to

$$\delta_{\alpha}^{g}(\hat{n}) = \frac{g_{\alpha}(\hat{n}) - \bar{n}_{\alpha}}{\bar{n}_{\alpha}} \tag{1}$$

where \bar{n}_{α} is the mean galaxy number density of $g_{\alpha}(\hat{n})$; we estimate this directly from the projected number counts maps by dividing the number of objects by the observed sky area.

We show in Fig. 5 estimates of the power spectra of these maps; these are estimated by simply measuring the pseudo C_{ℓ} s and dividing by the area of sky available. Due to the overlap in redshift distributions of the galaxies, the bins are correlated; we show the correlation coefficients arising from the inter-bin spectra in Appendix A. This is relevant for our analysis as the signal in neighbouring redshift bins is correlated due to this overlap; we will include this correlation in our covariance matrix calculation.

2.3 Large-scale galaxies

For the galaxies that we use for our large-scale tracer we use the extended photometric sample of LRGs from DESI Data Release 10 (DR10) (Zhou et al. 2023a,b). We use these to make estimates

both of the large-scale galaxy overdensity field and of the large-scale continuity-equation radial velocity field $\nu_r^{\rm cont}$ (hereafter we will drop the subscript r as all scalar velocities that we refer to will be radial velocities). We will then use these fields to measure two large-scale signals: $C_L^{\nu^{\rm kSZ}}\nu^{\rm cont}$ and $C_L^{\nu^{\rm kSZ}}g$, where $C_L^{\nu^{\rm kSZ}}X$ is the large-scale power spectrum of the kSZ-estimated velocity with the field X (for notational simplicity we use g instead of δ^g in the superscripts).

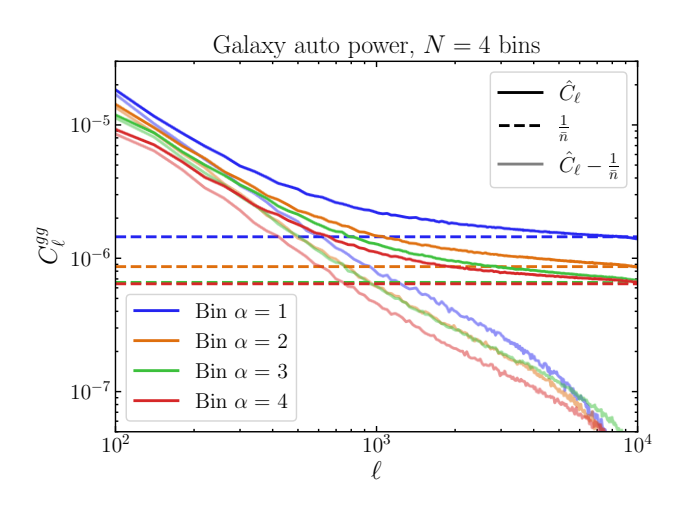
The galaxies are selected from the DESI Legacy Imaging Surveys (Dey et al. 2019) that combine data from DECaLS on Blanco, MzLS on Mayall, and BASS on Bok. For this analysis we adopt the *i*-band based photometric redshifts (Z_PHOT_MEDIAN_I), which have been shown to provide more accurate estimates. The overlap of this extended sample with the ACT footprint contains approximately 6.3 million galaxies.

Following Zhou et al. (2023a), we require the redshift error to satisfy $\sigma_z/(1+z) < 0.025$, which removes roughly 5% of objects with poorly constrained redshifts. This cut ensures that the reconstructed density and velocity fields are not biased by outliers, while retaining the vast majority of the high-quality sample.

We describe our process of estimating the velocity and large-scale overdensities in Sections 2.3.1 and 2.3.2 respectively.

2.3.1 Continuity equation velocity estimation

We estimate the large-scale velocity field from the large-scale photometric galaxy catalog using the continuity equation. This photometric continuity equation reconstruction was explored in detail in Ried Guachalla et al. (2024) and Hadzhiyska et al. (2024) and applied to the DR9+DR10 DESI LRG sample in Hadzhiyska et al. (2025b). For this reconstrution, we treat the large-scale galaxy overdensity field as



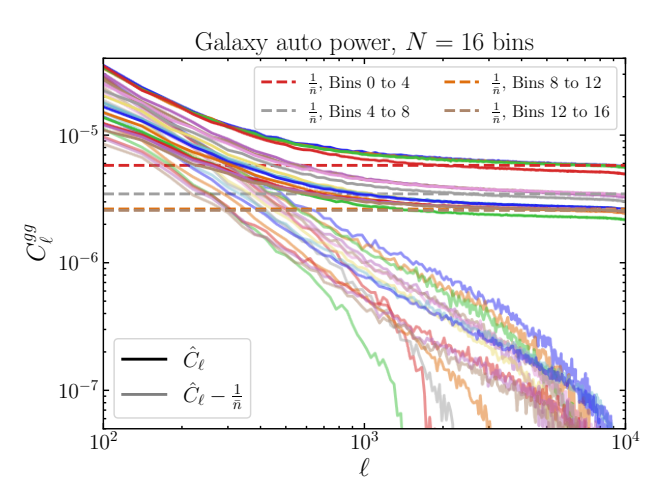


Figure 5. The auto power spectra of the binned galaxy overdensity maps for the N=4, 16 cases. We also show an estimate of the shot noise, which is simply $\frac{1}{n}$ with \bar{n} the mean number density, and the measured power spectra with this subtracted, to indicate on what scales the measurements are shot-noise dominated. We have binned the spectra in bins of width $\Delta \ell = 40$ order to smooth them. Note that in the 16-bin case we define each group of 4 bins by dividing each of the bins in the 4-bin case into bins with an equal number of galaxies, so that each of these have equal galaxy number density (and hence shot noise estimates).

a fully 3-dimensional object, treating the photometric redshift as the true redshift. In Section 5 we will explore the effect of such a reconstruction on simulations where we know the truth, to understand the behaviour of cosmological observables such as the angular galaxy velocity function C_I^{vv} .

The continuity equation is

$$\vec{\nabla} \cdot \vec{v}^{\text{cont}} + \frac{f}{b_g} \vec{\nabla} \cdot \left[\left(\vec{v}^{\text{cont}} \cdot \hat{n} \right) \hat{n} \right] = -aHf \frac{\delta^g}{b_g}, \tag{2}$$

where f is the growth rate and b_g is the galaxy bias. To solve this equation and estimate the peculiar velocity of each galaxy, we use the standard BAO reconstruction technique of Eisenstein et al. (2007), implemented in the pyrecon⁵ package (White 2015), adopting the 'RecSym' convention with the MultiGrid solver. This procedure provides an estimate of the first-order galaxy displacement field, which can then be converted into a velocity estimate.

We split the galaxy catalog into four separate redshift bins, [0.4, 0.54], [0.54 0.713], [0.713, 0.86] and [0.86 1.024], on which we perform the reconstruction separately. Additionally, we split the galaxies into two regions: north galactic cap (NGC) and south galactic cap (SGC) to reduce our computational expenses. We adopt a cubic grid of size 512^3 , and a smoothing radius of 12.5 Mpc/h following Ried Guachalla et al. (2024). Throughout we adopt a constant linear bias of b = 2.2 and Planck 2018 cosmology to estimate f at the mean effective redshift of ~ 0.8 .

Once the three-dimensional velocity field has been reconstructed we evaluate it at the positions of the input DESI LRG galaxies. We then create an estimate of the radial velocity field $v_r \equiv \vec{v} \cdot \hat{n}$, and project this to two-dimensional bins. We choose to make N projections, where N is the number of redshift bins, and we weight the projections by the galaxy distributions we use for kSZ velocity reconstruction (described in Section 2.2) $\frac{dN}{dr^{\text{true}}}$. The projected velocity

in each pixel is

$$v_r^{\text{cont},\alpha}(\hat{n}) = \frac{\sum_{i \in \hat{n}} v_{r,i}^{\text{cont}} \frac{dN^{\alpha}}{dz^{\text{true}}} (z_i^{\text{photo}})}{\int \frac{dN}{dz^{\text{true}}} (z) dz},$$
(3)

where the sum is over the continuity-equation-estimated radial velocities $v_{r,i}^{\rm cont}$ of all galaxies i in the pixel at \hat{n} , and we weight by the redshift kernel we wish to estimate the mean velocity over: $\frac{dN^{\alpha}}{dz^{\rm true}}$, where α labels the redshift bin. Note that these are evaluated at $z_i^{\rm photo}$, which is the redshift at which we evaluated the three-dimensional velocity field. The quantity in the denominator is the integral over the $\frac{dN}{dz}$ of the whole dataset and ensures normalization.

2.3.2 Large scale galaxy overdensity estimation

We additionally project the large-scale galaxies into tomographically binned overdensity bins. To do this, we separate them into the photo-z bins defined in Table 1 and project to 2+1 dimensions as described in Sec. 2.2.1.

3 PIPELINE

Our pipeline is as follows. We:

- (i) Split the small-scale LRG galaxies into N redshift bins, where N is some reasonable number that should approach the maximum signal-to-noise while remaining computationally tractable. We explore N = 4, 8, 16, and define the redshift bins using discrete cuts on the photometric redshift estimate z^{photo} ;
- (ii) Perform kSZ velocity reconstruction with the N small-scale LRG samples and the kSZ map using a quadratic estimator to get estimates of the radial velocity field $v_{\alpha}^{\rm kSZ}$ where $\alpha=1,\cdots,N$;
- (iii) Perform continuity-equation velocity reconstruction on the largescale LRG galaxies to get a three-dimensional velocity estimate $\vec{v}^{\text{cont}}(z, \hat{n})$;
- (iv) Project the radial component of the three-dimensional continuity velocity field into N two-dimensional bins v_{α}^{cont} ;

⁵ https://github.com/cosmodesi/pyrecon

⁶ We have explored performing the continuity-equation reconstruction on all bins together, but found poorer results on data than expected compared to simulations. This is at the expense of some signal-to-noise, but we defer more in-depth exploration to future work.

- (v) Measure the angular cross-correlation $\hat{C}_L^{v_{lpha}^{\rm kSZ}v_{eta}^{\rm cont}}$ and estimate its covariance matrix;
- covariance matrix; (vi) Compare $\hat{C}_{L}^{v_{\alpha}^{\rm EZZ}v_{\beta}^{\rm cont}}$ with theory.

We also compare with an alternate pipeline where, instead of performing continuity-equation velocity estimation, we:

- (iii-b) Project the three-dimensional photometric galaxy catalogue into N two-dimensional bins δ_{α}^{g} ;
- (iv-b) Measure the angular cross-correlation $\hat{C}_L^{v_{lpha}^{\rm kSZ}g_{eta}}$ and estimate its covariance matrix.

We perform the pipeline separately for the north galactic cap (NGC) and south galactic cap (SGC), and combine the final results assuming zero covariance.

We describe the different steps in more detail in several subsections below. Step (i) was described in Section 2.2.1. Step (ii) is described in Section 3.1. Steps (iii) and (iv) were described in Section 2.3.1, and step (iii-b) was described in Section 2.3.2. Steps (v) and (iv-b), are described in Sections 3.2 and 3.3. Step (vi) is described in Section 3.4.

Preliminaries and notation

Throughout this section, we use the notation $X_{\ell m}$ for the multipole moments of a real-space field X, which are related to the real-space field $X(\hat{n})$ by:

$$X_{\ell m} = \int X(\hat{n}) Y_{\ell m}^*(\hat{n}) d\Omega \tag{4}$$

where $Y_{\ell m}(\hat{n})$ are the spherical harmonic functions (with the star indicating their complex conjugate) and $d\Omega$ is the integration measure on the 2-sphere. The inverse of this transform is

$$X(\hat{n}) = \sum_{\ell=0}^{\infty} \sum_{m=-\ell}^{\ell} X_{\ell m} Y_{\ell m}(\hat{n}).$$
 (5)

We use upper-case L, M for the multipole moments when we refer to a field of which we are interested in the large scales, and lower-case ℓ , m when we refer to a field of which we are interested in the small scales.

In practice the upper-limit of the sum over ℓ in Equation (5) is cut off at some maximum ℓ which is set by the angular resolution. We use $\ell=3\times4096$ for our maximum ℓ for small-scale fields, as we are working in real-space with HEALPix maps of Nside = 4096.

The (co-)variance in a map X (or maps X, Z) as a function of scale is captured in the power spectrum C_{ℓ}^{XZ} , which can be estimated as follows:

$$C_{\ell}^{XZ} = \frac{1}{2\ell + 1} \sum_{m=0}^{m} X_{\ell m} Z_{\ell m}^{*}. \tag{6}$$

We will use the notation \tilde{X} to refer to a field created with inverse-variance filtering:

$$\tilde{X}_{\ell m} \equiv \frac{X_{\ell m}}{C_{\ell}^{XX}}.\tag{7}$$

In creating the inverse-variance filtered galaxy-overdensity maps δ_{α}^g and temperature map \tilde{T} we measure the power spectra $C_{\ell}^{g\alpha g\alpha}$ and C_{ℓ}^{TT} directly from the data; see Figs 2 and 5.

3.1 kSZ velocity reconstruction pipeline

We estimate the tomographically-binned projected large-scale velocity field from the small-scale temperature described in 2.1 and the small-scale galaxy overdensity measurement described in Section 2.2. Our pipeline is 2+1 dimensional in the sense that we work in two continuous angular dimensions on the sphere and one tomographically binned redshift dimension (labelled by Greek indices α), as opposed to 3 continuous dimensions. The tomographic kSZ velocity field estimator requires a small-scale tomographic galaxy overdensity measurement δ_{α}^g as well as the small-scale kSZ temperature measurement.

Aside from different choices about galaxy binning to be described below, our kSZ velocity reconstruction pipeline is described in McCarthy et al. (2025). It is based on the ReCCo pipeline of Cayuso et al. (2023), which implements real-space version of a quadratic estimator (QE) introduced in Deutsch et al. (2018). The QE itself followed closely the formalism of Okamoto & Hu (2003).

The theory of kSZ velocity reconstruction is described in Appendix B. While we refer the reader to Section 3.1 of McCarthy et al. (2025) for further details, the estimator is

$$(\hat{v}_{\alpha}^{\text{kSZ}})_{LM} = A_L^{\alpha} \left(\tilde{T}(\hat{n}) \zeta^{\alpha}(\hat{n}) \right)_{LM}. \tag{8}$$

Here, $\zeta^{\alpha}(\hat{n})$ is the galaxy overdensity map refiltered such that it approximates the expected optical depth distribution in bin α :

$$\zeta_{\ell m}^{\alpha} = C_{\ell}^{\tau g_{\alpha}} (\tilde{\delta_{\alpha}^{g}})_{\ell m} \tag{9}$$

where $C_\ell^{\tau g \alpha}$ is a model for the galaxy-electron cross correlation in bin α ; we describe our model in Section 4.1. Importantly, an incorrect model will lead to a biased velocity estimate; this bias is scale-independent and quantified by a quantity b_ν referred to as the "velocity bias" that will be marginalized over in our analysis.

The normalization A_L^{α} is given by

$$A_L^{\alpha} = (2L+1) \left(\sum_{\ell,\ell'} \frac{\left(f_{\ell\ell'L} C_{\ell'}^{\tau g_{\alpha}} \right)^2}{C_{\ell}^{TT} C_{\ell'}^{g_{\alpha}g_{\alpha}}} \right)^{-1}$$

$$\tag{10}$$

where

$$f_{\ell\ell'L} = \sqrt{\frac{(2\ell+1)(2\ell'+1)(2L+1)}{4\pi}} \begin{pmatrix} \ell & \ell' & L \\ 0 & 0 & 0 \end{pmatrix}$$
 (11)

with $\begin{pmatrix} \ell_1 & \ell_2 & \ell_3 \\ m_1 & m_2 & m_3 \end{pmatrix}$ the Wigner 3-J symbols. In practice, A_L^{α} is essentially scale-independent at the low Ls that we are interested in.

The auto power spectra of the reconstructed velocity estimates have a noise bias $N_L^{(0)}$. Assuming the filters used in the inverse-variance filtering accurately describe the two-point power in the maps, this is given in the ensemble average by

$$\left\langle \hat{v}_{\alpha,LM}^{\text{kSZ}} \hat{v}_{\beta,L'M'}^{\text{kSZ}} \right\rangle = \delta_{LL'} \delta_{MM'} \frac{A_L^{\alpha} A_L^{\beta}}{2L+1} \sum_{\ell,\ell'} \frac{(f_{\ell\ell'L})^2 C_{\ell'}^{\tau g_{\alpha}} C_{\ell'}^{\tau g_{\beta}} C_{\ell'}^{s_{\alpha}g_{\beta}}}{C_{\ell'}^{TT} C_{\ell'}^{g_{\alpha}g_{\alpha}} C_{\ell'}^{s_{\alpha}g_{\beta}}}$$

$$(12)$$

$$\equiv N_L^{(0),\alpha\beta}.\tag{13}$$

Note that for the equal-redshift auto correlation we have

$$N_L^{(0),\alpha\beta} = A_L^{\alpha} \equiv N_L^{(0),\alpha}. \tag{14}$$

We perform the velocity reconstruction separately in the north and south galactic caps. As we use the measured power spectra for the

filters, this means that we measure them separately on each region (see Figs 2 and 3). For homogeneous surveys, there would be no difference; however, the inhomogeneous noise properties of the ACT map and the slightly different $\frac{dN}{dz}$ of the north and south galaxies results in filters that are different on each region. In practice, this results in different $N_L^{(0)}$ in the different regions.

3.2 Angular cross correlation

We measure the angular cross-correlations $\hat{C}_L^{v_{lpha}^{\rm kSZ}v_{eta}^{\rm cont}}$ and $\hat{C}_L^{v_{lpha}^{\rm kSZ}g_{eta}}$, using a pymaster (Alonso et al. 2019) pipeline. pymaster is a python implementation of the MASTER algorithm (Hivon et al. 2002), which estimates a multipole-binned mask-decoupled power spectrum of two masked Gaussian fields. In Lai et al. (2025), a more optimal quadratic maximum likelihood (Tegmark & de Oliveira-Costa 2001; Kvasiuk et al. 2025) pipeline was implemented, leading to significant improvements in signal-to-noise (by an overall factor of \sim 2). We leave such an implementation and a detailed further study of this improvement to future work.

We measure the mask-decoupled \hat{C}_L s in multipole bins with bandwidths $\Delta L = 12$, with two multipole bins with $\Delta L = 3$ at very low L, i.e. bins with minimum Ls defined by $[0, 3, 6, 18, 24, \cdots]$. We do not use the lowest two bins in any analysis, taking an L_{\min} of 6. Our maximum multipole is the one with boundaries [42, 53], where our signal-to-noise is saturated. We have explored the stability of our signal on the size of ΔL and the minimum multipole analyzed.

3.3 Covariance estimation

We estimate the covariance between the \hat{C}_L s analytically using the pymaster implementation of the mask-decoupling of the simple "Knox formula" for the Gaussian covariance of the C_L s. This method requires an estimation of the true power in the maps. For this we use the measured power for the continuity equation velocity and galaxy maps, and the theoretical noise power $N_L^{(0),\alpha\beta}$ for the kSZ velocity maps (we find that, after masking tSZ clusters, the theoretical power agrees well with the observed power). We have checked that adding a signal covariance matrix to the theoretical noise estimation results in a negligible change in the covariance. We include all inter-bin covariances. In general, before mask decoupling,

$$\operatorname{Cov}(C_{L}^{\nu_{\alpha}^{kSZ}\nu_{\beta}^{\operatorname{cont}}}, C_{L'}^{\nu_{\gamma}^{kSZ}\nu_{\delta}^{\operatorname{cont}}}) = \frac{\delta_{LL'}}{(2L+1)f_{\operatorname{sky}}} \times \left(N_{L}^{(0),\alpha\gamma}C_{L}^{\nu_{\beta}^{\operatorname{cont}}\nu_{\delta}^{\operatorname{cont}}} + C_{L}^{\nu_{\alpha}^{\operatorname{cont}}\nu_{\delta}^{\operatorname{cont}}}C_{L}^{\nu_{\beta}^{\operatorname{cont}}\nu_{\gamma}^{\operatorname{kSZ}}}\right). \tag{15}$$

The second term in the brackets (the "cosmic variance term" depends on the signal; we have run our pipeline with and without a best-fit signal included in the covariance, and find that it makes negligible difference. The covariance of $C_L^{\nu_{\alpha}^{\rm KSZ}g_{\beta}}$ is computed similarly, but with $C_L^{\nu_{\beta}^{\rm cont}\nu_{\delta}^{\rm cont}}$ replaced with $C_L^{g_{\beta}g_{\delta}}$.

When we include the auto power spectrum of the kSZ velocity in

spec	χ^2 /ndof	PTE
$C_L^{v^{ m kSZ}_{v^{ m cont}}}$ (diagonal, NGC) $C_L^{v^{ m kSZ}_{v^{ m cont}}}$ (diagonal, SGC)	55.013188 / 64 58.408817 / 64	0.781 0.674
$C_L^{v^{ m kSZ}_{ m v^{cont}}}$ (full, NGC) $C_L^{v^{ m kSZ}_{ m v^{cont}}}$ (full, SGC)	994.06634 / 1024 994.62203 / 1024	0.743 0.739
$C_L^{v^{ m kSZ}g}$ (first off-diagonal, NGC) $C_L^{v^{ m kSZ}g}$ (first off-diagonal, SGC)	111.72567 / 128 110.8865 / 128	0.847 0.86
$C_L^{ u^{ ext{KSZ}}g}$ (full, NGC) $C_L^{ u^{ ext{KSZ}}g}$ (full, SGC)	1043.4999 / 1024 1031.0789 / 1024	0.329 0.432

Table 2. The PTEs of the χ^2 -to-zero for a nulled version of the dataset, where the redshifts of the small-scale galaxies are randomly shuffled. We list the χ^2 -to-zero over the number of degrees of freedom ndof, which we convert to a PTE assuming an analytic χ^2 distribution. In all cases there are 4 bandpowers in each spectrum, with an L_{\min} of 6 and an L_{\max} of 53. We list the PTE for our cross-correlation with the continuity equation velocity $(C_L^{v^{\rm kSZ}})^{\rm cont}$ as well as with the galaxy overdensity $(C_L^{v^{\rm kSZ}g})$, for the full inter-redshift-bin measurement ("full") as well as case when we look at just the redshift-space diagonals (ie, only the equal-redshift-bin correlations) for $C_L^{\rm vkSZ}{}_{\nu}^{\rm cont}$ and neighbouring bin cross spectra for $C_L^{v^{kSZ}g}$ ("first off-diagonal"). All PTEs are acceptable, indicating that our covariance matrix correctly describes the data according to this test.

the likelihood, we use

$$\operatorname{Cov}(C_{L}^{v_{\alpha}^{kSZ}v_{\beta}^{kSZ}}, C_{L'}^{v_{\gamma}^{kSZ}v_{\delta}^{kSZ}}) = \frac{\delta_{LL'}}{(2L+1)f_{\text{sky}}} \times \left(N_{L}^{(0),\alpha\gamma}N_{L}^{(0),\beta\delta} + N_{L}^{(0),\alpha\delta}N_{L}^{(0),\beta\gamma}\right). \tag{16}$$

The expression for the covariance of the auto power spectrum with the cross power spectrum is linear in the cosmic variance term:

$$\operatorname{Cov}(C_{L}^{\nu_{\alpha}^{kSZ}\nu_{\beta}^{kSZ}}, C_{L'}^{\nu_{\gamma}^{kSZ}\nu_{\delta}^{cont}}) = \frac{\delta_{LL'}}{(2L+1)f_{\text{sky}}} \times \left(N_{L}^{(0),\alpha\gamma}C_{L}^{\nu_{\beta}^{kSZ}\nu_{\delta}^{cont}} + N_{L}^{(0),\beta\gamma}C_{L}^{\nu_{\alpha}^{kSZ}\nu_{\delta}^{cont}}\right). \tag{17}$$

Again, we find that inclusion of this term is a negligible effect on our analysis.

We note that an analytical covariance with a theoretical power spectrum instead of the measured power may be preferable, or alternatively a covariance measured from simulations. However, given the requirement of many simulations for convergence, we defer such a study to future work, although we note that the converged simulationbased covariance used in McCarthy et al. (2025) was very close to the analogous theoretical estimate.

We test the covariance matrix by performing null tests. In particular, we run our pipeline on our dataset with the redshifts of the small-scale galaxies randomly shuffled; in this case we should detect a signal consistent with zero. We calculate the overall χ^2 with respect to zero, and convert this into a probability-to-exceed (PTE) assuming an analytical χ^2 distribution with number of degrees of freedom given by the number of datapoints. The PTEs are perfectly acceptable in all cases; we list them in Table 2.

3.4 Likelihood and comparison with theory

We compare our measured bandpowers $\hat{C}_L^{v_{\alpha}^{kSZ}v_{\beta}^{cont}}$ to theory $C_L^{v_{\alpha}^{kSZ}v_{\beta}^{cont}}$ (θ) (where θ is a parameter vector) using a Gaussian likelihood for the bandpowers

$$-2 \ln \mathcal{L}(\hat{C}_{L}^{\nu_{\alpha}^{kSZ}\nu_{\beta}^{cont}}, \theta) = \left(\hat{C}_{L}^{\nu_{\alpha}^{kSZ}\nu_{\beta}^{cont}} - C_{L}^{\nu_{\alpha}^{kSZ}\nu_{\beta}^{cont}}(\theta)\right) \mathbb{C}^{-1}$$

$$\cdot \left(\hat{C}_{L}^{\nu_{\alpha}^{kSZ}\nu_{\beta}^{cont}} - C_{L}^{\nu_{\alpha}^{kSZ}\nu_{\beta}^{cont}}(\theta)\right)$$

$$\equiv \chi^{2},$$

$$(19)$$

where \mathbb{C} is the covariance matrix of \hat{C} . The theory is described in Section 4. The parameter vector contains parameters encompassing the velocity bias b_{ν} , the galaxy bias b_{g} , and cosmology f_{NL} (with all other cosmological parameters assumed to be degenerate with b_{ν}). In practice, we look at four models: two fixed-cosmology model where $f_{NL}=0$, and two varying cosmology models where f_{NL} is freed. In each case, we consider one case where there is one b_{ν} parameter that is the same in all redshift bins, and one case where the velocity bias is allowed to vary independently in each redshift bin. In the latter case there are N velocity bias parameters which we label as b_{ν}^{α} (recall that N is the number of redshift bins).

We always allow N independent galaxy bias parameters b_g^α . The galaxy bias is well-known, and so we take tight priors $b_g=2.1\pm0.1, 2.1\pm0.1, 2.3\pm0.1, 2.4\pm0.1$ in to the redshift ranges $0.4 < z^{\rm photo} < 0.545, 0.545 < z^{\rm photo} < 0.713, 0.713 < z^{\rm photo} < 0.885, 0.885 < z^{\rm photo} < 0.101$ respectively, corresponding to the bins and measurements of Kim et al. (2024) and Sailer et al. (2025), which analyzed the cross-correlation of the clustering of these galaxies with Planck and ACT CMB lensing (Carron et al. 2022; Qu et al. 2024; Madhavacheril et al. 2024; MacCrann et al. 2024). Explicitly, in the 16-bin case, we use the first prior in the first four bins (which are created from rebinning the $0.4 < z^{\rm photo} < 0.545$ bin, and the second prior in the second four bins, etc.

We perform a Markov chain Monte–Carlo (MCMC) sampling, using Cobaya (Torrado & Lewis 2019, 2021). We minimize the likelihood using the BOBYQA minimizer (M.J.D. 2009; Cartis et al. 2018a,b) implemented in Cobaya to find the best-fit parameters. We visualize our posteriors and compute summary statistics with getDist⁷ (Lewis 2019).

When we quote signal-to-noise ratios, we use the mean b_{ν} from the one-parameter model from the chains divided by the errorbar estimated from its covariance: SNR = $\frac{\bar{b}_{\nu}}{\sigma(b_{\nu})}$. We have checked in many cases that this agrees with the SNR estimated of Lai et al. (2025), where the separate estimates of b_{ν}^{α} are co-added using their covariance matrix, and also that this agrees with the SNR quoted in McCarthy et al. (2025), which computed the improvement in χ^2 between the best-fit point and the null case and converted the equivalent probability-to-exceed (PTE) to a Gaussian number of sigma with the same PTE.

4 THEORY

In this Section we describe the theory quantities that we require to interpret our observables. In all cosmological calculations, we use the *Planck* 2018 Λ CDM cosmology (Planck Collaboration 2020a), where $H_0 \equiv 100 \, h \, \text{km/s/Mpc} = 67.66 \, \text{km/s/Mpc}$ is the Hubble

parameter; $\Omega_b h^2 = 0.02242$ is the physical density of baryons today; $\Omega_c h^2 = 0.11933$ is the physical density of cold dark matter today; and $\ln(10^{10}A_s) = 3.047$ and $n_s = 0.9665$, with and A_s and n_s the amplitude and spectral index of scalar fluctuations respectively (at a pivot scale of $0.05\,\mathrm{Mpc}^{-1}$).

Two distinct aspects of theory modelling are required for this measurement: an astrophsyical model for the small-scale $C_\ell^{g\tau}$ that we use to create the kSZ velocity estimate, and cosmological models for the large scale observables $C_L^{v^{kSZ}g}$ and $C_L^{v^{kSZ}v^{cont}}$. We discuss the small-scale $C_\ell^{g\tau}$ model in Section 4.1 and the large-scale cosmological modeling in Section 4.2. Finally, we present our model for scale-dependent bias induced by non-Gaussianity in Section 4.3.

4.1 Small-scale theory: galaxy-electron model

4.1.1 Galaxy-electron model

kSZ velocity reconstruction requires a model for $C_\ell^{\tau g}$, to compute the normalization A_L^{α} (see Equation (10)). In previous work, we modeled this using a halo model (for a review, see Cooray & Sheth (2002)). In this work, we bypass the halo-model calculation and use filters measured directly from $C_\ell^{g\tau}$ in simulations created from N-body simulations populated with LRG-like galaxies using a halo occupation distribution (HOD) and with a τ signal matched to hydrodynamic simulations. We create galaxy overdensity and τ maps from the simulations and cross-correlate them to directly estimate $C_\ell^{g\tau}$. The N-body simulations we use are the Abacus Summit light cone

The N-body simulations we use are the AbacusSummit light cone simulations (Maksimova et al. 2021; Hadzhiyska et al. 2022); we describe these, and our creation of galaxy and tau maps from them, in Appendix C.

We show the $C_{\ell}^{g\tau}$ in Fig. 6.

4.1.2 Optical depth bias

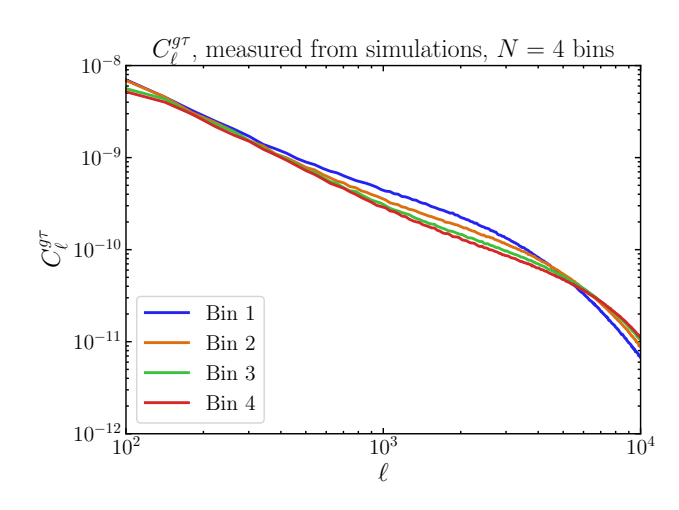
The assumption of a model for $C_\ell^{\tau g \alpha}$ results in a degeneracy: any parameter constraints we infer from $v_\alpha^{\rm kSZ}$ are degenerate with mismodelling of this quantity. While there is hope in the future of calibrating this quantity with direct tracers of the electrons such as fast radio bursts (Madhavacheril et al. 2019) or anisotropic CMB screening (Coulton et al. 2024b; Schutt et al. 2024; Hadzhiyska et al. 2025a), for now we use the fact that the optical depth bias is a scale-independent multiplicative quantity on large scales to define N optical depth bias parameters b_ν^α (where α runs over 1 to the number of redshift bins N). If the data are not sufficiently constraining, these N parameters can be condensed to one parameter b_ν . In our previous work (McCarthy et al. 2025) we quoted an "amplitude parameter" A; this is simply different notation for b_ν and in this work we update to b_ν and b_ν^α for consistency with other works in the literature.

The expected value of b_v^α given the true underlying galaxy-optical

⁷ https://getdist.readthedocs.io/en/latest/

⁸ We note that since the beginning of this work, the most precise cosmological parameters have been superseded by the ACT DR6+*Planck* cosmology (Louis et al. 2025). The small change in the cosmology would have negligible impact in our work.

⁹ The scale-dependence of b_{ν}^{α} has been tested on simulations (Giri & Smith 2022; Cayuso et al. 2023), with (Cayuso et al. 2023) finding that b_{ν}^{α} was scale-independent at multipoles L < 200.



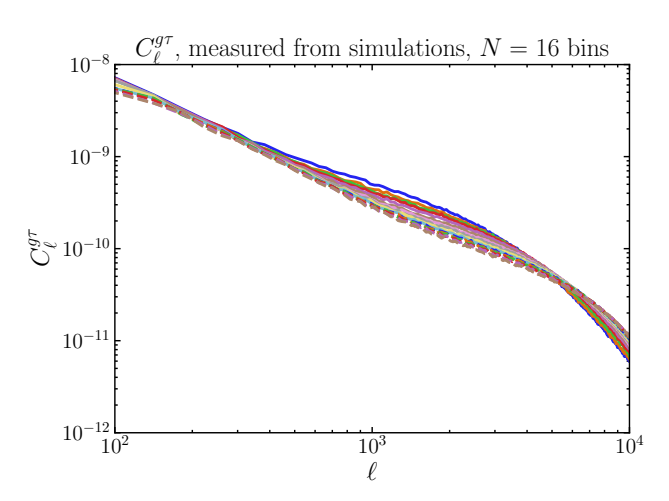


Figure 6. The $C_\ell^{g\tau}$ model we use in our filters. These are measured from the abacus HOD and τ simulations. We measure this at every ℓ , but for visualization purposes, we have binned them in ℓ space with a width $\Delta \ell = 400$.

depth correlation $\left[C_{\ell}^{\tau g_{\alpha}}\right]^{\text{true}}$ is

$$b_{v}^{\alpha} \simeq \frac{\left(\sum_{\ell} \frac{(2\ell+1)C_{\ell}^{\tau g \alpha} \left[C_{\ell}^{\tau g \alpha}\right]^{\text{true}}}{C_{\ell}^{TT} C_{\ell}^{g \alpha g \alpha}}\right)}{\left(\sum_{\ell} \frac{(2\ell+1)\left(C_{\ell}^{\tau g \alpha}\right)^{2}}{C_{\ell}^{TT} C_{\ell}^{g \alpha g \alpha}}\right)}.$$
 (20)

It is important to note that this depends on the details of the CMB dataset through C_ℓ^{TT} (containing foregrounds, instrumental noise, etc) and the details of the galaxy survey through the definition of the redshift-binning as well as through $C_\ell^{g\alpha g\alpha}$ (containing shot noise, galaxy bias, etc). Care should therefore be taken when comparing the measurement of b_ν from different data combinations and analysis choices.

Any cosmological constraints from kSZ velocity reconstruction should be marginalized over b_{ν} . Thus, with low-precision measurements of b_{ν} , it is difficult to use the kSZ-reconstructed velocity to place constraints on scale-independent quantities like growth; much of the interest in the signal will be for parameters which induce a scale-dependence like local primordial non-Gaussianity (Dalal et al. 2008; Münchmeyer et al. 2019).

4.2 Large-scale theory: velocity and galaxy power spectra

4.2.1 Velocity-velocity power specrum

We measure the cross-correlation between the kSZ-reconstructed radial velocity \hat{v}_{α}^{kSZ} and the continuity-equation reconstructed radial velocity \hat{v}_{α}^{cont} . Each of these velocity fields is a projection of the true three-dimensional radial velocity field $\vec{v}(\chi,\hat{n})$ with \hat{v}_{α}^{kSZ} following the projection kernels stated in Equations (B13) and \hat{v}_{α}^{cont} defined in (3). Assuming perfect reconstruction in both cases, we can model both as a projection of the underlying radial velocity field with the same redshift kernel:

$$v_{\alpha}(\hat{n}) = \int d\chi W^{\alpha}(\chi) v_r(\chi, \hat{n}), \tag{21}$$

where $W^{\alpha}(\chi)$ is the normalized redshift distribution of the galaxies in the bin α :

$$W^{\alpha}(\chi) = \frac{\frac{dN^{\alpha}}{d\chi}}{\int \frac{dN^{\alpha}}{d\chi} d\chi}.$$
 (22)

The angular two-point correlation function of the projected radial velocities is modelled as

$$C_L^{\nu\alpha\nu\beta} = \int d\chi_1 d\chi_2 W^{\alpha}(\chi_1) W^{\beta}(\chi_2)$$

$$\times \int \frac{k^2 dk}{(2\pi)^3} \mathcal{K}_L^{\nu}(\chi_1, k) \mathcal{K}_L^{\nu}(\chi_2, k) P_{\text{lin}}(\chi_1, \chi_2, k), \tag{23}$$

where $P_{\text{lin}}(\chi_1, \chi_2, k)$ is the linear matter power spectrum and the velocity kernel $\mathcal{K}_L^{\nu}(\chi, k)$ is given by

$$\mathcal{K}_{L}^{\nu}(\chi, k) = 4\pi i^{L} \frac{f(\chi)H(\chi)a(\chi)}{(2L+1)k} (Lj_{L-1}(k\chi) - (L+1)j_{L+1}(k\chi)), \tag{24}$$

where $j_L(x)$ are the Bessel functions of degree L; $f(\chi) \equiv \frac{d \ln \delta}{d \ln a}$ (with δ the dark matter overdensity and a the scale factor) is the growth rate; and $H(\chi)$ is the Hubble parameter at χ .

4.2.2 Velocity-continuity equation velocity power spectrum

To estimate the velocity field from the large-scale galaxy distribution, we solve the redshift-space continuity equation (Equation (25)), which we restate here:

$$\vec{\nabla} \cdot \vec{v}^{\text{cont}} + \frac{f}{b_{\varrho}} \vec{\nabla} \cdot \left[\left(\vec{v}^{\text{cont}} \cdot \hat{n} \right) \hat{n} \right] = -aHf \frac{\delta^g}{b_{\varrho}}, \tag{25}$$

where b_g is an estimate of the galaxy bias. Thus the continuity equation velocity which we estimate is dependent on this galaxy bias estimate, and contains galaxy bias information, which is often suppressed when writing v^{cont} . Restoring this, and neglecting the redshift space distortion (RSD) term (which is the second term on the left hand side of equation (25)), we see that the continuity equation velocity is related to the true velocity according to

$$\vec{v}^{\text{cont}} = \frac{b_g(\chi, k)}{b_g^{\text{fid}}} \vec{v}^{\text{true}},\tag{26}$$

where \vec{v}^{true} is the true underlying velocity field, b_g^{fid} is the fiducial bias chosen for the velocity reconstruction, and $b_g(\chi, k)$ is the true bias of the galaxies, which could have both redshift and scale dependence. Thus, the velocity-continuity equation velocity power spectrum is in

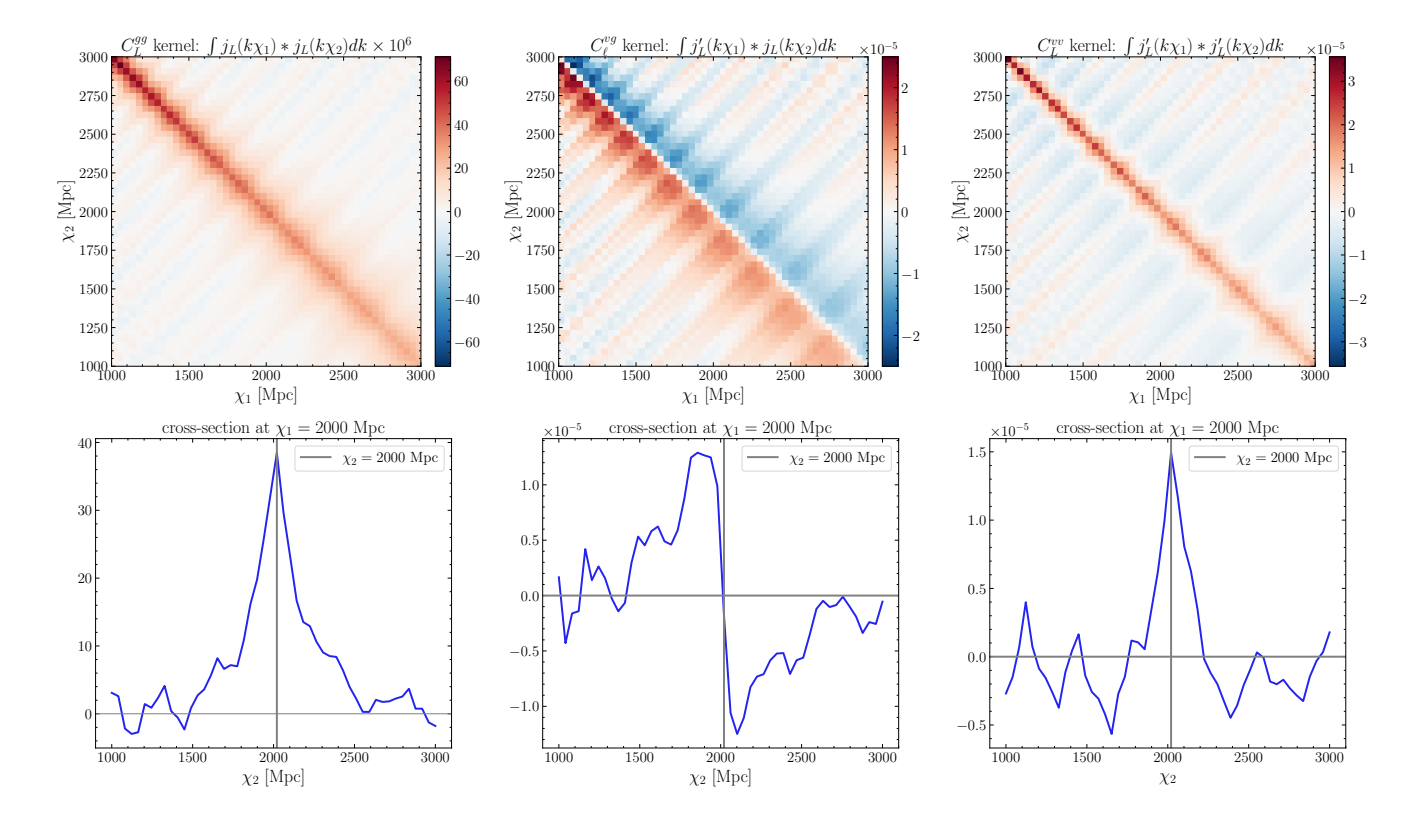


Figure 7. The structure of the (χ_1, χ_2) kernels used to evaluate C_ℓ^{gg} , C_ℓ^{gv} , and C_ℓ^{vv} . The C_ℓ^{gv} kernel displays a clear dipolar nature, peaking at non-local regions in the (χ_1, χ_2) plane. The C_ℓ^{gg} and C_ℓ^{vv} kernels are local and peak in the equal-redshift $\chi_1 = \chi_2$.

fact

$$C_L^{\nu_{\alpha}\nu_{\beta}^{\text{cont}}} = \int d\chi_1 d\chi_2 W^{\alpha}(\chi_1) W^{\beta}(\chi_2) \int \frac{k^2 dk}{(2\pi)^3} \times \frac{b_g(\chi_2, k)}{b_g^{\text{fig}}} \mathcal{K}_L^{\nu}(\chi_1, k) \mathcal{K}_L^{\nu}(\chi_2, k) P_{\text{lin}}(\chi_1, \chi_2, k).$$
(27)

This modelling assumes perfect continuity-equation velocity reconstruction. However, as our pipeline is performed on imperfect data—with a notable problem being the photo-z uncertainty of the data—further modelling is required. In order to incorporate effects of such properties of the data on the signal, we use simulations to calibrate a transfer function T_L such that our final model is

$$C_L^{\nu_\alpha \hat{\nu}_\beta^{\rm cont}} = T_L^{\alpha\beta} C_L^{\nu_\alpha \nu_\beta^{\rm cont}}. \tag{28}$$

We present the simulations and the transfer function in Section (5).

4.2.3 kSZ velocity-continuity equation velocity power spectrum

The kSZ velocity is modeled as scale-independent bias times the true velocity:

$$v^{\text{KSZ}} = b_{v}^{\alpha} v^{\text{true}}, \tag{29}$$

where b_{ν}^{α} is the kSZ velocity bias that arises due to the mismodelling of $C_{\ell}^{\tau g}$. Thus the full expression we use for the kSZ velocity-continuity equation velocity power spectrum is

$$C_L^{\nu_{\alpha}^{kSZ}\hat{\nu}_{\beta}^{\text{cont}}} = b_{\nu}^{\alpha} C_L^{\nu_{\alpha}\hat{\nu}_{\beta}^{\text{cont}}}.$$
 (30)

In practice, unless scale-dependence is being constrained, the misspecification of the linear bias $b_g^{\rm fid}$ is degenerate with the kSZ velocity bias b_v^{α} at the level of $C_L^{\nu^{\rm kSZ}\nu^{\rm cont}}$.

4.2.4 Velocity-galaxy power spectrum

The cross power spectrum between galaxies and true underlying binned radial velocity is

$$C_L^{\nu\alpha g\beta} = \int d\chi_1 d\chi_2 W^{\alpha}(\chi_1) W^{\beta}(\chi_2)$$

$$\times \int \frac{k^2 dk}{(2\pi)^3} \mathcal{K}_L^{\nu}(\chi_1, k) j_L(k\chi_2) b_g^{\beta}(\chi_2, k) P_{\text{lin}}(\chi_1, \chi_2, k),$$
(31)

where $b_g^{\alpha}(\chi_2, k)$ is the linear galaxy bias of the galaxies in redshift bin α at χ_2 , which could possibly depend on scale k.

4.2.5 kSZ velocity-galaxy power spectrum

The power spectrum between the kSZ-reconstructed velocity and the galaxies is

$$C_L^{\nu_{\alpha}^{kSZ}g\beta} = b_{\nu}^{\alpha} C_L^{\nu_{\alpha}g\beta}. \tag{32}$$

Just as for $C_L^{\nu^{\rm kSZ} \nu^{\rm cont}}$, misspecification in galaxy bias is degenerate with the velocity bias at the level of $C_L^{\nu^{\rm kSZ} g}$.

4.2.6 Implementation of the theory

We calculate the large-scale theory observables with a modified version of ReCCO (Cayuso et al. 2023), ¹⁰ which uses CAMB (Lewis et al. 2000)¹¹ to compute background cosmological quantities, the linear matter power spectrum, and perturbation transfer functions.

On the extremely large scales of interest, the widely-used Limber approximation (Limber 1953) is extremely poor. We use the beyond-Limber corrections of Fang et al. (2020) to compute the full expressions (23) and (31); the implementation is described in detail in Appendix A of Cayuso et al. (2023).

4.2.7 Redshift-structure of the theory

Due to the integral over spherical Bessel functions and their derivatives 12 , an interesting structure of C_L^{vg} and C_L^{vv} emerges in redshift space. The velocity-galaxy signal is exactly zero at $\chi_1=\chi_2$, and exhibits a dipolar nature. Thus the $C_L^{v\alpha s\beta}$ signal peaks on the off-diagonals $(\alpha \neq \beta)$. The $C_L^{v\alpha v\beta}$ and $C_L^{g\alpha g\beta}$ signals peak on the equal-redshift diagonal. This structure is illustrated in Fig. 7. This structure is the direct result of the velocity and density modes being related by a derivative and thus out-of-phase with each other.

4.3 Scale-dependent bias induced by primordial non-Gaussianity

4.3.1 Introduction

Local primordial non-Gaussianity is a non-Gaussianity in the initial conditions of the Universe parametrized by $f_{\text{NL}}^{\text{loc}}$ of the type

$$\Phi(\vec{x}) = \phi(\vec{x}) + f_{\text{NL}}^{\text{loc}} \left(\phi(\vec{x}) - \langle \phi \rangle\right)^2, \tag{33}$$

where $\Phi(\vec{x})$ is the Newtonian potential at position \vec{x} and $\phi(\vec{x})$ is an underlying Gaussian field. Note that, as ϕ is of order $O(10^{-5})$, a value of $f_{\rm NL}^{\rm loc}$ of 1 in fact corresponds to a highly Gaussian field (hereafter we will rever to $f_{\rm NL}^{\rm loc}$ as $f_{\rm NL}$). Constraints on primordial non-Gaussianity are of great interest, as they can give insight into the physics of the early Universe. Local-type primordial non-Gaussianity in particular is sensitive to whether the process driving inflation involved one or multiple scalar fields, with scenarios of multi-field inflation generically leading to $f_{\rm NL} \sim O(1)$ (see, eg de Putter et al. 2017). All current measurements are consistent with Gaussian initial conditions, with the tightest constraints from measuring the bispectrum of the Planck CMB (Planck Collaboration et al. 2020b) giving $f_{NL} = -0.9 \pm 5.1$. Non-Gaussianity of other types is also consistent with zero.

Local-type non-Gaussianity leads to a distinct signature in the clustering galaxies on very large scales (Dalal et al. 2008), inducing a scale-dependent galaxy bias $b^g \to b^g + \frac{f_{\rm NL}}{k^2}(b^g - p)$, where b^g is the galaxy bias with respect to dark matter in a Gaussian scenario (which is scale-independent), and p is a parameter which depends on galaxy assembly history (for objects following a universal halo mass relation, p = 1). This unique signature has led to a significant large-scale-structure programme to constrain $f_{\rm NL}$. Reaching the errorbars $\sigma(f_{\rm NL}) \sim 1$ required to be sensitive to multi-field inflation will be difficult for two reasons: the difficulty of making robust large-scale

measurements, and the cosmic (or sample) variance limit inherent on large scales. Cross correlation measurements with unbiased¹³ (i.e., $b^g = 1$) tracers (such as the true velocity field or the CMB lensing potential) have been shown to be able to bypass the sample variance limit through sample variance cancellation (Seljak 2009): heuristically, by simultaneously measuring the biased power spectrum bP(k)and the unbiased power spectrum P(k) on the same area of sky, one can measure the non-stochastic quantity $\frac{bP(k)}{P(k)} = b$ and avoid the cosmic variance inherent in a measurement of the stochastic quantity P(k). This effect was shown to be very promising in the context of kSZ tomography in Münchmeyer et al. (2019) and Contreras et al. (2019); recently, forecasts were revisited in Tishue et al. (2025). It has also been realized that the large-scale measurements required to access very low k have many systematics and a cross-correlation alone measurement may be significantly more robust. This has led to many recent constraints from cross-correlation-alone measurements on f_{NL} , with the Integrated Sachs Wolfe effect (Giannantonio & Percival 2014), CMB lensing (McCarthy et al. 2023; Krolewski et al. 2024; Bermejo-Climent et al. 2025; Fabbian et al. 2025), and most recently the kSZ-reconstructed velocity (Krywonos et al. 2024; Laguë et al. 2025; Hotinli et al. 2025).

The tightest constraints from large-scale-structure remain autopower-spectrum constraints, with $f_{\rm NL} = -3.6^{+9.0}_{-9.1}$ from DESI DR1 LRGs and quasars (Chaussidon et al. 2025). The tightest constraints from the kSZ velocity-galaxy cross correlation come from the combination of ACT DR5 and DESI LRG data and give $f_{\rm NL} = -39^{+40}_{-33}$ (Hotinli et al. 2025).

4.3.2 Theory and modelling details

The precise effect of f_{NL} on the Gaussian bias is

$$b^g \to b^g + f_{\rm NL} \frac{3\Omega_m H_0^2}{k^2 T(k) D(z)} \delta_c(b^g - p), \tag{34}$$

where Ω_m is the mean density of matter today; H_0 is the Hubble constant; T(k) and D(z) are the transfer and growth functions of the density field, respectively, with T(k) normalized to 1 at low k and D(z) normalized such that $D(z) = \frac{1}{1+z}$ during matter domination; and δ_c is the critical overdensity above which objects undergo gravitational collapse. We take $\delta_c = 1.686$ and p = 1 (appropriate for objects which follow a Universal halo mass relation, like dark matter halos). To constrain $f_{\rm NL}$, we simply use this model for the bias in Equation (27).

We note that there is complete degeneracy between $f_{\rm NL}$ and p (or the b_{ϕ} parameter that quantifies the coupling of galaxies to the primordial potential) (Slosar et al. 2008; Barreira 2022). Exploration of this degeneracy is beyond the scope of this paper.

5 DEMONSTRATION OF OUR PIPELINE ON SIMULATIONS

We demonstrate and calibrate various aspects of our pipeline on the AbacusSummit light-cone simulations (Maksimova et al. 2021; Hadzhiyska et al. 2022). We describe these simulations in Appendix C.

We demonstrate the unbiased recovery of the true velocity (given the correct model for $C_\ell^{g\tau}$) in Section 5.1. As discussed in Section 4.2.3, the continuity-equation estimated velocity field is biased,

¹⁰ https://github.com/jcayuso/ReCCO

¹¹ https://camb.info

¹² Note that the expression in brackets Equation (24) is proportional to the derivative of a $j_L(k_X)$

¹³ or more generally, several differently-biased

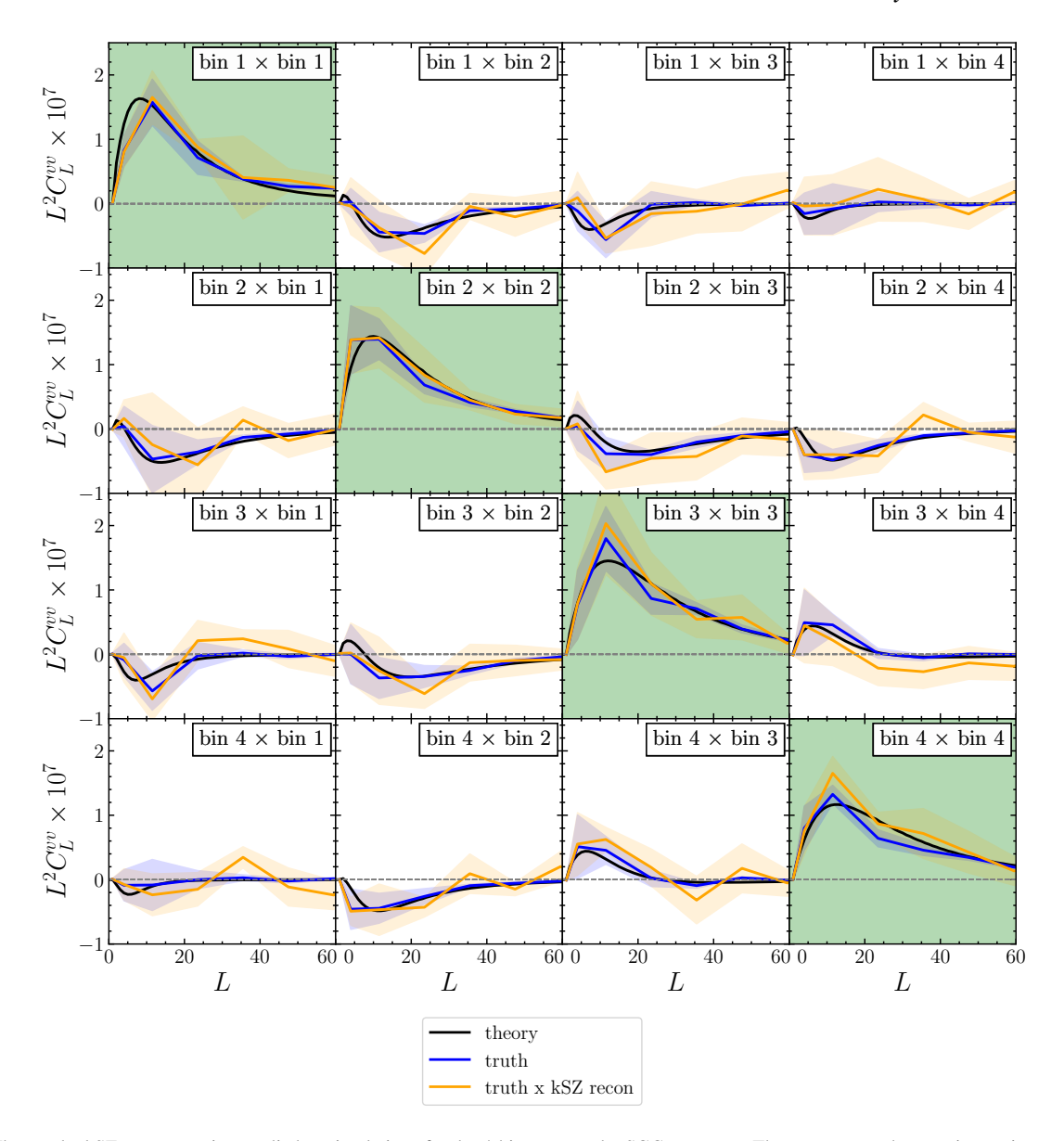


Figure 8. The results kSZ reconstruction applied to simulations for the 4-bin case on the SGC geometry. The reconstructed power is consistent with the true power. We show the true power spectrum and the cross spectrum of the kSZ reconstruction with truth; the kSZ reconstruction is noise dominated. The shaded bands show the 1σ regions. The diagonal is highlighted in green to guide the eye. The mean power spectrum of the true velocity field (blue) matches the theoretical prediction (black), providing a validation of our theory code; additionally, the kSZ-reconstructed velocity follows this closely as well.

and requires calibration on simulation; we discuss this in more detail and present the calibration in Section 5.2.

5.1 kSZ reconstruction demonstration

We treat our simulations like the dataset and run our kSZ velocity reconstruction pipeline (described in Section (3.1)). We add uncorrelated Gaussian noise to the kSZ map beforehand, in order to match the two-point power in the data. The results are shown in Fig. 8, where very good agreement is seen between the kSZ reconstruction and the truth. Thus we confirm that the QE makes an unbiased estimate of the velocity, in the case where $C_{\ell}^{g\tau}$ is perfectly known.

A validation of our theory code is also included in Fig. 8, as we include the theoretical prediction for $C_L^{\nu\nu}$ as well as the measured truth, and find that the theory describes the truth well.

5.2 Continuity equation velocity calibration

5.2.1 The need for simulation calibration of the theory

For the continuity equation velocity reconstruction part of our pipeline, we must understand the fidelity of the velocity reconstruction. In Ried Guachalla et al. (2024); Hadzhiyska et al. (2024), it was shown that for a DESI LRG-like galaxy sample with $\frac{\sigma_z}{(1+z)} \sim 0.02$, the velocity reconstruction has a correlation coefficient with the truth of ~ 0.3 . This correlation coefficient was defined as

$$r^{\nu_{\text{cont}},\nu_{\text{true}}} = \frac{\left\langle \nu_{\text{cont}}^{i} \nu_{\text{true}}^{i} \right\rangle}{\sqrt{\left\langle \nu_{\text{cont}}^{i} \nu_{\text{cont}}^{i} \right\rangle \left\langle \nu_{\text{true}}^{i} \nu_{\text{true}}^{i} \right\rangle}},$$
(35)

where the superscript i indicates velocity evaluated at the position of the object labelled by i, v_{true} is the true halo velocity, and v_{cont} is the continuity-equation-estimated velocity. The angular brackets

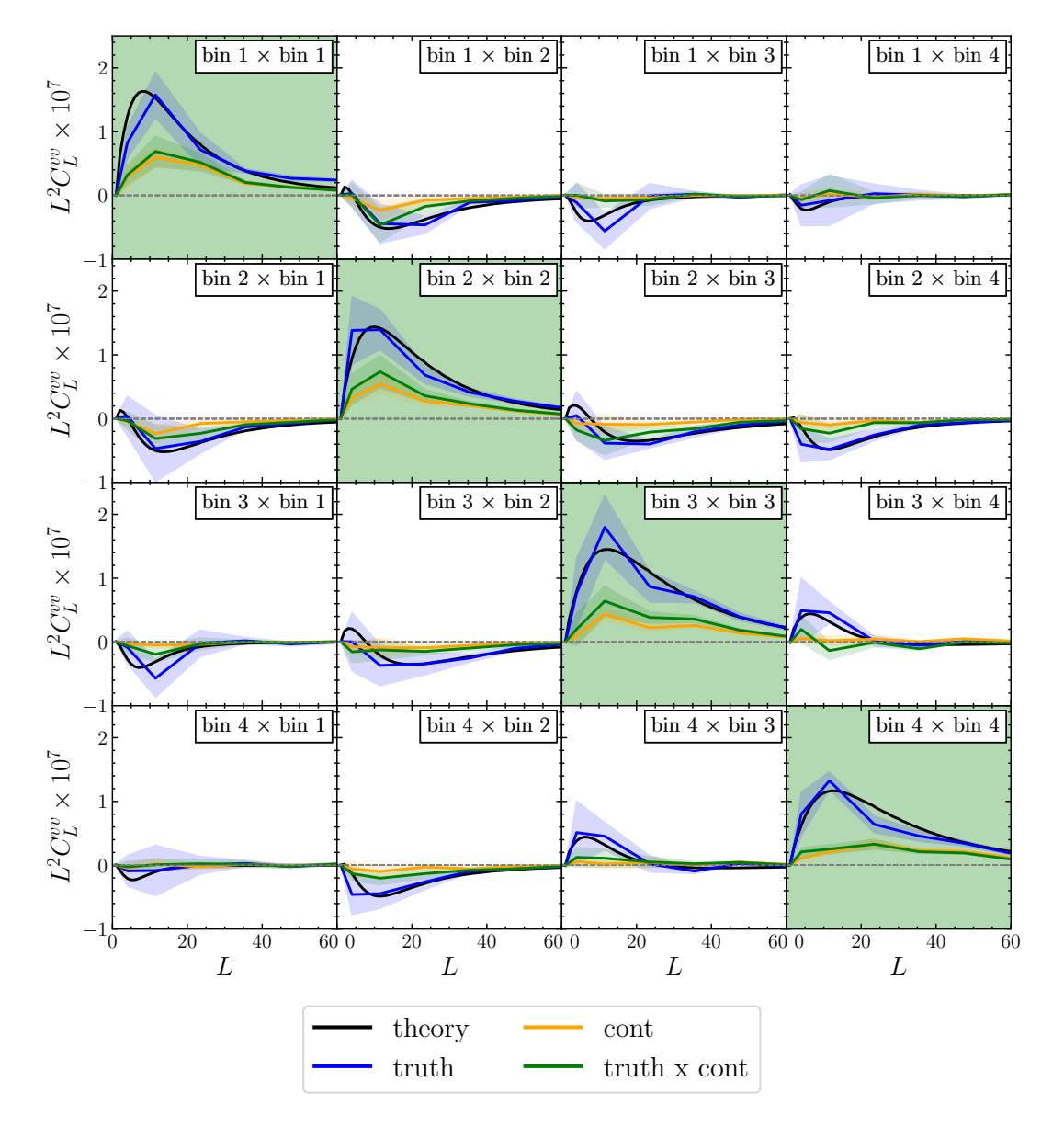


Figure 9. The $C_L^{\nu\nu}$ measured on the Abacus Summit lightcone simulations, for the N=4 tomographic bin case on the SGC, both before and after velocity reconstruction. The measured "true" power spectrum (ie, the power spectrum of v_{true}^{α}) is shown in blue, with the mean over the six quasi-independent simulations in solid lines and the 1σ region in shaded lines. The power spectrum of the continuity-equation reconstruction is shown in orange, and the cross-power spectrum of the truth and the reconstruction in green. We show a Λ CDM theory prediction for each case in black; we find good agreement between the theory and the truth. The diagonal is highlighted in green to guide the eye.

indicate the mean over all objects i. This quantity is an average over all scales; there was some exploration in Hadzhiyska et al. (2024) of the scale-dependence of r (see Fig. 6 therein), although not for photometric samples.

The correlation coefficient is not the quantity that we will need to quantify the performance of our continuity equation reconstruction. Our observable is $C_L^{\nu^{\rm cont}\nu^{\rm kSZ}}$, which we will for simplicity treat as $C_L^{\nu^{\rm cont}\nu^{\rm true}}$ (having validated our kSZ-reconstruction estimation in the previous section). Under the assumption that the continuity equation reconstruction creates an unbiased estimate of the velocity field, *i.e.*

$$v^{\text{cont}} = v^{\text{true}} + n. \tag{36}$$

where n is some noise, then even with a low correlation coefficient we can recover an unbiased measurement of the cross-power. Con-

versely, if the continuity-equation reconstruction creates a biased but noiseless estimate of the velocity field,

$$v^{\text{cont}} = Tv^{\text{true}},\tag{37}$$

with transfer function $T \neq 1$, a high correlation coefficient can still result in an in correct cross-correlation with the truth. In reality, we model the picture as somewhat in between:

$$v^{\text{cont}} = Tv^{\text{true}} + n, \tag{38}$$

where T quantifies the quality of the velocity reconstruction and allows for missing modes in the continuity-equation reconstruction, and n is all noise that is not correlated with v^{true} .

In order to understand the quantity $C_L^{\nu^{\rm cont} \nu^{\rm true}}$ it will be helpful to ignore (for now) any anisotropy in T (due to, e.g., relatively poor

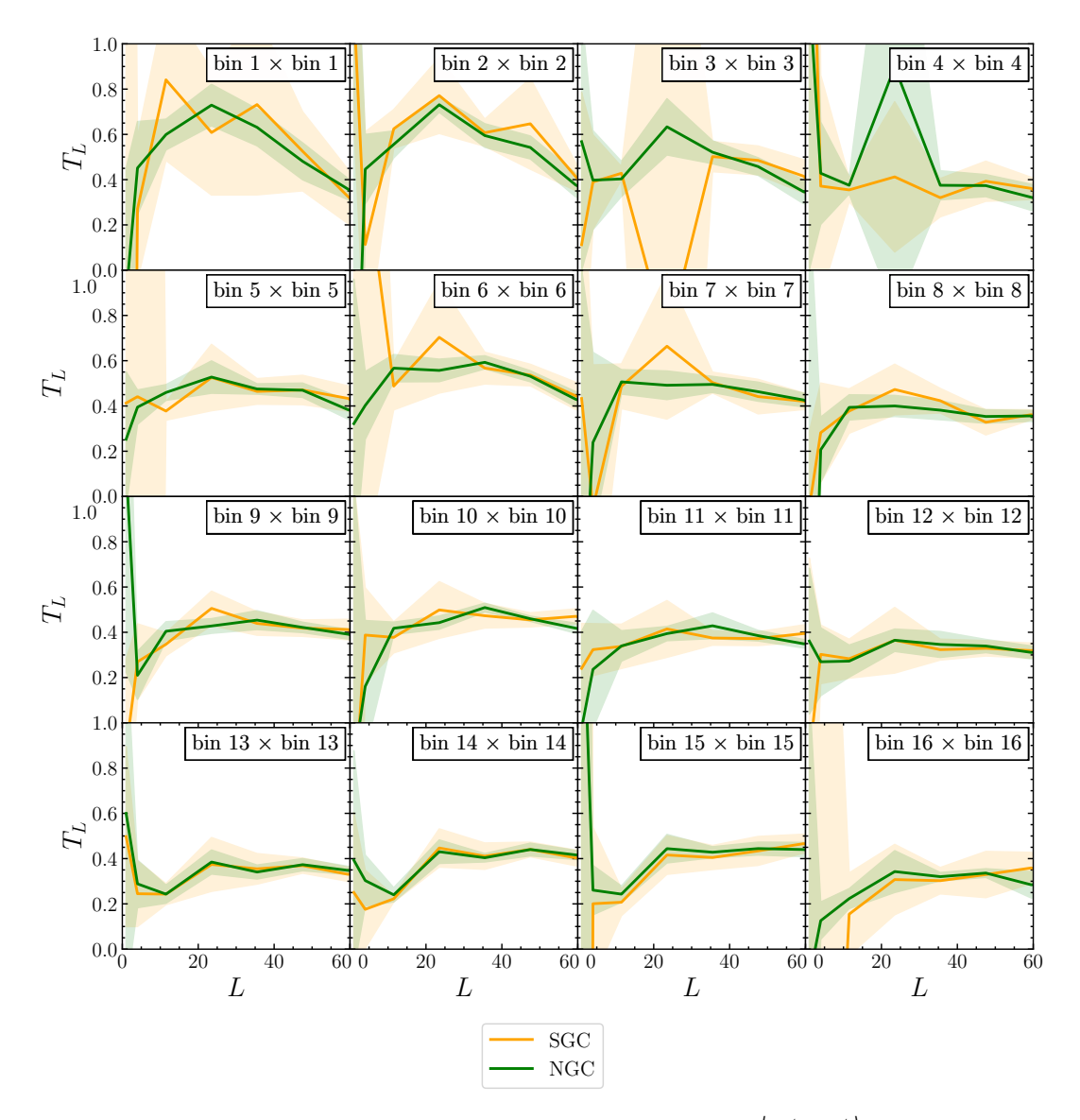


Figure 10. The transfer functions measured from the simulations with N=16 tomographic bins. We show $\left(\frac{C_L^{v_{\rm true}}v_{\rm cont}}{C_L^{v_{\rm true}}v_{\rm true}}\right)$ In general, a transfer function $T_L\sim 0.5$ is observed. We plot the mean over the six quasi-independent simulations with the standard deviation indicated with a shaded band.

performance near the edges of the footprint), and write

$$v_L^{\text{cont}} = T_L v_L^{\text{true}} + n_L. \tag{39}$$

We can then write for the cross-power spectrum we are interested in

$$C_L^{\nu^{\text{cont}}\nu^{\text{true}}} = T_L C_L^{\nu^{\text{true}}\nu^{\text{true}}}; \tag{40}$$

in order to interpret the $C_L^{\nu^{\rm kSZ}} \nu^{\rm cont}$ that we measure, it will be necessary (in the absence of deeper analytical understanding) to calibrate T_L from simulations.

Comparing the measured auto-correlation of the continuity-equation velocity reconstruction on data $C_L^{\nu^{\rm cont}}_{\nu}$ to the measured auto correlations of the simulations will serve as a check that our T_L is realistic.

Note that by using the same survey geometry for the simulations as we do for the data, any positional dependence in T should be appropriately encompassed into the average T_L that we calibrate (although in practice we find little dependence on survey geometry, at least at the current level of sensitivity).

Note that we have suppressed the redshift indices α in the above discussion, although we will need to calibrate a $T_L^{\alpha\beta}$ for all inter-bin cross correlations, in order to allow for appropriate redshift dependence in T_L . We describe our calibration of T_L in section 5.2.2.

5.2.2 Demonstration of continuity-equation reconstruction on simulations

We perform our continuity-equation reconstruction pipeline on the DESI DR10 LRG simulations described in Appendix C. We carry out the continuity-equation velocity reconstruction independently in each of the four larger redshift bins (with redshift boundaries shown in the first row of Table 1).

Before and after performing the continuity-equation velocity reconstruction, we project each bin to two dimensions and measure both mean true velocity and reconstructed velocity in each $N_{\rm side}=64$ HEALPix pixel, resulting in N $v_{\rm true}^{\alpha}$ and $v_{\rm cont}^{\alpha}$ maps respectively. We

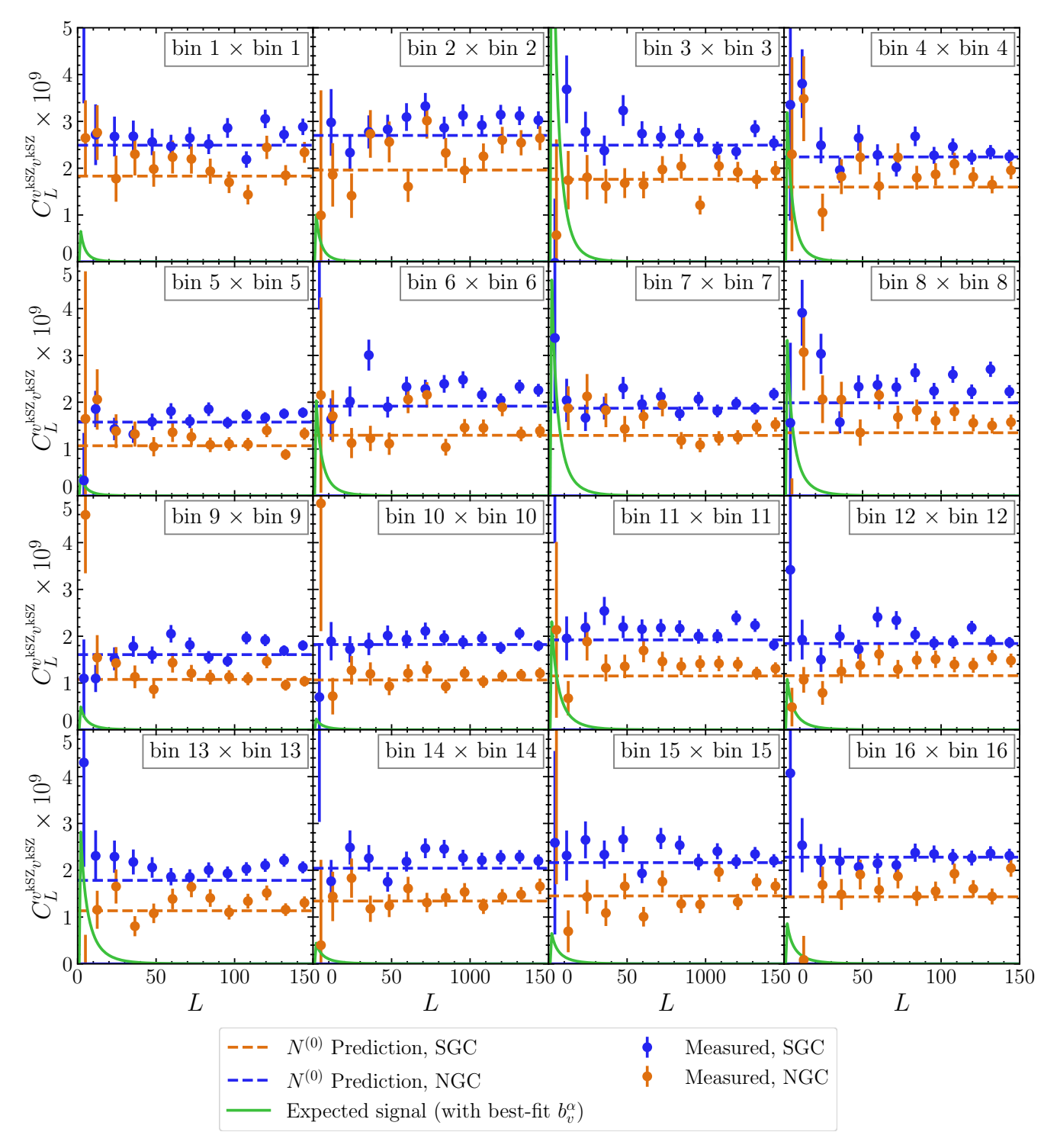


Figure 11. The measured auto power spectra of the kSZ-reconstructed velocity. The NGC region has lower $N^{(0)}$ bias due to the lower-variance CMB measurement in this region, as well as slightly higher galaxy number density in some redshift bins. In general, we find good agreement between the measured power and the analytical $N_L^{(0)}$ prediction (when masking galaxy clusters in the CMB+kSZ map before performing kSZ velocity reconstruction). The best-fit signal indicated uses the b_v^{α} from the best-fit model to the cross $C_v^{\text{kSZ}_v \text{cont}}$, as discussed in Section 6.2.

then measure $C_L^{v_{lpha}^{\rm true}}$, $C_L^{v_{lpha}^{\rm cont}}$, and $C_L^{v_{lpha}^{\rm true}}$, with a pymaster mask-decoupled estimate corresponding to the same bandpowers we use in the analysis.

The mean $C_L^{\nu_\alpha\nu_\beta}$ for the 4-bin case are shown in Fig. 9. In all

plots we include a theory estimate (see Section (23)); we find good agreement between our theory and the observed true velocity power spectrum. The relevant transfer functions are shown in Fig. 10 for the 16-bin case, for the $\alpha=\beta$ diagonal of $C_L^{\nu_\alpha\nu_\beta}$ equal-redshift correlations only.

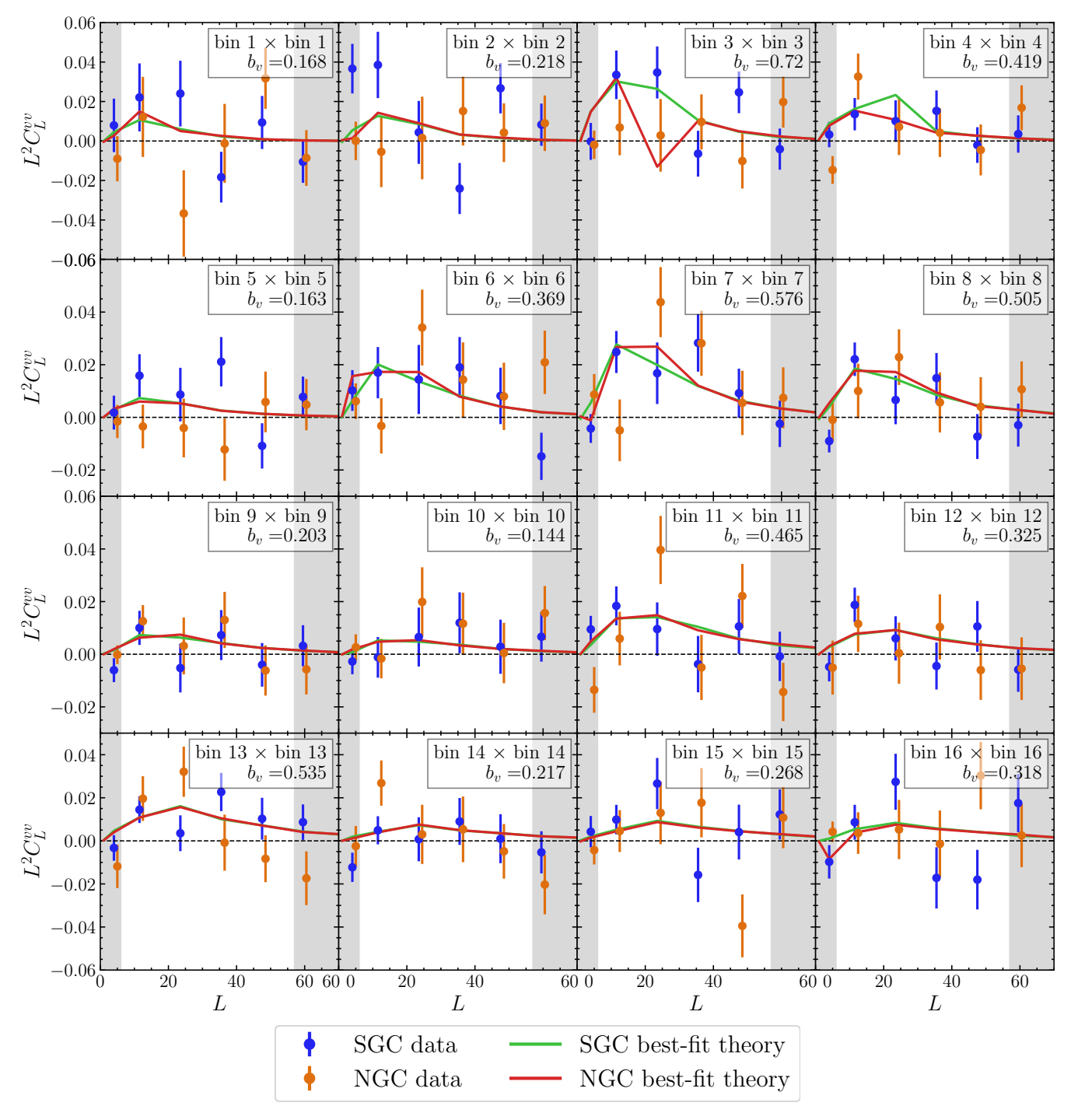


Figure 12. The baseline datapoints and the best-fit model. The best-fit model has 16 parameters b_{ν}^{α} and is jointly fit to all bins; the only difference in the model between the NGC and SGC cases is due to the different transfer functions. While there are a minority of cases where the transfer function looks unconverged, we have explored constraints dropping these bins and find negligible effect. We do not use the datapoints in the gray regions in any fits. For visualization purposes, we co-add these and display them in Fig. 13.

We also attempt to calibrate transfer functions for the inter-bin $(a \neq \beta)$ measurement, but found that these are unconverged for bins separated by a large distance (when the signal is zero). Thus we never include such bins in our analysis and restrict ourselves only to the diagonal $(\alpha = \beta)$ for our nominal analysis, although we also perform a fit for the case when we also include the first off-diagonal

 $(\alpha = \{\beta + 1, \beta - 1\})$). Most of the signal-to-noise is concentrated along or close to the diagonal.

5.2.3 Comparison to data

As we will use the T_L in our analysis, it is an important check to compare the equivalent quantity for the auto-spectrum to the data

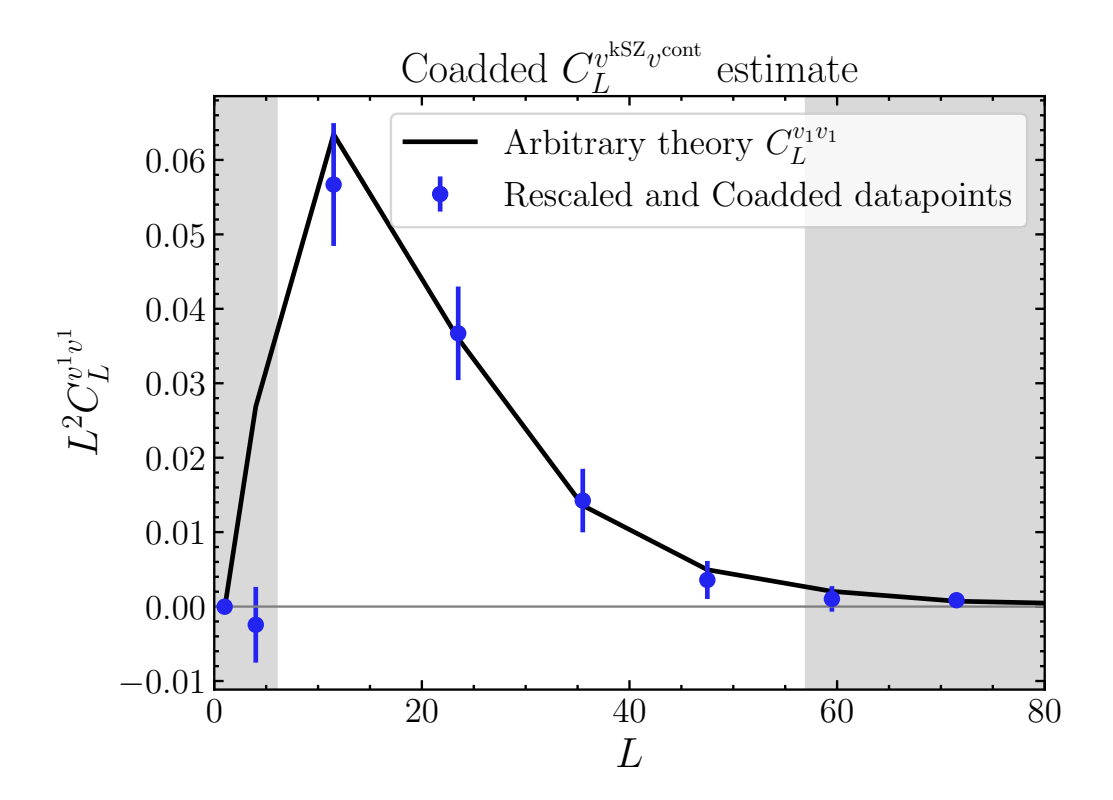


Figure 13. A co-add of the datapoints rescaled to estimate $C_L^{\nu_1\nu_1}$ (arbitrarily chosen). The scales not used in the analysis are indicated in the gray regions. We do use these points in the analysis; we analyze the points shown in Fig. 12.

products. In general, we find good consistency between the auto power spectra of the data and the simulations; we show in App. D the auto power spectra of the velocity field as measured on the data along with the mean measurement of the same signal from our simulations.

Fig. 12; we show a co-add of these points in Fig. 13. In Section 6.3 we open up the scale dependence of the model and constrain $f_{\rm NL}$. In Section 6.4 we include the auto spectrum of $\hat{v}^{\rm kSZ}$ in the analysis and report a 2.1σ measurement of the auto spectrum.

6 RESULTS

In this Section we present, discuss, and analyze our measurement. We make the measurement for an N=4, N=8, and N=16 tomographic bin case and compare these with each other for consistency. All plots in this section are for the baseline N=16 bin case, unless otherwise stated (note that sometimes we will plot examples for the N=4 bin case to improve readability).

Our "baseline" signal is $C_L^{\nu_{\alpha}^{\rm kSZ}} \nu_{\alpha}^{\rm cont}$ for a 16-bin case, where α runs from 1 to 16. For the larger more general $C_L^{\nu_{\alpha}^{\rm kSZ}} \nu_{\beta}^{\rm cont}$ signal there are 16×16 =256 inter-bin combinations; plots displaying these datapoints are difficult to read and interpret. Indeed, as most of the signal-to-noise is concentrated at equal-redshift ($\alpha = \beta$) diagonal, and because we find a good fit when we look at the diagonal-only case, we therefore primarily include only plots looking at the $\alpha = \beta$ equal-redshift diagonal. When we refer to our "baseline" dataset, we mean this $\alpha = \beta$ redshift diagonal. We defer a detailed analysis of the signal-to-noise penalty of removing the off-diagonal bins to future work.

In Section 6.1 we present the auto spectra of the kSZ-reconstructed velocities; these are shown in Fig. 11. In Section 6.2 we present and analyze the cross-power measurement between \hat{v}^{kSZ} and \hat{v}^{cont} ; our baseline datapoints, along with the best-fit model, are shown in

6.1 Auto power spectra of the kSZ reconstructions

The auto power spectra of our kSZ-estimated velocities are shown in Figure 11.

For reconstruction performed on Gaussian fields with zero signal, the kSZ velocity auto power-spectra contain only the reconstruction noise $N_L^{(0),\alpha}$. This is scale independent (on large scales) and, if the small-scale auto power of the fields matches the C_ℓ^{TT} and C_ℓ^{gg} filters used in the filtering and reconstruction normalization (i.e., if the filters used in the inverse-variance filtering of the maps and the theoretical computation of the normalization in (10) truly represent the data), can be analytically calculated to be

$$N_L^{(0),\alpha} = A_L^{\alpha},\tag{41}$$

where A_I^{α} is the normalization in Equation (10).

The assumptions of this analytical calculation are that all fields are Gaussian, and that $C_\ell^{gT}=0$ (i.e., that the temperature and galaxy fields are uncorrelated). Of course, a non-zero C_ℓ^{gT} is expected due to the correlation between the galaxies and foregrounds to the temperature field such as the CIB or tSZ effect; it is straightforward to include such an effect into the calculations both of the optimal estimator weights and of the resulting $N_L^{(0)}$ (the expressions are given in full in Cayuso et al. (2023)); however, this effect is subdominant as

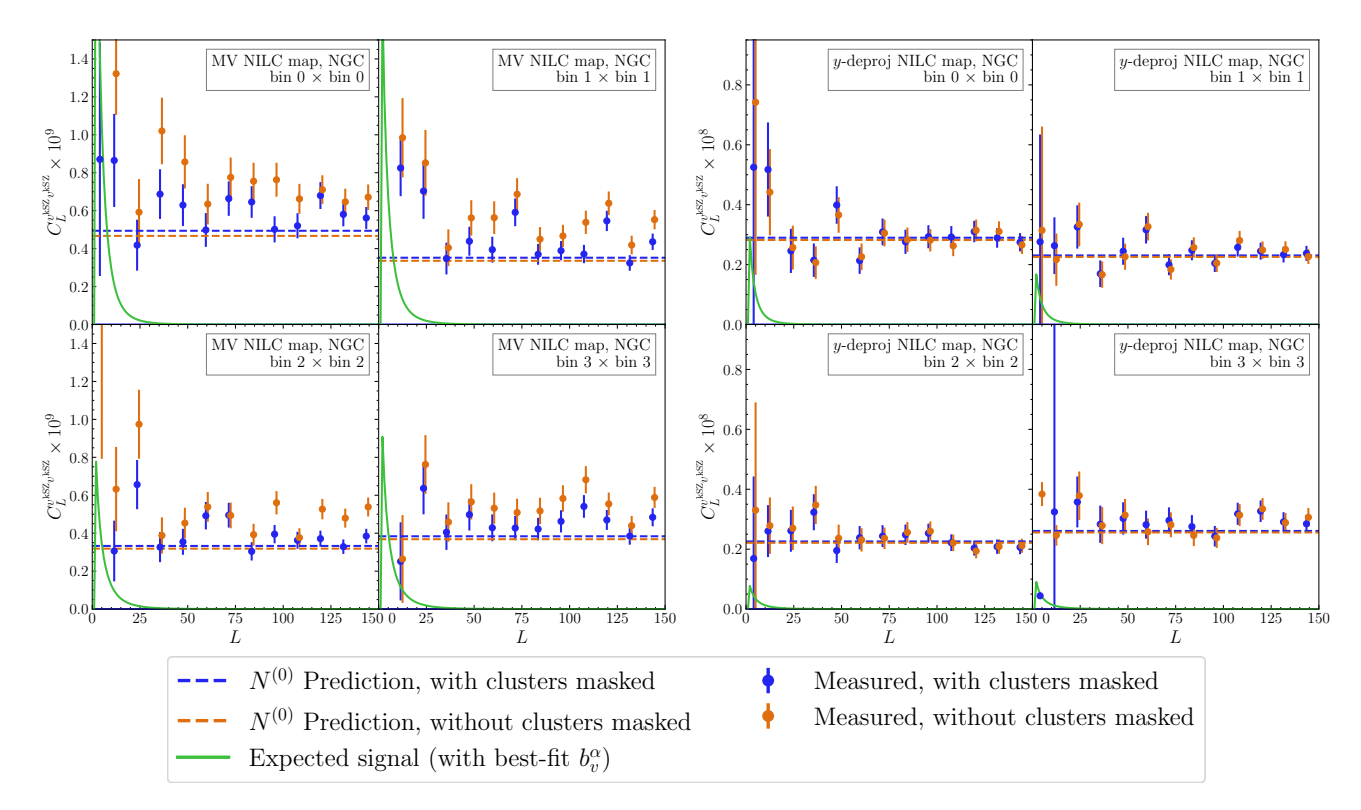


Figure 14. Auto power spectra of the kSZ reconstructed velocity for the N = 4 bin case on NGC. On the left we show the reconstruction with the unconstrained NILC, and on the right with the SZ-deprojected NILC; we show this only for NGC but conclusions are similar for SGC. We see that only for the unconstrained NILC when tSZ clusters are unmasked does the analytical prediction disagree with the measured power, indicating that removing these clusters (either through masking or deprojecting the tSZ effect) makes the analytical prediction much closer to the measurement. Note the significantly larger y-axis scale on the right; the SZ-deprojected velocity reconstructions have a factor of $\sim 5 \times$ more power than the MV NILC measurement. Note also that we have slightly offset the orange "measured, without clusters masked" points for slightly better comparison with the other points.

it is a correction of order $r_\ell \equiv \frac{C_\ell^{gT}}{\sqrt{C_\ell^{gg}C_\ell^{TT}}}$ which we have measured to be everywhere less than 2%. Thus, we neglect this correction. The remaining effect that we expect to observe from the non-zero C_ℓ^{gT} is a contribution to the estimator *monopole*. We remove this contribution and suppress any variance sourced by it by subtracting the observed monopole (estimated on the sky area available) before making any auto- and cross-power spectrum measurements.

Previous work (Bloch & Johnson 2024; McCarthy et al. 2025; Lai et al. 2025) found an offset of order 10 - 70% between the theory prediction for noise and the measured high-L power (where in the context of $C_L^{\nu\nu}$ high-L now means $L > \sim 50$, where no signal is expected, and the measured power was always higher than the prediction). ¹⁴ The noise amplitude had to be separately calibrated in the estimation of the covariance (in all of these works). For McCarthy et al. (2025) we performed some tests replacing either the galaxy or the temperature data with simulations which matched the power spectra of the data; we found that in both cases, the measured auto spectra agreed much more closely with the analytical prediction. Given that the kSZ reconstruction auto power spectrum is a trispectrum of the form $\langle T^S T^S \delta^S \delta^S \rangle$, our simulation tests suggested that this was caused by a bias of the form $\langle FG^SFG^S\delta^S \rangle$, where FG^S is some smal-scale foreground to the temperature measurement that is correlated with the galaxies. As the Gaussian contribution from C_{ℓ}^{gT}

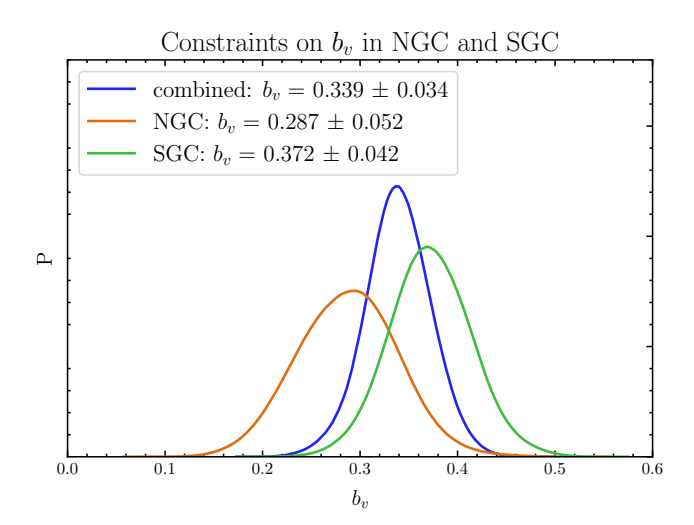


Figure 15. The velocity bias b_v inferred on NGC, SGC, and their combination. The NGC and SGC results are consistent. Our combined measurement is $b_v = 0.339 \pm 0.034$.

is subdominant (as discussed above), we expected this to be from the connected part of this trispectrum.

Interestingly, we find that this offset is significantly mitigated by the masking of tSZ clusters. We demonstrate this in Fig. 14 for the N=4 case in Appendix F for the N=16 case. We also show in Fig. 14 that deprojecting the tSZ also removes the offset between

¹⁴ The disagreement in (Bloch & Johnson 2024) can be eliminated with a more accurate estimation of the Planck temperature power spectrum.

analytical and measured power, although the overall reconstruction power (both analytical and measured) is $\sim 5\times$ higher than for the unconstrained NILC. As the tSZ clusters are highly non-Gaussian and also correlated with the temperature, this is consistent with the offset being caused by a term of the form $\langle FGFG\delta\delta\rangle$. It would be of interest to study this contribution on simulations or analytically; such a study is beyond the scope of this paper.

Going forward, all spectra that we show will be with the tSZ clusters masked. All of our results are derived from this case.

We defer to future work a more careful analysis of these the auto power spectra of v^{kSZ} , although we show results where we include the datapoints in our Gaussian likelihood in Section 6.4.

6.2 Cross power spectra of the kSZ and continuity-equation velocity

6.2.1 Measurements of $C_L^{v^{kSZ}v^{cont}}$

We show the measured cross-correlation between the kSZ-reconstructed velocity and the continuity-equation-reconstructed velocity, and the best-fit model, in Fig. 12 for the diagonals of the 16-bin case. These are our baseline datapoints. We perform tests for foreground contamination by using different signal maps in Section 7; we find no evidence for foreground contamination in this signal. As the signal-to-noise is spread over 16 redshift bins, it is difficult to assess by eye the signal to noise. To visually demonstrate this, we co-add our datapoints into an estimate of $C_L^{\nu_1\nu_1}$ as in McCarthy et al. (2025). We show this co-added plot in Fig. 13.

We fit two models to the baseline dataset: an N+1-dimensional model where we have one b_{ν} parameter and N galaxy bias parameters, and a 2N-dimensional model where we have N galaxy bias parameters and N velocity bias parameters b_{ν}^{α} . We summarize the constraints, signal-to-noise ratios, and goodness of fit in Table 3, on both SGC and NGC and for their combination. The SNR is calculated as the mean b_{ν} from the one- b_{ν} model divided by its errorbar. We find good fits with acceptable PTEs (note that we neglect the galaxy biases in our degrees of freedom counting, but we also do not count the contribution of the galaxy bias priors to the χ^2) when calculating the PTE. We show the posteriors on b_{ν} for each case in Fig. 15. We prefer the multiple- b_{ν}^{α} model over the single- b_{ν} model with a $\Delta\chi^2$ of 27 for 15 more parameters; this has a PTE 0.04%, and indicates a $\sim 2\sigma$ preference for the several- b_{ν}^{α} model.

The individually recovered b_v^{α} are shown in Fig. 16. We compare both models by defining a χ^2 according to

$$\chi^{2} = (b_{\nu}^{\alpha} - b_{\nu}) C_{b\alpha}^{-1} (b_{\nu}^{\alpha} - b_{\nu}) \tag{42}$$

where $C_{b_{\nu}^{\alpha}}$ is the full covariance matrix of the b_{ν}^{α} parameters which we obtain from the MCMC chains. We convert this to a PTE assuming 15 degrees of freedom, and find χ^2 s with slightly low PTEs, similar to the PTE of the $\Delta\chi^2$ between the two model, again demonstrating the 2σ preference for the b_{ν}^{α} model.

6.2.2 L-dependence of the signal and signal-to-noise

We show in Figure 17 the dependence of the overall signal-to-noise on the choice of minimum L in the analysis, for different combinations of the datasets. The statistical significance drops to below 2σ when $L_{\min} \sim 40$. We also show in Figure 18 how the constraint changes when we go to larger L_{\min} , and to smaller number of redshift bins N; in general we find a consistent measurement.

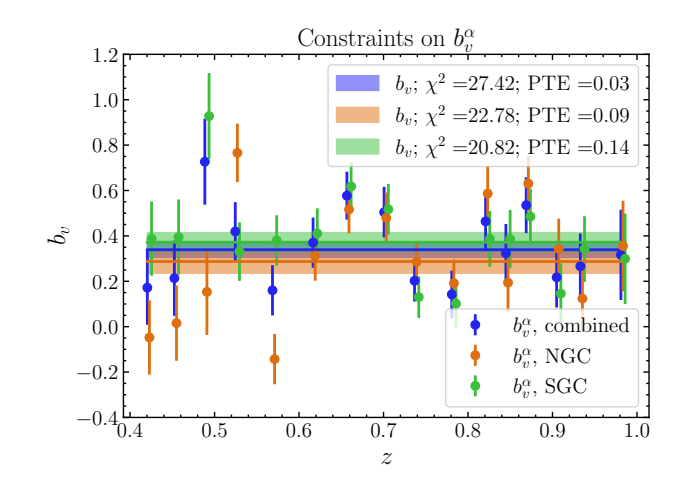


Figure 16. The b_v^α measured in each redshift bin as compared to the one- b_v model where all are constrained to be the same. We compare the separate b_v^α points to the single b_v point and quantify their difference by converting to a χ^2 using the full covariance matrix from the chains. We convert this to a PTE assuming 16-1 degrees of freedom, and find a PTE of 0.03, indicating that the varying b_v^α model is $\sim 2\sigma$ consistent with the single- b_v model.

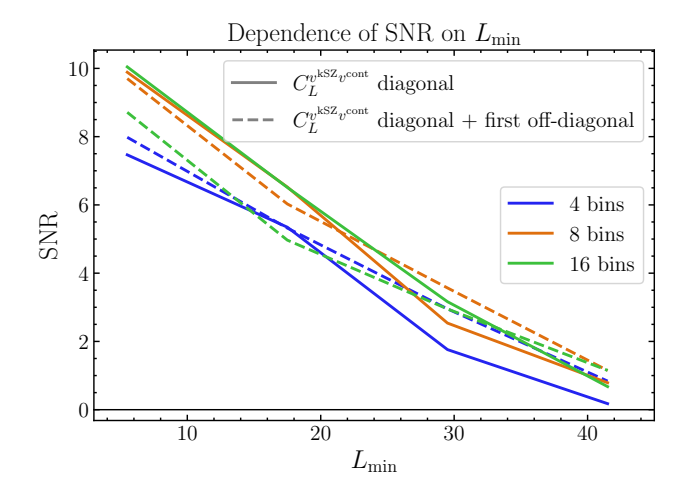


Figure 17. The dependence of the total SNR on the minimum L used in the analysis, for various data combinations. We have used $L_{\rm max}=53$; using a larger $L_{\rm max}$ does not change the results.

6.3 Constraints on scale-dependent bias and non-Gaussianity

For our baseline dataset, we free up the $f_{\rm NL}$ parameter using the model described in Section 4.3.2. Note that this part of the analysis assumes that the transfer function for the $f_{\rm NL}$ response is the same as for the standard velocity. In future work, we will test and refine this assumption using simulations including non-Gaussianity. We show our $f_{\rm NL}$ posteriors in Fig. 19.

We note that in this case the b_{ν}^{α} and b_{ν} models—where the velocity bias is varied independently in each redshift bin and where it is fixed to be equal—are conceptually different models, as the b_{ν} model allows for all of the signal to simultaneously approach 0, where the constraining power on $f_{\rm NL}$ is 0. In contrast, the b_{ν}^{α} model breaks this coupling of the parameters, as the amplitudes are no longer intercorrelated. We illustrate this by showing both models in the corner plot in Fig. 20, where the degeneracy-breaking can be clearly seen.

spec	constraint (combined)	SNR	$N_{ m points}$	$\chi^2_{\min}(b^{\alpha}_{\nu})$	PTE (b_v^α)	$\chi^2_{\min}(b_v)$	PTE (b_v)
$C_L^{v^{ ext{KSZ}}v^{ ext{cont}}}$ (diagonal) (NGC)	0.287 ± 0.052	5.53	64	55.49	0.21	78.45	0.09
$C_L^{v ext{kSZ}_v ext{cont}}$ (diagonal) (SGC) $C_L^{v ext{kSZ}_v ext{cont}}$ (diagonal) (joint)	0.372 ± 0.042	8.78	64	55.6	0.21	76.38	0.12
$C_L^{v^{\text{kSZ}}v^{\text{cont}}}$ (diagonal) (joint)	0.339 ± 0.034	10.04	128	129.25	0.13	156.34	0.04

Table 3. The constraints and goodness-of-fit for the baseline NGC, SGC, and combined case. We use 16 redshift bins and only use the diagonals $C_L^{\nu^{\alpha}\nu^{\beta}}$ for $\alpha = \beta$. For the b_{ν}^{α} model, where the velocity biases are constrained independently in each redshift bin, we find very good and consistent fits in SGC and NGC and so we combine them, and also find a good joint fit. The single-parameter model is a slightly worse fit in all cases.

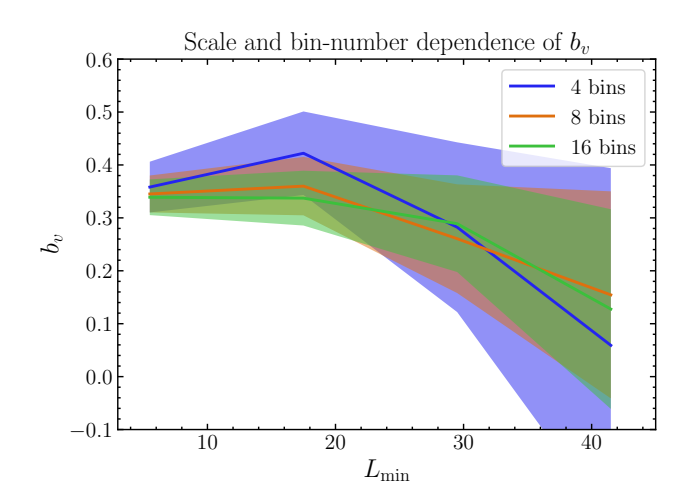


Figure 18. Dependence of the constraint on the minimum L included and number of bins. In general, we see a consistent inference on b_v across scales and number of bins, with most of the SNR coming from large scales. The shaded regions indicate the 1σ uncertainty.

The full corner plot is shown in Appendix G. The marginalized $f_{\rm NL}$ constraints are isolated in Fig. 19.

This behaviour is due to the fact that the non-linearity of the model results in the sensitivity of a given redshift bin to $f_{\rm NL}$ depending on the inferred b_{ν}^{α} . We discuss this further in Appendix G. This is not a fundamental problem of the analysis: in a higher signal-to-noise-ratio, b_{ν} (or b_{ν}^{α}) will be measured by the smaller-scale measurement and this degeneracy will be broken.

We show the constraints on $f_{\rm NL}$ in Fig. 19. For these purposes, we have used priors on b_{ν} and b_{ν}^{α} that allow them to be negative, but we have checked that imposing positivity priors does not significantly affect the $f_{\rm NL}$ posteriors. We use the constraint obtained from the b_{ν}^{α} model as our baseline result: we find $f_{\rm NL} = -180^{+61}_{-86}$ at 67% confidence, with $f_{\rm NL}$ consistent with zero at 2σ .

The introduction of many poorly measured parameters has the risk of introducing spurious prior volume effects, and so we have performed some parameter-recovery tests of our pipeline. In particular, on the replacement of our datavector with a theory vector with $f_{\rm NL}=0$ and $b_{\nu}=b_{\nu}^{\alpha}=0.3$, we found that for the b_{ν} model our posteriors for NGC, SGC, and the joint case are all consistent with the truth; however, for the b_{ν}^{α} this is only the case for the joint NGC+SGC case, with the NGC-alone case showing a significant negative bias (as we see in the data). However, in we use the joint case which as our baseline result, we believe that these prior volume effects are mitigated, as in this case b_{ν}^{α} is well-enough constrained in this case.

The scales used in this analysis are indicated in Fig. 21. Note that we have used the simple Limber conversion to convert from L, χ to

k; on the large scales we use we go beyond Limber and so this is not accurate, but gives a guideline. We defer an in-depth study of the scales from which we get information to future work. However, in this simple comparison, it is possible that our L_{\min} prevents us from reaching the extremely large scales used in Hotinli et al. (2025), and is a possible explanation for why we get less tight constraints than that work on f_{NL} with a similar signal to noise.

6.4 Inclusion of the auto power spectrum

The dominant contribution to the auto power spectra is the $N_L^{(0)}$ bias. We have an analytic expectation for this, which is broadly in line with what we see at high-L in the data, but a careful analysis would require a full realisation-dependent $N_L^{(0)}$ subtraction (Namikawa et al. 2013), as is often done in CMB lensing power spectrum analyses (Planck Collaboration 2020b; Qu et al. 2024). We defer this to future work, but for now we note that if we model $N_L^{(0)}$ as scale-independent we can include the auto-points in our likelihood with the following model:

$$C_{\alpha}^{\nu kSZ} v_{\alpha}^{kSZ} = (b_{\nu}^{\alpha})^2 C_{L}^{\nu \alpha \nu \alpha} + a^{\alpha} N_{L}^{(0), \alpha}, \tag{43}$$

where a^{α} is a scale-independent correction to the noise that we fit and $C_L^{\nu\alpha\nu\alpha}$ is the ΛCDM theory prediction. The model is fit separately in each redshift bin, and in NGC and SGC (with a^{α} different in NGC and SGC).

For the purposes of assessing detection significance, we first constrain an amplitude parameter, $(b_{\nu}^{\alpha})^2$, using a prior that is linear in $(b_{\nu}^{\alpha})^2$ and allows it to be negative. When we do this, we see a hint of a signal (at 2.1σ) in the auto alone, with $b_{\nu}^2 = 0.089 \pm 0.042$, which we show on the left hand side of Figure 22.

We also use this to place a constraint on b_{ν} , with a linear prior on b_{ν} and imposing $b_{\nu} > 0$; we find $0.25 < b_{\nu} < 0.37$ at 67% confidence. We get a good fit in the auto-alone case, with a best-fit χ^2 of 127 for 192 datapoints and 33 parameters (one b_{ν} parameter and $16 \times 2~a^{\alpha}$ parameters), corresponding to a PTE of 97%. Previous work (Bloch & Johnson 2024) constrained the model above using Planck and unWISE data; note that the numerical bounds on b_{ν} from that work cannot be directly compared to the results here due to different choices of $C_{\ell}^{g\tau}$ model (see discussion in Section 4.1.2).

The auto-alone case is consistent with the cross-only constraint and so we can combine them; this gives $b_{\nu} = 0.33 \pm 0.03$ (where we again we use a linear prior in b_{ν} as the cross spectra are sufficiently constraining), increasing our signal-to-noise ratio to 11. These are summarized in Fig. 22. The PTE for the combination is 0.04 (with a best-fit of χ^2 245.1 for 256 datapoints and 48 parameters). We show the recovered noise amplitude factors in Fig. 23.

Note that in our covariance matrix we assume that $a^{\alpha} = 1$ everywhere. As the combined as are closer to $a^{\alpha} = 1.06$ on SGC and $a^{\alpha} = 1.1$ on NGC. As our SNR is dominated by SGC, and the error-

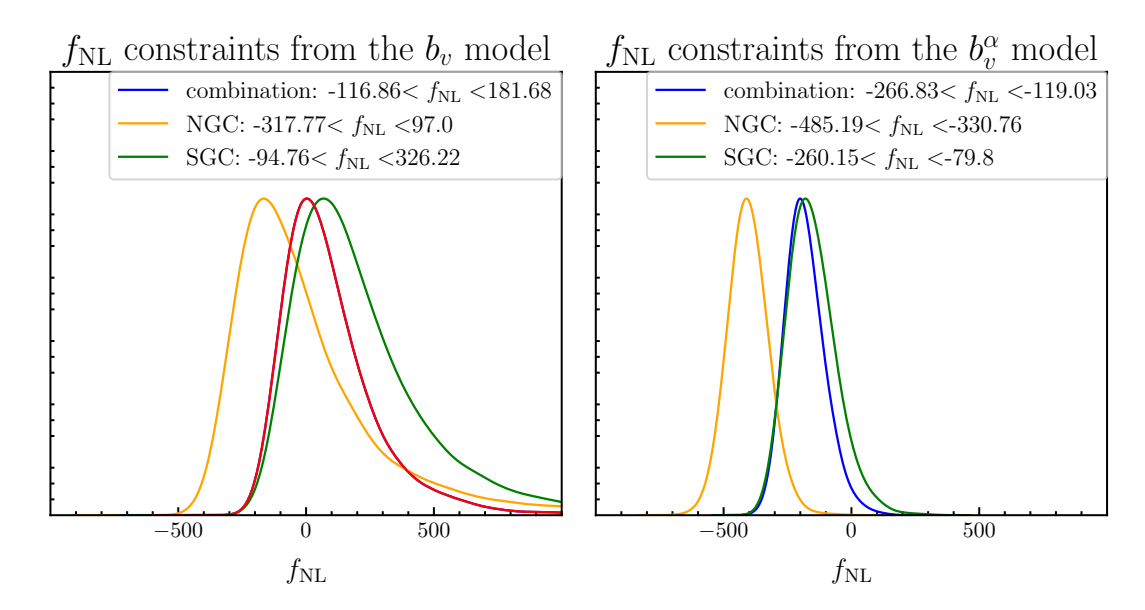


Figure 19. Constraints on f_{NL} , from the b_v^{α} model (left) and the b_v model (right). The constraints quoted in the legend are 67% confidence intervals. See the text for a discussion of the low "NGC" posterior on the RHS.

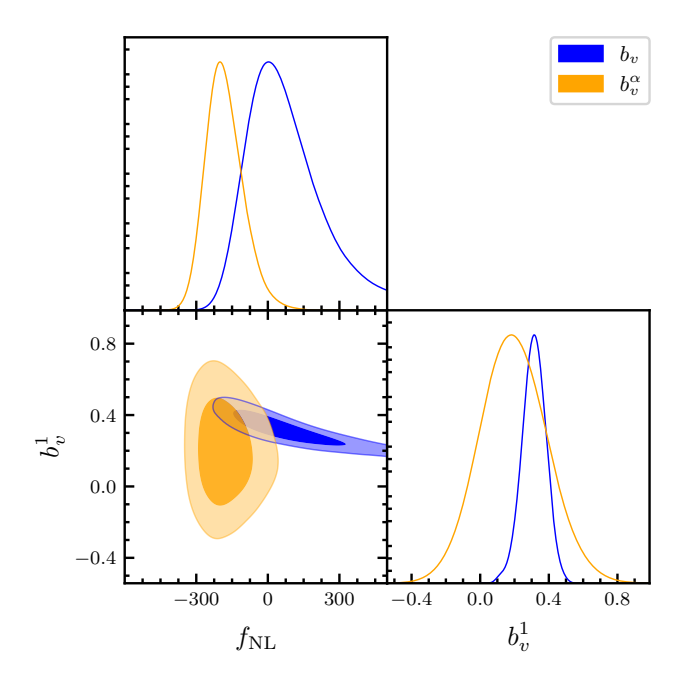


Figure 20. Constraints on $f_{\rm NL}$ and the b_{ν}^{α} models, for the case where the velocity bias is varied independently in each redshift bin (orange contours) as well as when it is fixed in each redshift bin (blue contours). We show only a subset of the full corner plot, as it is all that is necessary for illustration purposes. The degeneracy with $f_{\rm NL}$ is clearly broken in the b_{ν}^{α} case. We show the full corner plot in Appendix. G.

bars on the cross-spectrum are proportional to the square root of this number, we expect the effect on our reported SNR to be minor.

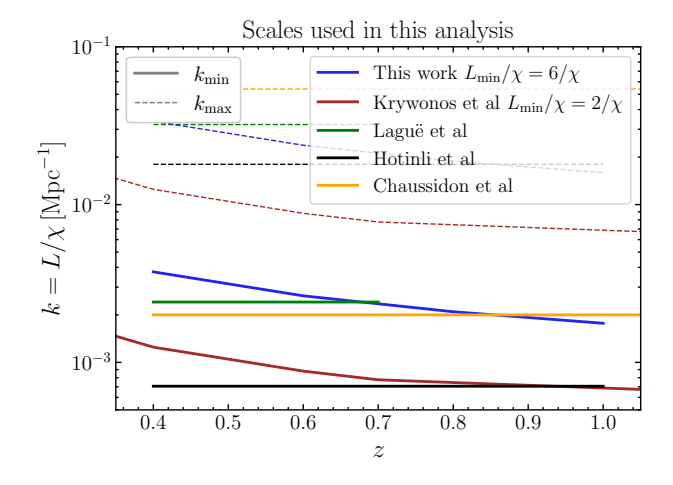


Figure 21. Scales used in this analysis. We show an approximate k-scale calculated by L/χ , and we indicate the scale cuts used by other relevant recent works for comparison—in particular, of three works which have constrained $f_{\rm NL}$ with the kSZ velocity cross-correlation (Krywonos et al. 2024; Laguë et al. 2024; Hotinli et al. 2025), and of the three-dimensional $f_{\rm NL}$ of the same galaxy sample (Chaussidon et al. 2025).

7 TESTS FOR FOREGROUND CONTAMINATION

On small scales, the millimeter sky (on which we measure the CMB) is dominated by non-kSZ foregrounds, such as the tSZ effect and the CIB. These are correlated with large scale structure. In this section we explore whether our datapoints are contaminated by a foreground bias. We do this by exploring the dependence of the datapoints on the choice of CMB+kSZ map: we compare the standard minimum-variance (MV) NILC map with a map with the tSZ explicitly removed by y-deprojection. Note that this map will have no tSZ foregrounds but a different amount of any other foregrounds; thus we don't use it as a "foreground-cleaned" map but instead as a "differently-cleaned" map. A foreground-immune signal will be consistent when measured

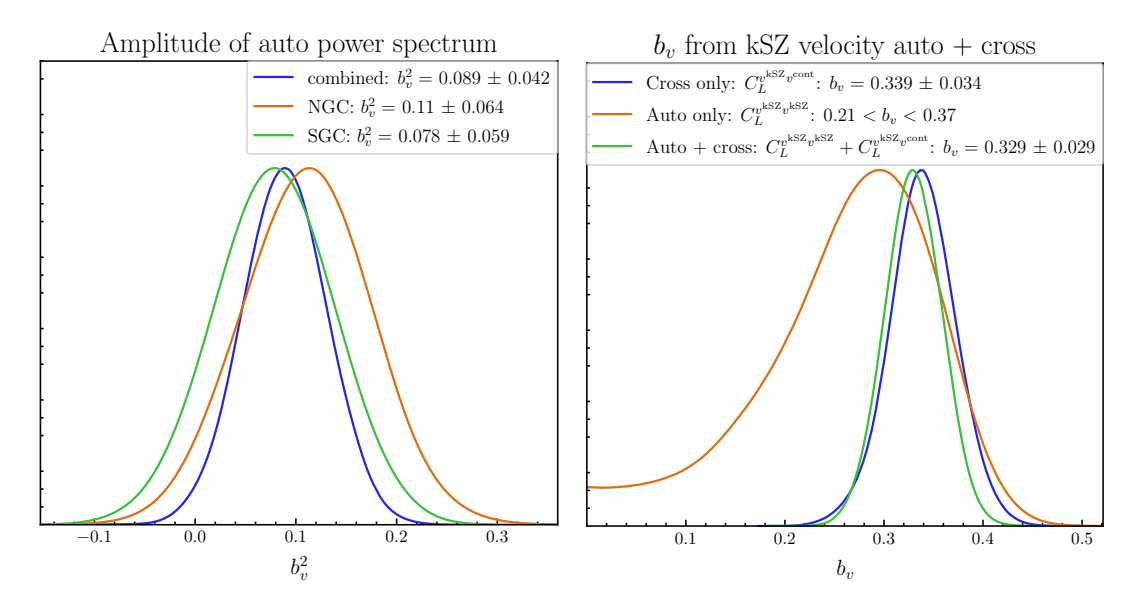


Figure 22. Left: The constraints on the amplitude of the kSZ velocity auto power spectrum, b_v^2 . We measure this at 2.1σ to be $b_v^2 = 0.089 \pm 0.042$. Right: The constraints on b_v from the kSZ velocity auto power spectrum, its cross with the continuity-equation velocity, and their combination. Note that on the left hand side the prior is linear in the amplitude of the signal b_v^2 (for the purposes of assessing detection significance), while on the right hand side we impose a physical prior $b_v > 0$ which is linear in b_v . We measure the auto power spectrum at 2σ significance. It is consistent with the cross power-spectrum, and the combined constraint is significant at 11σ .

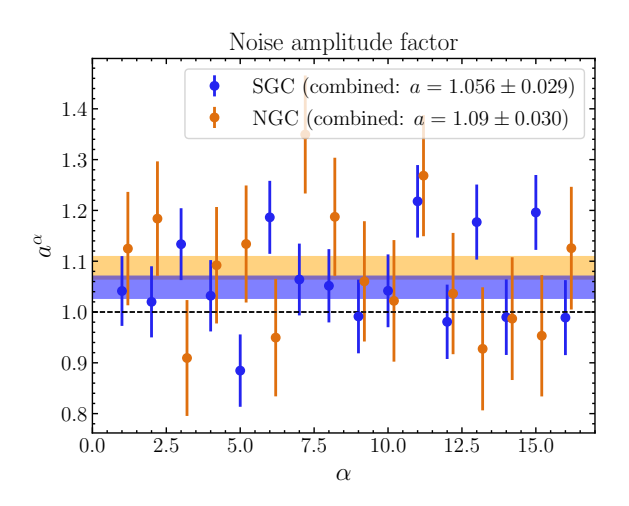


Figure 23. The recovered noise amplitudes when the auto power spectrum is fit to a constant noise model. These are multiplicative amplitudes with respect to the analytical noise prediction.

with each map. We also use a foreground-only map (a blackbody-deprojected *y* map) as a "foreground-only" map on which we expect a null result.

In addition to performing contamination tests of our signal, we perform similar tests on an alternative signal - $C_L^{\nu^{\rm kSZ}g}$, the cross-correlation measured between the kSZ-estimated velocity and the galaxies themselves, as was measured in Lai et al. (2025).

galaxies themselves, as was measured in Lai et al. (2025). The velocity-velocity correlation $C_L^{\nu_\alpha\nu_\beta}$ concentrates most of the signal-to-noise in the equal-redshift diagonal ($\alpha=\beta$). In contrast, due to the non-local nature of the v-g correlation, the velocity-galaxy correlation $C_L^{\nu_\alpha g_\beta}$ concentrates most of the signal-to-noise in the off-diagonals ($\alpha\neq\beta$) (see Section 4.2.7 for a discussion), and

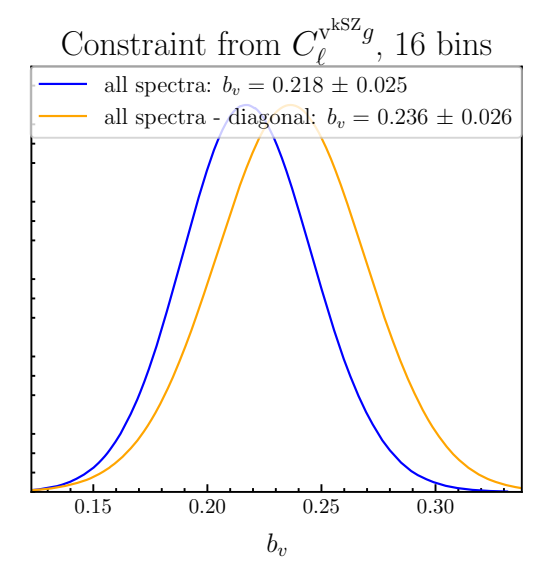


Figure 24. The shift in the b_v measurement from $C_v^{VKSZ}_g$ when the diagonals are dropped. This is an inconsistent shift (at the 2.2σ level) for a nested dataset, as quantified by the test derived in Gratton & Challinor (2020).

very little on the diagonal; however, in practice we measure a large signal on the diagonal.

We show a subset of the $C_L^{v_\alpha^{kSZ}g_\beta}$ datapoints in Fig. 25. Even by inspection by eye, we notice a large excess on the $\alpha=\beta$ diagonals of $C_L^{v^{kSZ}g}$ (where the signal is expected to be close to zero), on almost all scales. This is *not* present in $C_L^{v^{kSZ}v^{cont}}$. After performing tests with differently cleaned maps, we attribute this to foreground contamination of the form $\langle FG^S\delta^S\delta^L \rangle$, where FG^S indicates a small-scale foreground in the CMB+kSZ map. We note that contamination with

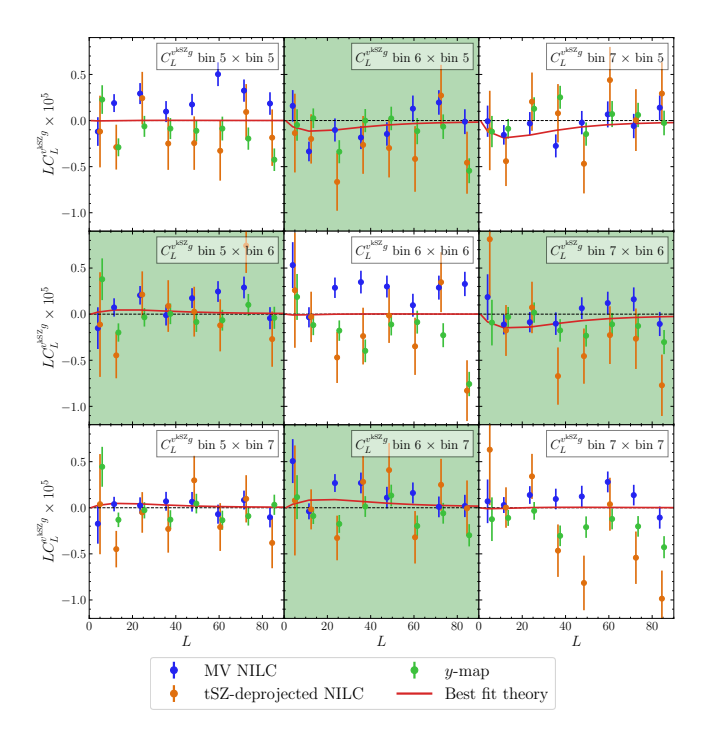


Figure 25. The data points measured from reconstruction performed on an MV NILC (blue) versus an SZ-deprojected NILC (orange), for a subset of $C_L^{v,kSZ}{}^g$. We have co-added the SGC and NGC datapoints. A general observation is that these sets of points appear consistent except for a possible bias on the diagonal of $C_L^{v,kSZ}{}^g$. We also show the points measured with a *foreground-only* map ("y-map", in green). In general these are consistent with null on the off-diagonals, but not on the diagonal. Note that we have highlighted the first off-diagonal (where most of the signal-to-noise is concentrated) in green to guide the eye. As argued in the text, this is evidence for foreground bias on the diagonals of the $C_L^{v,kSZ}{}^g$ measurement.

this behaviour – affecting $C_L^{v^{\rm kSZ}g}$ but not $C_L^{v^{\rm kSZ}_{V^{\rm cont}}}$ at equal redshifts – would arise if foreground contamination to the kSZ velocity reconstruction depended directly on the large-scale density field (this could result from a small-scale non-Gaussian CMB foreground coupling with the small-scale galaxies within the quadratic estimator). Contamination of this form would not correlate with the continuity-equation velocity on the equal-redshift bins due to the suppressed density-velocity signal at equal redshift.

We perform some tests of the signal in order to check this hypothesis. In particular, we show a subset of $C_L^{\nu^{\rm kSZ} g}$ in Fig. 25 and a subset of $C_L^{\nu^{\rm kSZ} \nu^{\rm cont}}$ in Fig. 26, including the some off-diagonals, when we use the MV NILC and the SZ-deprojected NILC; we also show some foreground-only (null-signal) points, where the reconstruction was performed with the y-map replacing the temperature map. For the y-map case, we use the same filters in the velocity reconstruction as for the MV map, but for the SZ-deprojected map we replace the C_L^{TT} filter with the measured power of the SZ-deprojected map. Thus, the measured power spectrum of the SZ-deprojected map is well aproximated by the analytical $N_L^{(0)}$ calculated with the new filters, but the y-map signal is not, due to a mismatch in estimated and true power. We rescale the outputs by a constant factor such that the observed power matches the analytical $N_L^{(0)}$. 15

For the MV NILC map and the SZ-deprojected map, we calculate

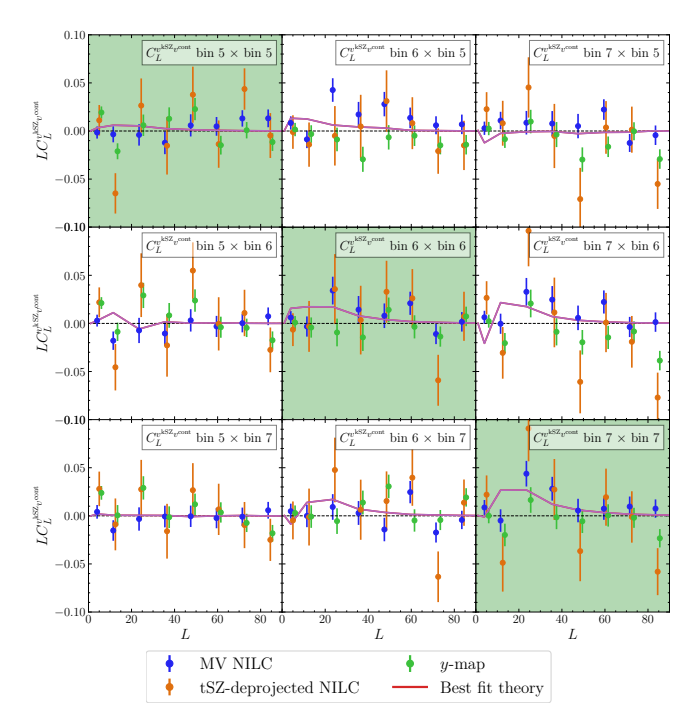


Figure 26. The NGC data points measured from reconstruction performed on an MV NILC (blue) versus an SZ-deprojected NILC (orange), for a subset of $C_L^{\nu kSZ_{\nu} \text{cont}}$. A general observation is that these sets of points appear consistent with each other. We also show the points measured with a *foreground-only* map ("y-map", in green). In general these are consistent with null. Note that we have highlighted the diagonal (where most of the signal-to-noise is concentrated) in green to guide the eye. This is consistent with no contribution from foreground bias on the diagonals of the $C_L^{\nu kSZ_{\nu} \text{cont}}$ measurement, which we use as our baseline dataset.

the covariance as we do for the main analysis. We use the mask-decoupled theoretical covariance matrix assuming the appropriate analytical estimate of $N_L^{(0)}$ for the auto power spectra of the kSZ reconstructions, and the measured power for the auto power spectra of the large-scale galaxies or continuity-equation velocity. For the y-map case, we use the $N_L^{(0)}$ of the MV-reconstruction case, remembering that we have rescaled the outputs such that their power matches this.

In general, it is hard to make strict conclusions by eye as the SZ-deprojected points are noisier. However, there is clear evidence for a systematic inconsistency between the MV NILC and SZ-deprojected NILC points on the diagonal of $C_L^{\nu \text{KSZ}_g}$ and not elsewhere. Additionally, the "y-map" points are not null here but are null elsewhere.

To quantify this and further test for foreground contamination, we explore constraints on an overall velocity bias parameter in different regimes in Appendix E. Here, we simply show the biggest shifts in the constraints: the final constraints from $C_\ell^{\nu^{kSZ}g}$ shift by $\sim 1\sigma$ when the diagonal is dropped, as is shown in Figure 24. Gratton & Challinor (2020) devised a useful test to check whether the shift in a parameter when analyzed with a subset of a larger dataset as compared to the full dataset is within the expected fluctuation range: in particular, we expect fluctuations of order $\sigma_\Delta^2 \sim \sigma_a^2 - \sigma_b^2$. By this metric, there is a significant shift in the inferred b_ν when going from

to match the observed power spectra of the y-map and use the analytical $N_L^{(0)}$ in the covariance calculation. Conclusions are qualitatively similar.

¹⁵ We have also performed this test for the case where we recalculate the filters

the full dataset to one with no diagonal; the shift is a 2.2σ anomaly. Given this information and our knowledge of the shifts or consistency in datapoints and b_{ν} inference for differently-cleaned maps and our tests with foreground-only maps, we conclude that at the current level of sensitivity the diagonal of $C_L^{\nu g}$ is foreground-dominated.

We propose reducing the foreground contribution to C_L^{vg} by forming the estimator $C_L^{v_\alpha g_\beta} - C_L^{v_\beta g_\alpha}$, which could be more immune to foreground bias. We will explore this in future work.

8 CONCLUSION

We have measured the velocity field with the small-scale kSZ signal in ACT through its anisotropic cross-correlation with the DESI LRG galaxy sample. We have measured a 10σ cross-correlation signal with an alternative velocity field estimate from the continuity equation, and found a good fit to the data for our model. We find a low velocity bias with respect to our theory, which was created to match the Illustris-TNG simulations and a HOD prescription, indicating at high significance that this theory is an incomplete model of the true astrophysics. This is consistent with recent work which used a similar data combination to directly constrain this model (Hadzhiyska et al. 2025b), and other recent works which constrained a slightly different model (Lai et al. 2025; Hotinli et al. 2025).

We perform several consistency tests of our measurement, including making a measurement with randomly shuffled galaxies and confirming consistency with zero; and various frequency-dependent tests. We see no evidence for frequency-dependent foregrounds in our $C_L^{\nu^{\rm kSZ}\nu^{\rm cont}}$ statistic. This stands in contrast to what we see in a $C_L^{\nu^{\rm kSZ}g}$ measurement that we perform for comparison, where we find evidence for some contamination on the equal-redshift spectra. However, we note that these spectra contribute only a very small amount to the signal-to-noise that only contribute a small amount to the total signal-to-noise.

The signal that we measure is sensitive to scale-dependent bias, and so we constrain the local primordial non-Gaussianity parameter $f_{\rm NL}$ to be $f_{\rm NL} = -180^{+61}_{-86}$ at 67% confidence, and consistent with zero at 2σ . Constraints on primordial non-Gaussianity are a main goal of the kSZ velocity reconstruction programme, and it would be of interest to compare the information in the 2-dimensional reconstruction performed here to that in a recent complementary 3-dimensional reconstruction Hotinli et al. (2025), which found similar signal-tonoise on a smaller sky area and yet significantly tighter constraints on $f_{\rm NL}$. We have suggested that this may be due to our probing of different maximum scales in our analysis. An analytic study of the scales most important for $f_{\rm NL}$ constraints would be of interest but beyond the scope of this paper.

There are several ways in which our analysis was suboptimal, and it would be of interest to improve it. First, by performing a quadratic-maximum-likelihood analysis following Lai et al. (2025); Kvasiuk et al. (2025); second, by more optimal weighting of the galaxies by their redshift error following Hotinli et al. (2025).

We additionally found a 2.1σ hint of the auto power spectrum signal in $C_L^{\gamma \text{KSZ}_{\gamma}\text{KSZ}}$, and it would be of interest to follow up on this with a more robust analysis. We note that foreground biases to this statistic may be a problem, which we have shown can be somewhat mitigated by removal of tSZ clusters but it would be well-motivated to investigate this further.

A key aspect of this paper is our demonstration of our pipeline on *N*-body simulations. The continuity-equation velocity reconstruction process required this for our theoretical model; in this respect, the

 $C_L^{\nu \rm kSZ} g$ signal, which can be modelled cleanly through analytic calculations, is much more attractive than $C_L^{\nu \rm kSZ} \nu^{\rm cont}$. The kSZ era of CMB measurements continues to develop, and it will be imperative to understand better and control systematics such as the foreground biases investigated here in future analyses. Detailed studies for experiment-specific setups will be of high interest for current and upcoming surveys.

ACKNOWLEDGEMENTS

We thank Edmond Chaussidon, Simone Ferraro, Selim Hotinli, and Kendrick Smith for useful discussions. Support for ACT was through the U.S. National Science Foundation through awards AST-0408698, AST-0965625, and AST-1440226 for the ACT project, as well as awards PHY-0355328, PHY-0855887 and PHY-1214379. Funding was also provided by Princeton University, the University of Pennsylvania, and a Canada Foundation for Innovation (CFI) award to UBC. ACT operated in the Parque Astronómico Atacama in northern Chile under the auspices of the Agencia Nacional de Investigación y Desarrollo (ANID). The development of multichroic detectors and lenses was supported by NASA grants NNX13AE56G and NNX14AB58G. Detector research at NIST was supported by the NIST Innovations in Measurement Science program, Computing for ACT was performed using the Princeton Research Computing resources at Princeton University, the National Energy Research Scientific Computing Center (NERSC), and the Niagara supercomputer at the SciNet HPC Consortium. SciNet is funded by the CFI under the auspices of Compute Canada, the Government of Ontario, the Ontario Research Fund-Research Excellence, and the University of Toronto. We thank the Republic of Chile for hosting ACT in the northern Atacama, and the local indigenous Licanantay communities whom we follow in observing and learning from the night sky.

FMcC acknowledges support from the European Research Council (ERC) under the European Union's Horizon 2020 research and innovation programme (Grant agreement No. 851274). The Flatiron Institute is a division of the Simons Foundation.

This work made use of python, numpy¹⁶ (Harris et al. 2020), matplotlib¹⁷ (Hunter 2007), scipy¹⁸ (Virtanen et al. 2020), astropy¹⁹ (Astropy Collaboration et al. 2013, 2018, 2022), HEALPix (Górski et al. 2005) and its python implementation healpy²⁰ (Zonca et al. 2019), pixell²¹, pymaster²² (Alonso et al. 2019), CAMB²³ (Lewis et al. 2000), class²⁴ (Lesgourgues 2011; Blas et al. 2011), Cobaya²⁵ (Torrado & Lewis 2019, 2021), and getDist²⁶ (Lewis 2019).

```
16 https://numpy.org
17 https://matplotlib.org
18 https://scipy.org
19 https://www.astropy.org/index.html
20 https://healpy.readthedocs.io/en/latest/
21 https://pixell.readthedocs.io/en/latest/
22 https://namaster.readthedocs.io/en/latest/
23 https://camb.info
24 http://class-code.net
25 https://cobaya.readthedocs.io
26 https://getdist.readthedocs.io/en/latest/
```

REFERENCES

- Abitbol, M., et al. 2025, arXiv:2503.00636, J. Cosmology Astropart. Phys., 2025, 034, The Simons Observatory: science goals and forecasts for the enhanced Large Aperture Telescope
- ACTDESHSC Collaboration, et al. 2025, arXiv:2507.21459, arXiv e-prints, arXiv:2507.21459, The Atacama Cosmology Telescope: DR6 Sunyaev-Zel'dovich Selected Galaxy Clusters Catalog
- Ade, P., et al. 2019, arXiv:1808.07445, J. Cosmology Astropart. Phys., 2019, 056, The Simons Observatory: science goals and forecasts
- Alonso, D., Sanchez, J., Slosar, A., & LSST Dark Energy Science Collaboration. 2019, MNRAS, 484, 4127, A unified pseudo- C_{ℓ} framework
- Astropy Collaboration, et al. 2013, arXiv:1307.6212, A&A, 558, A33, Astropy: A community Python package for astronomy
- —. 2018, arXiv:1801.02634, AJ, 156, 123, The Astropy Project: Building an Open-science Project and Status of the v2.0 Core Package
- —. 2022, arXiv:2206.14220, ApJ, 935, 167, The Astropy Project: Sustaining and Growing a Community-oriented Open-source Project and the Latest Major Release (v5.0) of the Core Package
- Barreira, A. 2022, arXiv:2205.05673, J. Cosmology Astropart. Phys., 2022, 013, Can we actually constrain f_{NL} using the scale-dependent bias effect? An illustration of the impact of galaxy bias uncertainties using the BOSS DR12 galaxy power spectrum
- Bennett, C. L., et al. 1992, ApJ, 396, L7, Preliminary Separation of Galactic and Cosmic Microwave Emission for the COBE Differential Microwave Radiometers
- Bermejo-Climent, J. R., et al. 2025, arXiv:2412.10279, A&A, 698, A177, Constraints on primordial non-Gaussianity from the cross-correlation of DESI luminous red galaxies and Planck CMB lensing
- Blas, D., Lesgourgues, J., & Tram, T. 2011, arXiv:1104.2933, J. Cosmology Astropart. Phys., 2011, 034, The Cosmic Linear Anisotropy Solving System (CLASS). Part II: Approximation schemes
- Bloch, R. & Johnson, M. C. 2024, arXiv:2405.00809, arXiv e-prints, arXiv:2405.00809, Kinetic Sunyaev Zel'dovich velocity reconstruction from Planck and unWISE
- Calafut, V., et al. 2021, arXiv:2101.08374, Phys. Rev. D, 104, 043502, The Atacama Cosmology Telescope: Detection of the pairwise kinematic Sunyaev-Zel'dovich effect with SDSS DR15 galaxies
- Carron, J., Mirmelstein, M., & Lewis, A. 2022, arXiv:2206.07773, J. Cosmology Astropart. Phys., 2022, 039, CMB lensing from Planck PR4 maps
- Cartis, C., Fiala, J., Marteau, B., & Roberts, L. 2018a, arXiv:1804.00154, arXiv e-prints, arXiv:1804.00154, Improving the Flexibility and Robustness of Model-Based Derivative-Free Optimization Solvers
- Cartis, C., Roberts, L., & Sheridan-Methyen, O. 2018b, arXiv:1812.11343, arXiv e-prints, arXiv:1812.11343, Escaping local minima with derivative-free methods: a numerical investigation
- Cayuso, J., Bloch, R., Hotinli, S. C., Johnson, M. C., & McCarthy, F. 2023, arXiv:2111.11526, J. Cosmology Astropart. Phys., 2023, 051, Velocity reconstruction with the cosmic microwave background and galaxy surveys
- Chaussidon, E., et al. 2025, arXiv:2411.17623, J. Cosmology Astropart. Phys., 2025, 029, Constraining primordial non-Gaussianity with DESI 2024 LRG and QSO samples
- Chen, X. & Wright, E. L. 2009, arXiv:0809.4025, ApJ, 694, 222, Extragalactic Point Source Search in Five-Year WMAP 41, 61, and 94 Ghz Maps
- Contreras, D., Johnson, M. C., & Mertens, J. B. 2019, arXiv:1904.10033, J. Cosmology Astropart. Phys., 2019, 024, Towards detection of relativistic effects in galaxy number counts using kSZ tomography
- Cooray, A. & Sheth, R. 2002, astro-ph/0206508, Phys. Rep., 372, 1, Halo models of large scale structure
- Coulton, W., et al. 2024a, arXiv:2307.01258, Phys. Rev. D, 109, 063530, Atacama Cosmology Telescope: High-resolution component-separated maps across one third of the sky
- Coulton, W. R., et al. 2024b, arXiv:2401.13033, arXiv e-prints, arXiv:2401.13033, The Atacama Cosmology Telescope: A search for late-time anisotropic screening of the Cosmic Microwave Background Dalal, N., Doré, O., Huterer, D., & Shirokov, A. 2008, arXiv:0710.4560,

- Phys. Rev. D, 77, 123514, Imprints of primordial non-Gaussianities on large-scale structure: Scale-dependent bias and abundance of virialized objects
- de Putter, R., Gleyzes, J., & Doré, O. 2017, arXiv:1612.05248, Phys. Rev. D, 95, 123507, Next non-Gaussianity frontier: What can a measurement with σ (f_{NL}) \lesssim 1 tell us about multifield inflation?
- Delabrouille, J., Cardoso, J. F., Le Jeune, M., Betoule, M., Fay, G., & Guilloux, F. 2009, arXiv:0807.0773, A&A, 493, 835, A full sky, low foreground, high resolution CMB map from WMAP
- Deutsch, A.-S., Dimastrogiovanni, E., Johnson, M. C., Münchmeyer, M., & Terrana, A. 2018, arXiv:1707.08129, Phys. Rev. D, 98, 123501, Reconstruction of the remote dipole and quadrupole fields from the kinetic Sunyaev Zel'dovich and polarized Sunyaev Zel'dovich effects
- Dey, A., et al. 2019, arXiv:1804.08657, AJ, 157, 168, Overview of the DESI Legacy Imaging Surveys
- Eisenstein, D. J., Seo, H.-J., Sirko, E., & Spergel, D. N. 2007, astro-ph/0604362, ApJ, 664, 675, Improving Cosmological Distance Measurements by Reconstruction of the Baryon Acoustic Peak
- Fabbian, G., Alonso, D., Storey-Fisher, K., & Cornish, T. 2025, arXiv:2504.20992, arXiv e-prints, arXiv:2504.20992, Constraints on primordial non-Gaussianity from Quaia
- Fang, X., Krause, E., Eifler, T., & MacCrann, N. 2020, arXiv:1911.11947, J. Cosmology Astropart. Phys., 2020, 010, Beyond Limber: efficient computation of angular power spectra for galaxy clustering and weak lensing
- Garrison, L. H., Eisenstein, D. J., Ferrer, D., Maksimova, N. A., & Pinto, P. A. 2021, arXiv:2110.11392, MNRAS, 508, 575, The ABACUS cosmological N-body code
- Giannantonio, T. & Percival, W. J. 2014, arXiv:1312.5154, MNRAS, 441, L16, Using correlations between cosmic microwave background lensing and large-scale structure to measure primordial non-Gaussianity.
- Giri, U. & Smith, K. M. 2022, arXiv:2010.07193, J. Cosmology Astropart. Phys., 2022, 028, Exploring KSZ velocity reconstruction with N-body simulations and the halo model
- Górski, K. M., Hivon, E., Banday, A. J., Wandelt, B. D., Hansen, F. K., Reinecke, M., & Bartelmann, M. 2005, astro-ph/0409513, ApJ, 622, 759, HEALPix: A Framework for High-Resolution Discretization and Fast Analysis of Data Distributed on the Sphere
- Gratton, S. & Challinor, A. 2020, arXiv:1911.07754, MNRAS, 499, 3410, Understanding parameter differences between analyses employing nested data subsets
- Guachalla, B. R., et al. 2025, arXiv:2503.19870, Phys. Rev. D, 112, 103512, Backlighting extended gas halos around luminous red galaxies: Kinematic Sunyaev-Zel'dovich effect from DESI Y1 and ACT data
- Hadzhiyska, B., Ferraro, S., Ried Guachalla, B., & Schaan, E. 2024, arXiv:2312.12434, Phys. Rev. D, 109, 103534, Velocity reconstruction in the era of DESI and Rubin/LSST. II. Realistic samples on the light cone
- Hadzhiyska, B., Garrison, L. H., Eisenstein, D., & Bose, S. 2022, arXiv:2110.11413, MNRAS, 509, 2194, The halo light-cone catalogues of ABACUSSUMMIT
- Hadzhiyska, B., Sailer, N., & Ferraro, S. 2025a, arXiv:2506.17379, arXiv e-prints, arXiv:2506.17379, Mapping the gas density with the kinematic Sunyaev-Zel'dovich and patchy screening effects: a self-consistent comparison
- Hadzhiyska, B., et al. 2025b, arXiv:2407.07152, Phys. Rev. D, 112, 083509, Evidence for large baryonic feedback at low and intermediate redshifts from kinematic Sunyaev-Zel'dovich observations with ACT and DESI photometric galaxies
- Hand, N., et al. 2012, arXiv:1203.4219, Phys. Rev. Lett., 109, 041101, Evidence of Galaxy Cluster Motions with the Kinematic Sunyaev-Zel'dovich Effect
- Harris, C. R., et al. 2020, Nature, 585, 357, Array programming with NumPy, https://doi.org/10.1038/s41586-020-2649-2
- Hill, J. C., Ferraro, S., Battaglia, N., Liu, J., & Spergel, D. N. 2016, arXiv:1603.01608, Phys. Rev. Lett., 117, 051301, Kinematic Sunyaev-Zel'dovich Effect with Projected Fields: A Novel Probe of the Baryon Distribution with Planck, WMAP, and WISE Data
- Hilton, M., et al. 2021, arXiv:2009.11043, ApJS, 253, 3, The Atacama Cosmology Telescope: A Catalog of >4000 Sunyaev-Zel'dovich Galaxy Clus-

- Hivon, E., Górski, K. M., Netterfield, C. B., Crill, B. P., Prunet, S., & Hansen, F. 2002, ApJ, 567, 2, MASTER of the Cosmic Microwave Background Anisotropy Power Spectrum: A Fast Method for Statistical Analysis of Large and Complex Cosmic Microwave Background Data Sets
- Hotinli, S. C., Smith, K. M., & Ferraro, S. 2025, arXiv:2506.21657, arXiv e-prints, arXiv:2506.21657, Velocity Reconstruction from KSZ: Measuring f_{NL} with ACT and DESILS
- Hunter, J. D. 2007, Computing in Science & Engineering, 9, 90, Matplotlib: A 2D graphics environment
- Kim, J., et al. 2024, arXiv:2407.04606, J. Cosmology Astropart. Phys., 2024, 022, The Atacama Cosmology Telescope DR6 and DESI: structure formation over cosmic time with a measurement of the cross-correlation of CMB lensing and luminous red galaxies
- Krolewski, A., et al. 2024, arXiv:2305.07650, J. Cosmology Astropart. Phys., 2024, 021, Constraining primordial non-Gaussianity from DESI quasar targets and Planck CMB lensing
- Krywonos, J., Hotinli, S. C., & Johnson, M. C. 2024, arXiv:2408.05264, arXiv e-prints, arXiv:2408.05264, Constraints on cosmology beyond ΛCDM with kinetic Sunyaev Zel'dovich velocity reconstruction
- Kusiak, A., Bolliet, B., Ferraro, S., Hill, J. C., & Krolewski, A. 2021, arXiv:2102.01068, Phys. Rev. D, 104, 043518, Constraining the baryon abundance with the kinematic Sunyaev-Zel'dovich effect: Projected-field detection using P1anck, WMAP, and unWISE
- Kvasiuk, Y., Lai, A., Münchmeyer, M., & Smith, K. M. 2025, arXiv:2510.05215, arXiv e-prints, arXiv:2510.05215, QML-FAST - A Fast Code for low-ℓ Tomographic Maximum Likelihood Power Spectrum Estimation
- Laguë, A., Madhavacheril, M. S., Smith, K. M., Ferraro, S., & Schaan, E. 2024, arXiv:2411.08240, Constraints on local primordial non-Gaussianity with 3d Velocity Reconstruction from the Kinetic Sunyaev-Zeldovich Effect
- Laguë, A., Madhavacheril, M. S., Smith, K. M., Ferraro, S., & Schaan, E. 2025, arXiv:2411.08240, Phys. Rev. Lett., 134, 151003, Constraints on Local Primordial Non-Gaussianity with 3D Velocity Reconstruction from the Kinetic Sunyaev-Zeldovich Effect
- Lai, A. C. M., Kvasiuk, Y., & Münchmeyer, M. 2025, arXiv:2506.21684, arXiv e-prints, arXiv:2506.21684, KSZ Velocity Reconstruction with ACT and DESI-LS using a Tomographic QML Power Spectrum Estimator
- Lesgourgues, J. 2011, arXiv:1104.2932, arXiv e-prints, arXiv:1104.2932, The Cosmic Linear Anisotropy Solving System (CLASS) I: Overview
- Lewis, A. 2019, arXiv:1910.13970, GetDist: a Python package for analysing Monte Carlo samples, https://getdist.readthedocs.io
- Lewis, A., Challinor, A., & Lasenby, A. 2000, astro-ph/9911177, ApJ, 538, 473, Efficient Computation of Cosmic Microwave Background Anisotropies in Closed Friedmann-Robertson-Walker Models
- Limber, D. N. 1953, ApJ, 117, 134, The Analysis of Counts of the Extragalactic Nebulae in Terms of a Fluctuating Density Field.
- Liu, R. H., Hadzhiyska, B., Ferraro, S., Bose, S., & Hernández-Aguayo, C. 2025, arXiv:2504.11794, arXiv e-prints, arXiv:2504.11794, Fast Baryonic Field Painting for Sunyaev-Zel'dovich Analyses: Transfer Function vs. Hybrid Effective Field Theory
- Louis, T., et al. 2025, arXiv:2503.14452, arXiv e-prints, arXiv:2503.14452, The Atacama Cosmology Telescope: DR6 Power Spectra, Likelihoods and Λ CDM Parameters
- MacCrann, N., et al. 2024, arXiv:2304.05196, ApJ, 966, 138, The Atacama Cosmology Telescope: Mitigating the Impact of Extragalactic Foregrounds for the DR6 Cosmic Microwave Background Lensing Analysis
- Madhavacheril, M. S., Battaglia, N., Smith, K. M., & Sievers, J. L. 2019, arXiv:1901.02418, Phys. Rev. D, 100, 103532, Cosmology with the kinematic Sunyaev-Zeldovich effect: Breaking the optical depth degeneracy with fast radio bursts
- Madhavacheril, M. S., et al. 2024, arXiv:2304.05203, ApJ, 962, 113, The Atacama Cosmology Telescope: DR6 Gravitational Lensing Map and Cosmological Parameters
- Maksimova, N. A., Garrison, L. H., Eisenstein, D. J., Hadzhiyska, B., Bose, S., & Satterthwaite, T. P. 2021, arXiv:2110.11398, MNRAS, 508, 4017, ABACUSSUMMIT: a massive set of high-accuracy, high-resolution N-

- body simulations
- McCarthy, F. & Johnson, M. C. 2020, arXiv:1907.06678, Phys. Rev. D, 102, 043520, Remote dipole field reconstruction with dusty galaxies
- McCarthy, F., Madhavacheril, M. S., & Maniyar, A. S. 2023, arXiv:2210.01049, Phys. Rev. D, 108, 083522, Constraints on primordial non-Gaussianity from halo bias measured through CMB lensing cross-correlations
- McCarthy, F., et al. 2025, arXiv:2410.06229, J. Cosmology Astropart. Phys., 2025, 057, The Atacama Cosmology Telescope: Large-scale velocity reconstruction with the kinematic Sunyaev-Zel'dovich effect and DESI LRGs
- M.J.D., P. 2009, Technical Report 2009/NA06, DAMTP, University of Cambridge), The BOBYQA algorithm for bound constrained optimization without derivatives
- Münchmeyer, M., Madhavacheril, M. S., Ferraro, S., Johnson, M. C., & Smith, K. M. 2019, arXiv:1810.13424, Phys. Rev. D, 100, 083508, Constraining local non-Gaussianities with kinetic Sunyaev-Zel'dovich tomography
- Naess, S., et al. 2025, arXiv:2503.14451, arXiv e-prints, arXiv:2503.14451, The Atacama Cosmology Telescope: DR6 Maps
- Namikawa, T., Hanson, D., & Takahashi, R. 2013, arXiv:1209.0091, MNRAS, 431, 609, Bias-hardened CMB lensing
- Nelson, D., et al. 2019, arXiv:1812.05609, Computational Astrophysics and Cosmology, 6, 2, The IllustrisTNG simulations: public data release
- Okamoto, T. & Hu, W. 2003, astro-ph/0301031, Phys. Rev. D, 67, 083002, Cosmic microwave background lensing reconstruction on the full sky
- Planck Collaboration. 2013, arXiv:1212.4131, A&A, 557, A52, Planck intermediate results. XI. The gas content of dark matter halos: the Sunyaev-Zeldovich-stellar mass relation for locally brightest galaxies
- —. 2020a, arXiv:1807.06209, A&A, 641, A6, Planck 2018 results. VI. Cosmological parameters
- —. 2020b, arXiv:1807.06210, A&A, 641, A8, Planck 2018 results. VIII. Gravitational lensing
- —. 2020c, arXiv:2007.04997, A&A, 643, A42, Planck intermediate results. LVII. Joint Planck LFI and HFI data processing
- Planck Collaboration, et al. 2020a, arXiv:1807.06205, A&A, 641, A1, Planck 2018 results. I. Overview and the cosmological legacy of Planck
- —. 2020b, arXiv:1905.05697, A&A, 641, A9, Planck 2018 results. IX. Constraints on primordial non-Gaussianity
- Qu, F. J., et al. 2024, arXiv:2304.05202, ApJ, 962, 112, The Atacama Cosmology Telescope: A Measurement of the DR6 CMB Lensing Power Spectrum and Its Implications for Structure Growth
- Remazeilles, M., Delabrouille, J., & Cardoso, J.-F. 2011, arXiv:1006.5599, MNRAS, 410, 2481, CMB and SZ effect separation with constrained Internal Linear Combinations
- Ried Guachalla, B., Schaan, E., Hadzhiyska, B., & Ferraro, S. 2024, arXiv:2312.12435, Phys. Rev. D, 109, 103533, Velocity reconstruction in the era of DESI and Rubin/LSST. I. Exploring spectroscopic, photometric, and hybrid samples
- Roper, F. A., Cai, Y.-C., & Peacock, J. A. 2025, arXiv:2510.12553, arXiv e-prints, arXiv:2510.12553, Mass dependence of halo baryon fractions from the kinetic Sunyaev-Zeldovich effect
- Sailer, N., et al. 2025, arXiv:2407.04607, J. Cosmology Astropart. Phys., 2025, 008, Cosmological constraints from the cross-correlation of DESI Luminous Red Galaxies with CMB lensing from Planck PR4 and ACT DR6
- Schaan, E., et al. 2016, arXiv:1510.06442, Phys. Rev. D, 93, 082002, Evidence for the kinematic Sunyaev-Zel'dovich effect with the Atacama Cosmology Telescope and velocity reconstruction from the Baryon Oscillation Spectroscopic Survey
- —. 2021, arXiv:2009.05557, Phys. Rev. D, 103, 063513, Atacama Cosmology Telescope: Combined kinematic and thermal Sunyaev-Zel'dovich measurements from BOSS CMASS and LOWZ halos
- Schutt, T., Maniyar, A. S., Schaan, E., Coulton, W. R., & Mishra, N. 2024, arXiv:2401.13040, Phys. Rev. D, 109, 103539, New temperature inversion estimator to detect CMB patchy screening by large-scale structure
- Seljak, U. 2009, arXiv:0807.1770, Phys. Rev. Lett., 102, 021302, Extracting Primordial Non-Gaussianity without Cosmic Variance
- Slosar, A., Hirata, C., Seljak, U., Ho, S., & Padmanabhan, N. 2008,

arXiv:0805.3580, J. Cosmology Astropart. Phys., 2008, 031, Constraints on local primordial non-Gaussianity from large scale structure

Smith, K. M., Madhavacheril, M. S., Münchmeyer, M., Ferraro, S., Giri, U., & Johnson, M. C. 2018, arXiv:1810.13423, arXiv e-prints, arXiv:1810.13423, KSZ tomography and the bispectrum

Soergel, B., et al. 2016, arXiv:1603.03904, MNRAS, 461, 3172, Detection of the kinematic Sunyaev-Zel'dovich effect with DES Year 1 and SPT

Stein, G., Alvarez, M. A., Bond, J. R., van Engelen, A., & Battaglia, N. 2020, arXiv:2001.08787, J. Cosmology Astropart. Phys., 2020, 012, The Websky extragalactic CMB simulations

Sunyaev, R. A. & Zeldovich, Y. B. 1970, Ap&SS, 7, 3, Small-Scale Fluctuations of Relic Radiation

 —. 1980, MNRAS, 190, 413, The velocity of clusters of galaxies relative to the microwave background - The possibility of its measurement.

Tanimura, H., Zaroubi, S., & Aghanim, N. 2021, arXiv:2007.02952, A&A, 645, A112, Direct detection of the kinetic Sunyaev-Zel'dovich effect in galaxy clusters

Tegmark, M. & de Oliveira-Costa, A. 2001, astro-ph/0012120, Phys. Rev. D, 64, 063001, How to measure CMB polarization power spectra without losing information

Terrana, A., Harris, M.-J., & Johnson, M. C. 2017, arXiv:1610.06919, J. Cosmology Astropart. Phys., 2017, 040, Analyzing the cosmic variance limit of remote dipole measurements of the cosmic microwave background using the large-scale kinetic Sunyaev Zel'dovich effect

Tishue, A. J., Shiveshwarkar, C., & Holder, G. 2025, arXiv:2510.25821, arXiv e-prints, arXiv:2510.25821, The kSZ optical depth degeneracy and future constraints on local primordial non-Gaussianity

Torrado, J. & Lewis, A. 2019, Cobaya: Bayesian analysis in cosmology, Astrophysics Source Code Library, record ascl:1910.019

 2021, arXiv:2005.05290, J. Cosmology Astropart. Phys., 2021, 057, Cobaya: code for Bayesian analysis of hierarchical physical models

Virtanen, P., et al. 2020, Nature Methods, 17, 261, SciPy 1.0: Fundamental Algorithms for Scientific Computing in Python

White, M. 2015, arXiv:1504.03677, MNRAS, 450, 3822, Reconstruction within the Zeldovich approximation

Yuan, S., et al. 2024, arXiv:2306.06314, MNRAS, 530, 947, The DESI oneper cent survey: exploring the halo occupation distribution of luminous red galaxies and quasi-stellar objects with ABACUSSUMMIT

Zeldovich, Y. B. & Sunyaev, R. A. 1969, Ap&SS, 4, 301, The Interaction of Matter and Radiation in a Hot-Model Universe

Zhang, P. 2010, Monthly Notices of the Royal Astronomical Society: Letters, 407, L36, The dark flow induced small-scale kinetic Sunyaev–Zel'dovich effect, http://dx.doi.org/10.1111/j.1745-3933.2010.00899.x

Zhou, R., et al. 2023a, arXiv:2309.06443, J. Cosmology Astropart. Phys., 2023, 097, DESI luminous red galaxy samples for cross-correlations

 2023b, arXiv:2208.08515, AJ, 165, 58, Target Selection and Validation of DESI Luminous Red Galaxies

Zonca, A., Singer, L., Lenz, D., Reinecke, M., Rosset, C., Hivon, E., & Gorski, K. 2019, Journal of Open Source Software, 4, 1298, healpy: equal area pixelization and spherical harmonics transforms for data on the sphere in Python

APPENDIX A: CORRELATION STRUCTURE OF THE BINNED GALAXIES

When we split the galaxies into more redshift bins, these bins have non-zero correlation sourced by their overlapping redshift kernels due to the photo-z uncertainty. We show in this Appendix some plots of the off-diagonal correlation structure, specifically by plotting

 $r_{\ell}^{\alpha\beta} \equiv \frac{C_{\ell}^{g\alpha g\beta}}{\sqrt{C_{\ell}^{g\alpha g\alpha}C_{\ell}^{g\beta g\beta}}}$. We show this for 4 bins in Fig. A1 and for 16

bins in Fig. A2. The correlation is clear on large scales, and falls of on small scales due to the shot noise, although the underlying signals remain correlated.

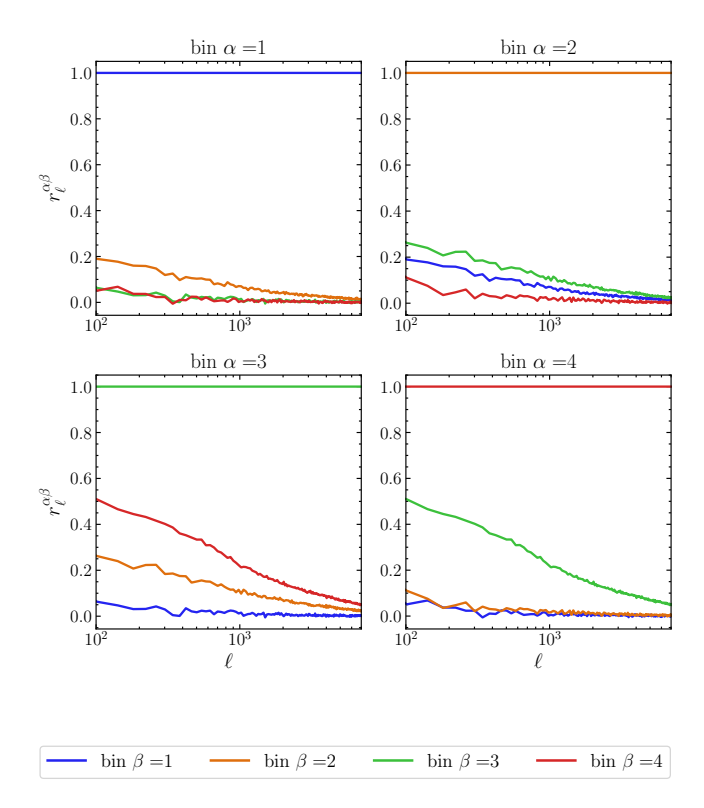


Figure A1. Inter-bin correlation structure of galaxy overdensity maps for the N = 4 bin case.

APPENDIX B: KSZ VELOCITY RECONSTRUCTION THEORY

The (two-dimensional)²⁷ kSZ temperature anisotropy $\Delta T^{\rm kSZ}$ in direction \hat{n} is of the form

$$\frac{\Delta T^{\text{kSZ}}(\hat{n})}{\bar{T}} = -\sigma_T \int d\chi a(\chi) v_r(\chi, \hat{n}) n_e(\chi, \hat{n}), \tag{B1}$$

$$\equiv -\int d\chi v_r(\chi, \hat{n}) \dot{\tau}(\chi, \hat{n}) \tag{B2}$$

where \bar{T} is the mean CMB temperature; σ_T is the Thomson scattering cross section; $a(\chi)$ is the scale-factor at comoving distance χ ; $v_r(\chi,\hat{n}) \equiv \vec{v}(\chi,\hat{n}) \cdot \hat{n}$ is the three-dimensional radial velocity field at (χ,\hat{n}) ; $n_e(\chi,\hat{n})$ is the electron density at (χ,\hat{n}) ; and $\dot{\tau}(\chi,\hat{n}) \equiv \frac{d\tau}{d\chi}(\chi,\hat{n})$ is the differential optical depth.

The (2+1)-dimensional galaxy number density field $\delta_{\alpha}^{g}(\hat{n})$ is

$$\delta_{\alpha}^{g}(\hat{n}) = \frac{\int d\chi \frac{dN^{\alpha}}{d\chi} \delta^{g}(\chi, \hat{n})}{\int d\chi \frac{dN^{\alpha}}{d\chi}}$$
(B3)

where $\frac{dN^{\alpha}}{d\chi}$ is the redshift distribution of the galaxies in bin α . When the large-scale velocity is held fixed (i.e., to the realization

²⁷ Throughout, we refer to fields as two-dimensional if they depend on the two-dimensional coordinate \hat{n} ; three-dimensional if they depend on the three-dimensional coordinates (χ, \hat{n}) ; and 2+1-dimensional if they depend on the quasi-three-dimensional redshift-binned tomographic coordinates (α, \hat{n}) . Thus both the three-dimensional vector field $\hat{v}(\chi, \hat{n})$ and the scalar field $v_r(\chi, \hat{n})$ are three-dimensional in our language.

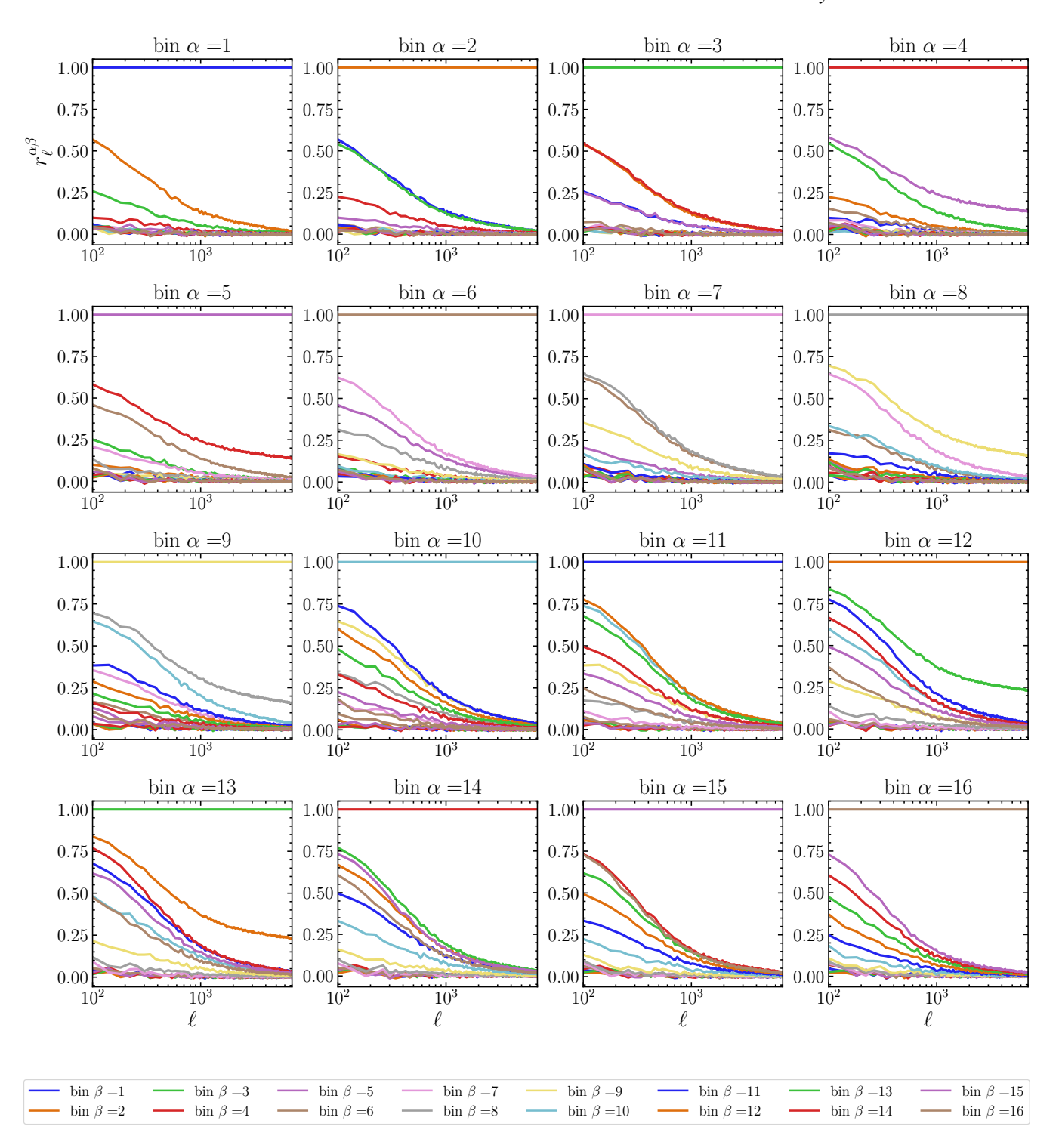


Figure A2. Inter-bin correlation structure of galaxy overdensity maps for the N=16 bin case.

of the velocity field in our Universe), the galaxies and the kSZ are

correlated at the two-point level according to ²⁸

$$\begin{split} \left\langle \frac{\Delta T_{\ell m}^{\text{kSZ}}}{\bar{T}} \delta_{\ell' m'}^{g^{\alpha}} \right\rangle_{\text{fixed } \nu} &= \sum_{\ell_1 m_1 \ell_2 m_2} (-1)^{m_1} W_{m_1 m_2 - m}^{\ell_1 \ell_2 \ell} \times \\ & \int d\chi \left\langle v_{r \ell_1 m_1}(\chi) \dot{\tau}_{\ell_2 m_2}(\chi) (\delta_{\alpha}^g)_{\ell' m'} \right\rangle, \end{split} \tag{B4}$$

²⁸ In this equation we restore a factor of $(-1)^m$ that was erroneously omitted in Equation (6) of McCarthy et al. (2025).

where $W_{m_1m_2m_3}^{\ell_1\ell_2\ell_3}$ is the following mode-coupling matrix:

$$\begin{split} W_{m_1 m_2 m_3}^{\ell_1 \ell_2 \ell_3} &= \sqrt{\frac{(2\ell_1 + 1)(2\ell_2 + 1)(2\ell_3 + 1)}{4\pi}} \begin{pmatrix} \ell_1 & \ell_2 & \ell_3 \\ 0 & 0 & 0 \end{pmatrix} \times \\ & \begin{pmatrix} \ell_1 & \ell_2 & \ell_3 \\ m_1 & m_2 & m_3 \end{pmatrix}. \end{split} \tag{B5}$$

Here, $\begin{pmatrix} \ell_1 & \ell_2 & \ell_3 \\ m_1 & m_2 & m_3 \end{pmatrix}$ are the Wigner 3-J symbols. In the squeezed $L \equiv \ell_1 \ll \ell_2, \ell_3$ limit (which dominates), this can be simplified and approximated as

$$\left\langle \frac{\Delta T_{\ell m}^{\rm kSZ}}{\overline{T}} (\delta_{\alpha}^{g})_{\ell' m'} \right\rangle \simeq \int d\chi \sum_{LM} (-1)^{M} \begin{pmatrix} \ell & \ell' & L \\ m & m' & -M \end{pmatrix} f_{\ell \ell' L} \times C_{\ell'}^{\dagger g \alpha} (\chi) v_{r L M} (\chi) \tag{B6}$$

whore

$$f_{\ell\ell'L} = \sqrt{\frac{(2\ell+1)(2\ell'+1)(2L+1)}{4\pi}} \begin{pmatrix} \ell & \ell' & L \\ 0 & 0 & 0 \end{pmatrix}$$
 (B7)

and

$$\langle \dot{\tau}_{\ell m}(\chi)(\delta_{\alpha}^g)_{\ell' m'} \rangle \equiv C_{\ell}^{\dot{\tau}g_{\alpha}}(\chi)\delta_{\ell\ell'}\delta_{mm'},$$
 (B8)

resulting from the statistical isotropy of the small-scale statistics of the galaxies and the electrons. Equation (B6) is the basis for kSZ velocity reconstruction: the only "unknown" in this expression is $v_{rLM}(\chi)$, as the left hand side is directly measurable from data and we can model $C_{\ell}^{\dot{\tau}g\alpha}(\chi)$. Given N independent galaxy overdensity maps labelled by α , we can create N velocity estimates

$$(v_{\alpha})_{LM} \sim W'^{L\ell_1\ell_2}_{Mm_1m_2} \left\langle T^{\text{kSZ}}_{\ell_1m_1}(\delta^g_{\alpha})_{\ell_2m_2} \right\rangle \tag{B9}$$

where W' are weights that depend on $C_\ell^{\dagger g\alpha}(\chi)$. The optimal weights have been derived several times in the literature (see, *e.g.* Deutsch et al. 2018; McCarthy & Johnson 2020; Cayuso et al. 2023; Bloch & Johnson 2024). The real-space estimator we use (see Equation (8)) is a real-space implementation of this optimal QE. Note that the final quantity estimated is a *projected* quantity (*i.e.*, with the redshift-dependence integrated out)

$$(v_{\alpha})_{LM} = \int W_{LM}^{v_{\alpha}^{\text{KSZ}}}(\chi) v_{r,LM}(\chi) d\chi$$
 (B10)

where $W_{LM}^{v_{\alpha}^{\rm kSZ}}(\chi)$ is a projection kernel. In practice, this is scale-independent on large scales such that $W_{LM}^{v_{\alpha}^{\rm kSZ}}(\chi)=W^{v_{\alpha}^{\rm kSZ}}(\chi)$. The projection kernel depends on $C_{\ell}^{\dot{\tau}g}$:

$$W^{\nu_{\alpha}^{\rm kSZ}}(\chi) \approx \frac{C_{\ell=\bar{\ell}}^{\dot{\tau}g_{\alpha}}(\chi)}{C_{\ell=\bar{\ell}}^{\dot{\tau}g_{\alpha}}},\tag{B11}$$

where $\bar{\ell}$ is some characteristic high- ℓ multipole which dominates the signal-to-noise (Bloch & Johnson 2024), and

$$C_{\ell}^{\tau g_{\alpha}} \equiv \int d\chi C_{\ell}^{\dot{\tau} g_{\alpha}}(\chi)$$
 (B12)

is the isotropic optical depth-galaxy cross power (with τ the total optical depth as opposed to the differential optical depth $\dot{\tau}$ such that $\tau \equiv \int \dot{\tau} d\chi$). If we make the assumption that the electrons evolve slowly in each redshift bin compared to the galaxy density, this can be further approximated as

$$W_{LM}^{\text{kSZ},\alpha}(\chi) \approx \frac{\frac{dN^{\alpha}}{d\chi}}{\int d\chi \frac{dN^{\alpha}}{d\chi}},$$
 (B13)

and so the velocity we estimate is the mean velocity projected along the redshift distribution of the galaxies used in the reconstruction.

APPENDIX C: DESCRIPTION OF SIMULATIONS

We use *N*-body simulations populated with galaxies using a halo occupation distribution (HOD) to validate our pipeline and complete our theory model as described in the text (Section 5). In this Section, we describe how we create the simulations.

Lightcone simulations

The Abacus Summit simulations are a set of *N*-body simulations run with Abacus (Garrison et al. 2021), with LRG-like galaxies added according to the HOD prescription of (Yuan et al. 2024). There are 25 "base" Abacus Summit lightcone simulations and 2 "huge" simulations. The "huge" simulations cover enough volume to be full-sky; the "base" simulations cover only 1/8 of the sky, and so cannot be used to fully cover the survey geometry we are interested in. Thus we use one of the "huge" simulations to test our pipeline, and create six quasi-independent simulations from it by rotating the sky.

τ and kSZ simulations

We create a τ map using the transfer function method of Liu et al. (2025), in which the dark matter density field from an N-body simulation is mapped to the corresponding gas field using a transfer function calibrated on a hydrodynamical simulation; we use the gas—dark matter transfer function measured from the TNG300-1 simulation (Nelson et al. 2019) at z=0.5.

Concretely, we use dark matter density shells from the AbacusSummit lightcone (with shell spacing $\sim 10~h^{-1}{\rm Mpc}$ between 0.3 < z < 1.1), and apply the gas—dark matter transfer function measured from the TNG300-1 simulation (Nelson et al. 2019) at z=0.5 to obtain $\delta_{\rm gas}$. The resulting τ shells are then summed (after converting to the appropriate units) to yield the redshift-evolving $\tau(\hat{n},z)$ map at nside=8192.

We create a kSZ map by additionally multiplying each τ shell by the line-of-sight halo velocity field before summing, with the velocity field estimated from the particle velocities within each pixel.

Small-scale DESI DR9 LRG Galaxy simulations

We add galaxies according to a HOD described in Hadzhiyska et al. (2024). We downsample the galaxies to follow the $\frac{dN}{dz}$ measured from the data. We add photo-z noise of width $0.027 \times (1+z)$ to the galaxies corresponding to the extended LRG sample.

For the small-scale two-dimensional galaxy overdensity maps, we create tomographically binned galaxy overdensity maps according to the same prescription we do on the data, by applying the photo-z boundaries in Table 1 and projecting to 2+1 dimensions following the description in Section (2.2.1), although on the full sky. We cross-correlate this maps with the τ map to estimate the $C_{\ell}^{g\tau}$ used in our kSZ reconstruction pipeline.

Large-scale DESI DR10 LRG Galaxy simulations

To reproduce the photometric redshift errors and $\frac{dN}{dz}$ distribution of the DR10 Extended LRG sample, we add Gaussian noise of width

 $\sigma_z = 0.02 \times (1+z)$ to the observed (redshift-space) redshift of each object and downsample the galaxy catalog to match the observed $\frac{dN}{dz}$. We then apply a mask so that the mock footprint closely matches that of the data. Finally, we divide the mock catalog into four redshift bins, matched to the data both in range and $\frac{dN}{dz}$.

2-dimensional velocity field simulations

We create an estimate of the "true" velocity field that we wish to estimate v^{true} by projecting the true halo velocities of the objects according to

$$\hat{v}^{\text{true},\alpha}(\hat{n}) = \frac{\sum_{i} v_{i} \frac{dN^{\alpha}}{dz}(z^{i})}{\int \frac{dN}{dz}},$$
(C1)

where the sum is over all objects i in the pixel at (\hat{n}) and $\frac{dN}{dz^{\alpha}}(z^{i})$ is the redshift kernel of the velocity field we wish to estimate evaluated at the redshift of the object i. Again, we normalize by the $\frac{dN}{dz}$ of the entire simulation. We estimate \hat{v}^{true} before downsampling as it is a cosmological quantity that does not depend on the details of the survey used to estimate it.

The quantity that \hat{v}^{true} is estimating can be modelled as the following projection of the underlying velocity field:

$$v^{\text{true},\alpha}(\hat{n}) = \int d\chi \frac{dN^{\alpha}}{d\chi} v(\chi,\hat{n}).$$
 (C2)

APPENDIX D: AUTO POWER SPECTRA OF THE CONTINUITY-EQUATION VELOCITY

In this Appendix we show the measured auto power spectra of the continuity-equation auto power spectra, and show that our model is sensible. In Fig. D1 we show the measurement as well as the prediction from theory and simulations. The Λ CDM theory is indicated in dashed purple; the mean from the simulations is shown in red and green for is shown in for NGC and SGC respectively. The power suppression with respect to theory seen in the simulations seems to match what is seen in the data.

APPENDIX E: STABILITY OF CONSTRAINTS FOR VARIOUS DATA COMBINATIONS

We found evidence for a foreground bias in the diagonal of $C_L^{v^{\rm KSZ}g}$. In this Appendix we explore how such a bias may propagate into the amplitude constraints.

We show in Figure E1 the constraints on one overall velocity bias parameter for the $C_L^{\nu^{\rm kSZ}\nu^{\rm cont}}$ case and for the $C_L^{\nu^{\rm kSZ}g}$, where we consider the diagonals separately to the remaining points. We see here that we see signals consistent with the presence of foregrounds in the $C_L^{\nu^{\rm kSZ}g}$ measurement, as we see a non-zero signal when we use the y map for the velocity reconstruction, and an inconsistent signal when we use the MV NILC and the y-deprojected NILC. Interestingly, the bias is not enough to be noticeable in the overall dataset.

APPENDIX F: DEPENDENCE OF AUTO POWER SPECTRA ON CLUSTER MASKING FOR THE 16-BIN CASE

As discussed in Section 6.1, we find that the observed offset between the measured auto power spectrum of the kSZ-reconstructed velocity and the analytic prediction is mitigated when tSZ clusters are masked before performing the kSZ velocity reconstruction. In this Appendix we show explicitly the effect of this procedure for the baseline N=16 bin case. This is shown for SGC in Fig. F1 and for NGC in Fig. F2.

APPENDIX G: DEGENERACIES IN THE $F_{\rm NL}$ ANALYSIS AND FULL $F_{\rm NL}$ CORNER PLOT

The full corner plot for the $f_{\rm NL}$ analysis is shown in Fig. G1. The use of a multiple- b_{ν}^{α} model reduces the strong correlation between b_{ν} and $f_{\rm NL}$ that is clearly evident int he single- b_{ν} model; however, the b_{ν}^{α} remain correlated with $f_{\rm NL}$, even if the correlation is not as strong as in the single- b_{ν} case. Indeed, the bins with higher b_{ν}^{α} are most correlated with $f_{\rm NL}$, as they are precisely the subsets of the dataset where we have most constraining power; this is indicated in Fig. G2 where we extract the correlation coefficient between each b_{ν}^{α} parameter and $f_{\rm NL}$ and plot this against the posterior mean of b_{ν}^{α} . A positive correlation is evident in this plot.

This paper has been typeset from a TEX/IATEX file prepared by the author.

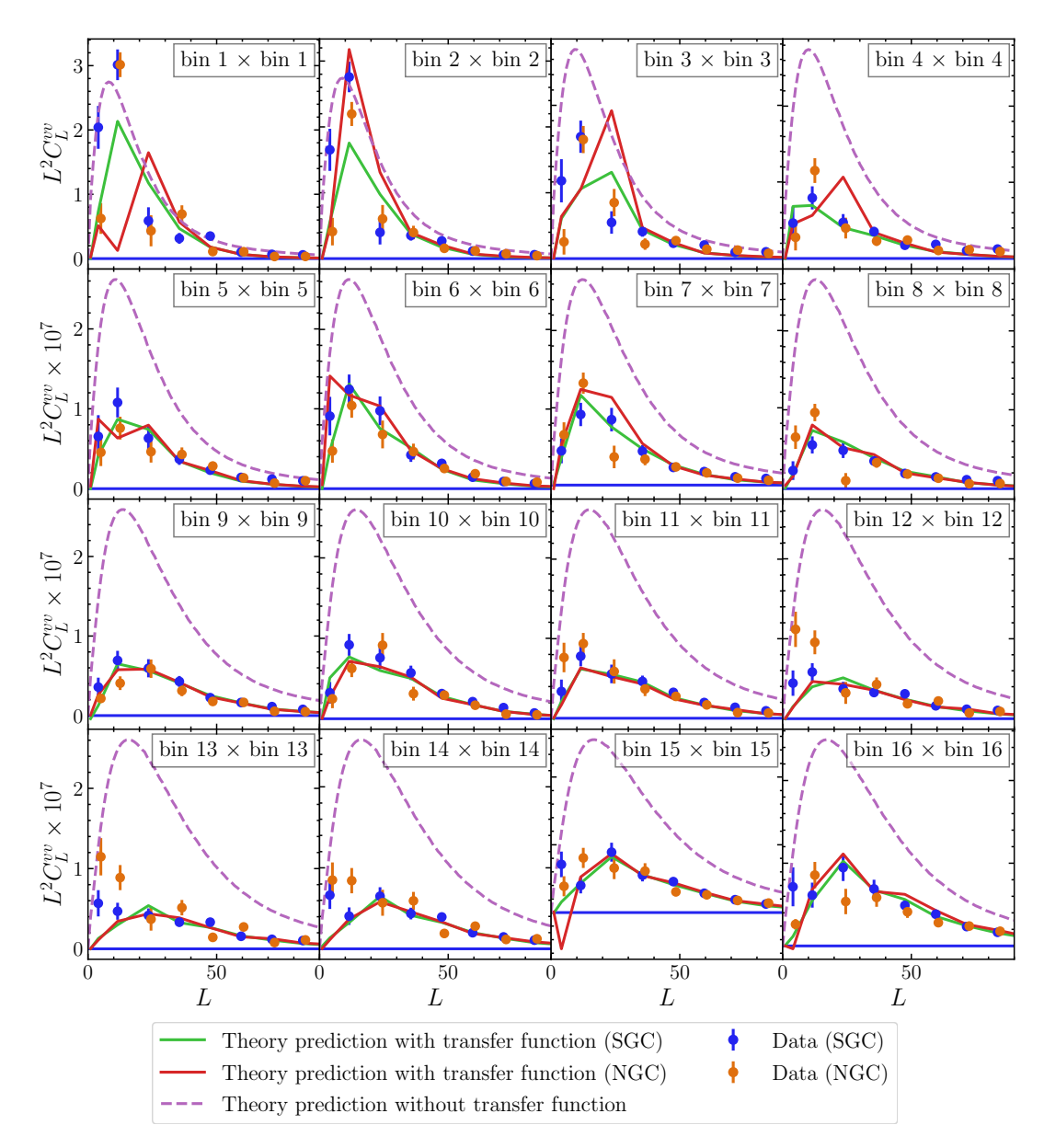


Figure D1. The measured auto power spectra of the continuity-equation velocities. We show the Λ CDM prediction in dashed purple; the continuity equation reconstruction suppresses the power. We calibrate this suppression with simulations and we show the mean from the simulations in red and green. The simulations capture the power in the data well.

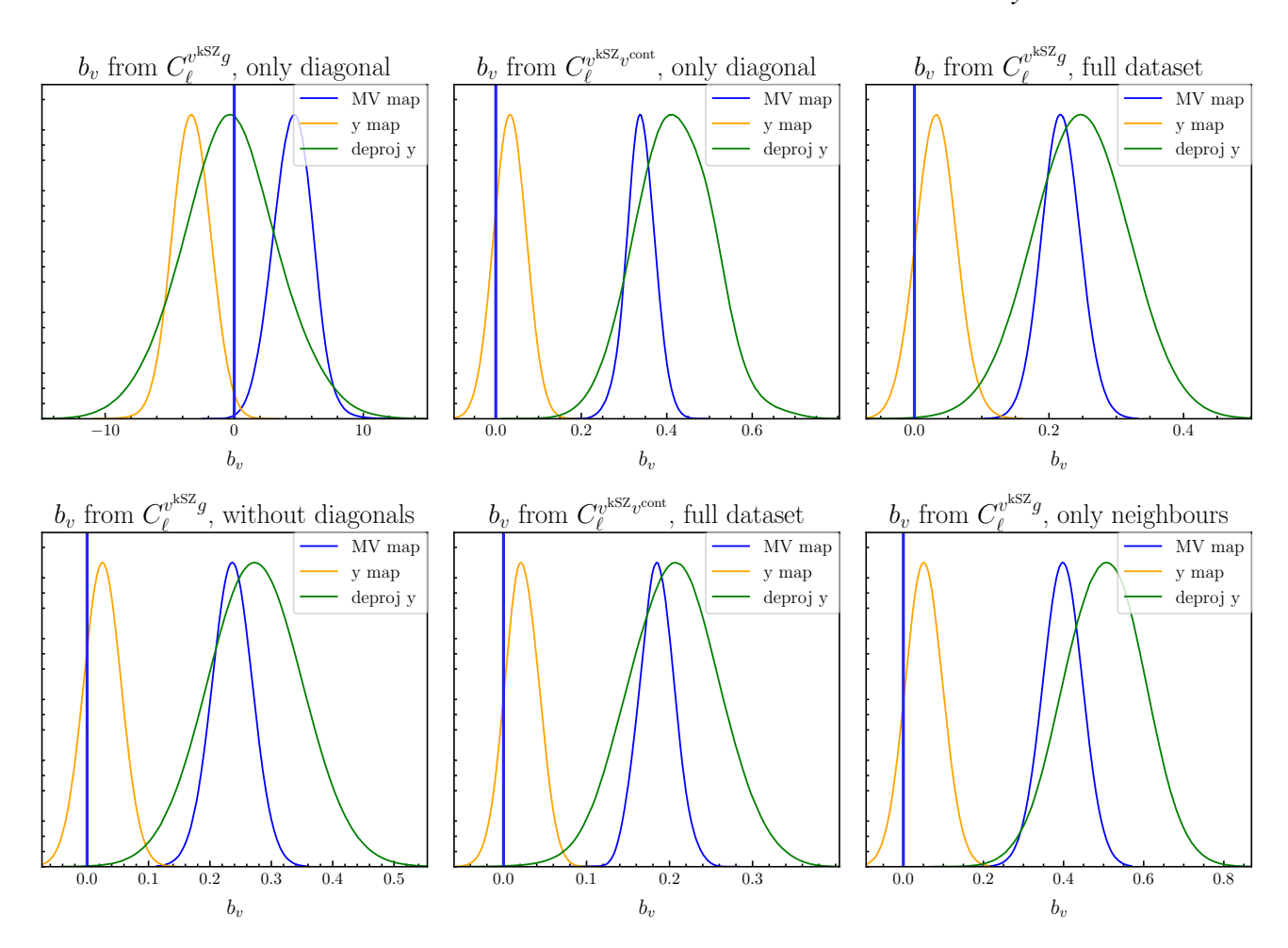


Figure E1. The constraints on the overall amplitude b_v for several data combinations. In particular, we are testing consistency for different signal maps and also immunity to foregrounds. The yellow curves, labelled "y map", should be null, as the temperature leg used for velocity reconstruction is expected to have no kSZ signal and only foregrounds. At the same time, the blue and green curves—labelled "MV NILC" and "deproj y" respectively—should be consistent, as we expect these are both unbiased measurements of the kSZ signal but with different amounts of foregrounds and noise (in particular, the y-deproj map has no tSZ, at the expense of possibly higher CIB, and it also has significantly higher noise). For all of the $C_L^{vkSZ_v^{cont}}$ cases that we look at —both the diagonal-only and the diagonal+neighbours case—these tests pass. However, for the $C_L^{vkSZ_g}$ diagonals (the first plot), these tests fail. We see a strong negative signal with the y-map. Because this subset of the data contributes only a small amount of the overall signal-to-noise, it is not significant enough to leak into the full measurement (the third plot), but it is clear that these points should not be included and combined with the rest of the points as they are not consistent. We also inspect the constraint from an "only neighbours" formulation of $C_L^{vkSZ_g}$, as there is a lot of redshift overlap between neighbouring bins.

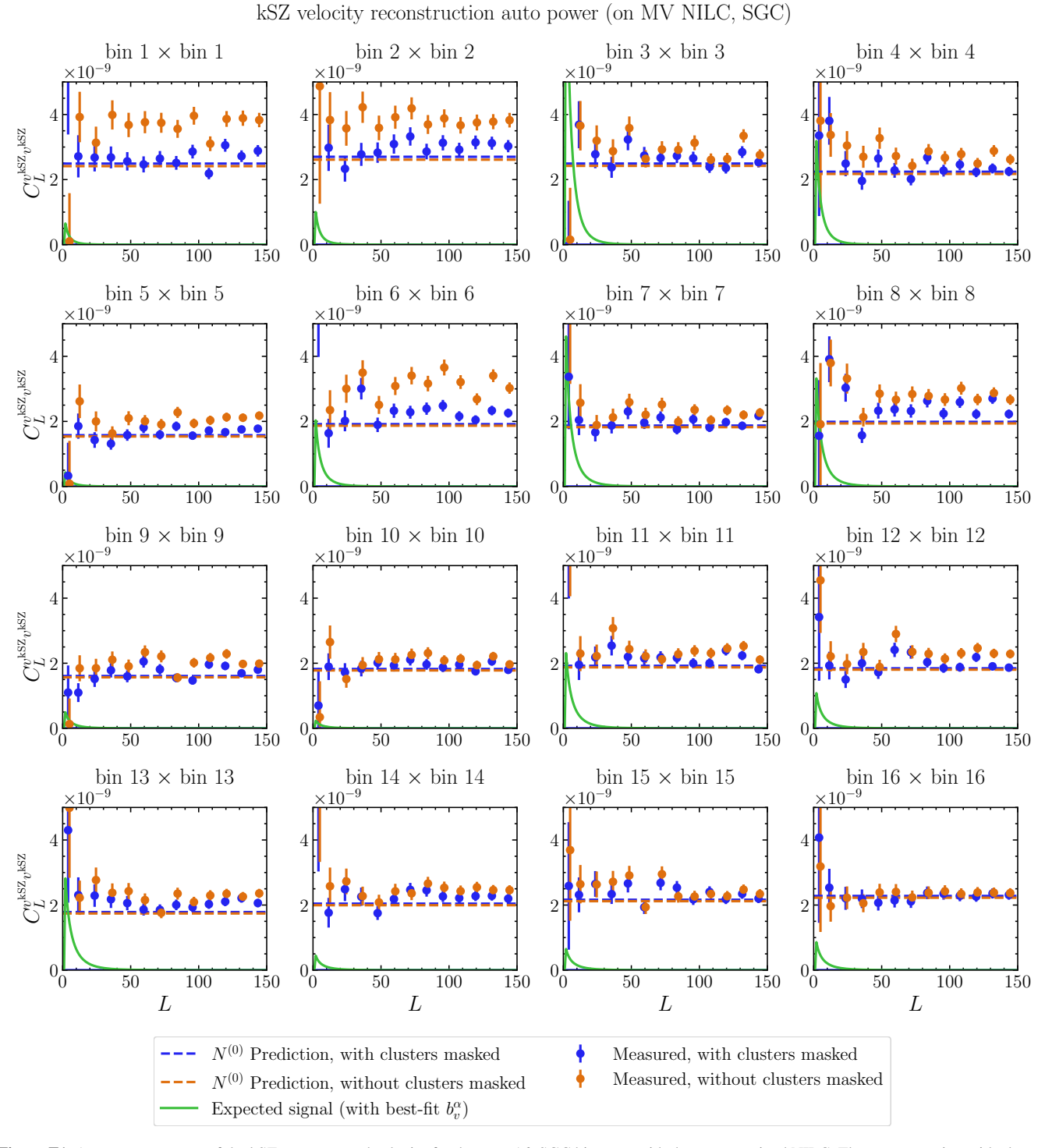


Figure F1. Auto power spectra of the kSZ reconstructed velocity for the N = 16, SGC bin case, with the unconstrained NILC. The reconstruction with clusters masked has power that agrees with the analytic prediction; as in the 4-bin case, the one with clusters retained does Note that in the higher redshift bins, even the unmasked reconstruction agrees with theory; this is not unexpected given that the clusters are mostly at lower z. Note that we have slightly offset the orange "measured, without clusters masked" points for slightly better comparison with the other points.

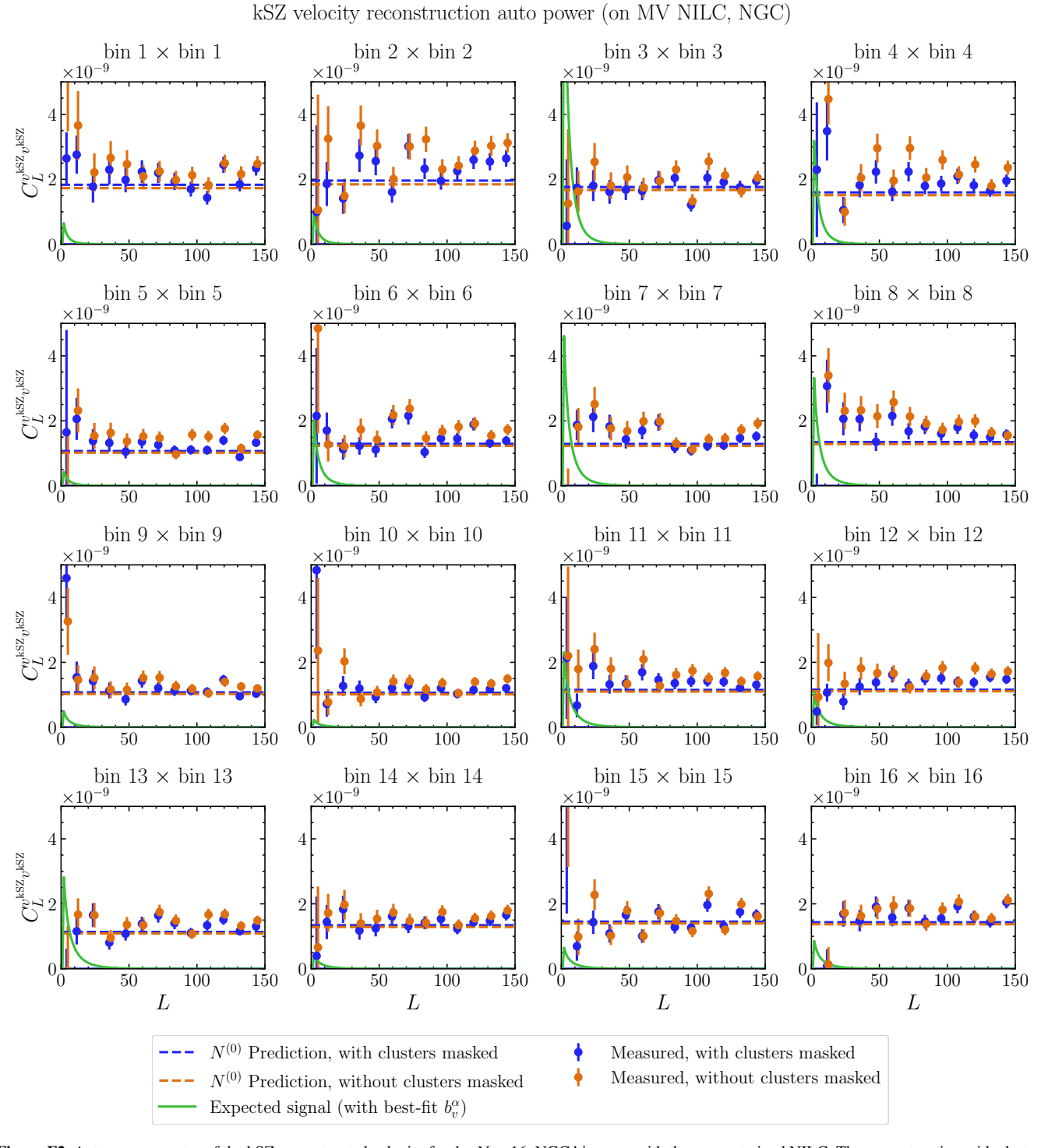


Figure F2. Auto power spectra of the kSZ reconstructed velocity for the N = 16, NGC bin case, with the unconstrained NILC. The reconstruction with clusters masked has power that agrees with the analytic prediction; as in the 4-bin case, the one with clusters retained does Note that in the higher redshift bins, even the unmasked reconstruction agrees with theory; this is not unexpected given that the clusters are mostly at lower z. Note that we have slightly offset the orange "measured, without clusters masked" points for slightly better comparison with the other points.

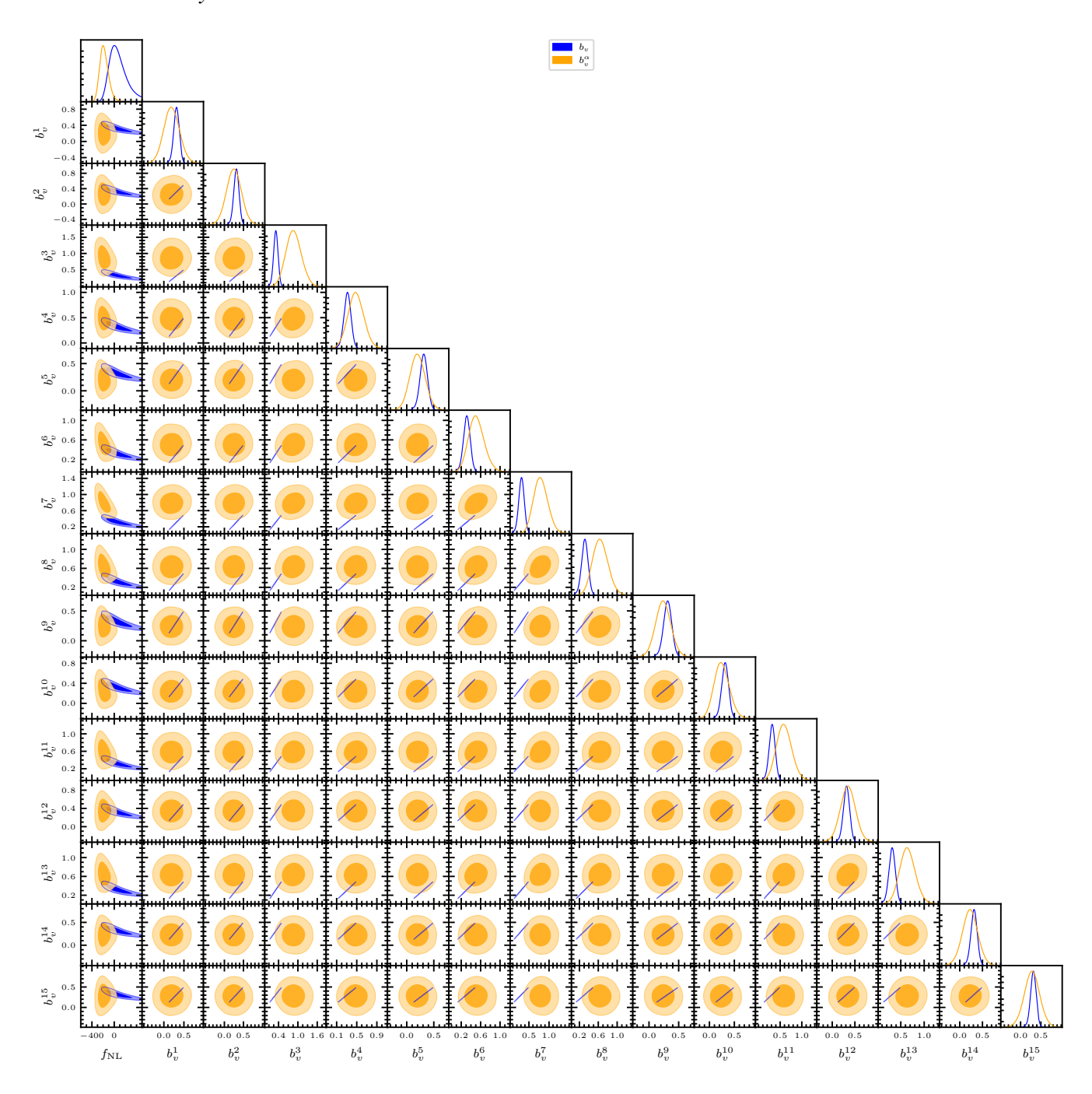


Figure G1. Full corner plot for the $f_{\rm NL}$ analysis

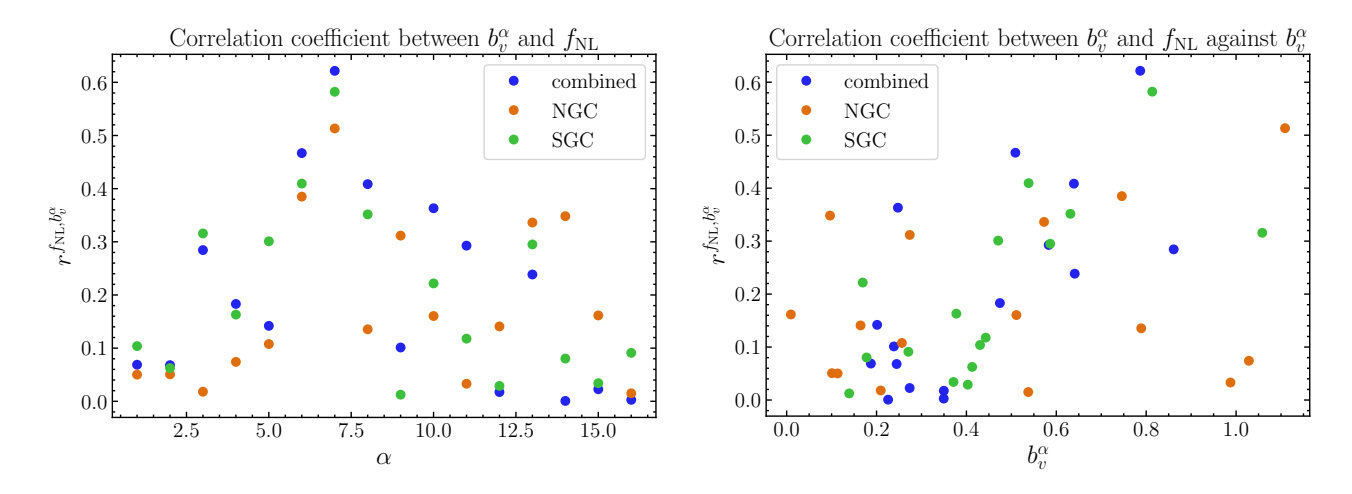


Figure G2. The correlation coefficient between the velocity bias and $f_{\rm NL}$, plotted against bin number on the left to indicate which bins are dominating the constraint, and against value of the velocity bias on the right. We see that bin 7 is the most correlated with $f_{\rm NL}$, and we see a positive correlation between $r^{b_V^{\alpha}}f_{\rm NL}$ and b_V^{α} .